Stony Brook University

The official electronic file of this thesis or dissertation is maintained by the University Libraries on behalf of The Graduate School at Stony Brook University.

Performance study of Cascade Reconstruction at the Glashow Resonance in IceCube

A Thesis Presented

by

Hans Niederhausen

to

The Graduate School

in Partial Fulfillment of the Requirements

for the degree of

Master of Arts

in

Physics

Stony Brook University

December 2012

Stony Brook University

The Graduate School

Hans Niederhausen

We, the thesis committee for the above candidate for the Master of Arts degree,
hereby recommend acceptance of this thesis.

Joanna Kiryluk - Thesis Advisor
Assistant Professor, Department of Physics and Astronomy

Dmitri Kharzeev
Professor, Department of Physics and Astronomy

Dominik A. Schneble
Associate Professor, Department of Physics and Astronomy

This thesis is accepted by the Graduate School.

Charles Taber
Interim Dean of the Graduate School

Abstract of the Thesis

Performance study of Cascade Reconstruction at the Glashow Resonance in IceCube

by

Hans Niederhausen

Master of Arts

in

Physics

Stony Brook University

2012

IceCube is a one cubic kilometer neutrino telescope at the South Pole. Its primary goal is to discover high energy cosmic neutrinos and anti-neutrinos from astrophysical sources. Observation of the spectrum near the characteristic energy $E_\nu \approx 6.3\,\mathrm{PeV}$ of the Glashow resonance, the interaction of anti-neutrinos with atomic electrons via $\bar{\nu}_e + e^- \to W^-$, is of particular interest. Since the cross section for this process can be calculated from first principles, it is possible to quantify separately the fluxes for neutrinos and anti-neutrinos if the resonance is observed above a continuum. In turn, such a separation will give unique insights into the astrophysics properties of the sources.

We conducted the first IceCube performance studies and optimizations for likelihood-based algorithms to reconstruct (anti-)neutrino-induced particle showers (cascades) in the energy range of the Glashow resonance using simulated data from electron (anti-)neutrino Monte Carlo generators and detector response simulations. For hadronic showers in the energy range $1\,\mathrm{PeV} < E_\nu < 10\,\mathrm{PeV}$ that are well contained within the IceCube instrumented volume, we achieved an energy resolution of $10\% < \sigma\left(\Delta E/E\right) < 14\%$ depending on the ice model and the shower position in the detector. The position and direction resolution varied between $1.1\,\mathrm{m} < \sigma\left(\Delta x, \Delta y, \Delta z\right) < 4.2\,\mathrm{m}$ and $8° < \theta_{RMS} < 27°$, respectively. We verified and refined the methods on experimental data using an in-situ laser as a pulsed light source with constant brightness and a single wavelength of $\lambda = 337\,\mathrm{nm}$. The energy resolution for reconstructed laser events was found to be $\sigma\left(\Delta E/E\right) = 1.8\%$ from the reconstructed energy of $E \pm \delta E_{stat} = (527 \pm 9)$ TeV, where the uncertainty is statistical. For $83\% - 92\%$ of the laser events, we reconstructed the zenith angle

to within $\Delta\theta < 2°$ and found a position resolution of $0.3\,\mathrm{m} < \sigma\left(\Delta x, y, z\right) < 0.4\,\mathrm{m}$ from the reconstructed positions. The existence of considerable systematic effects is evidenced by a shift of the reconstructed laser position from the true position by $3.7\,\mathrm{m}$. Such effects arise, for example, from differences in photon propagation at different wavelengths. The laser data represent a best case scenario, in view of its illumination of the detector and the monochromatic laser emission. The simulation results confirm IceCube's capability to observe astrophysical neutrino fluxes near the Glashow resonance and form a first demonstration, corroborated by an analysis of laser data, of IceCube's pointing capability with the cascade detection channel in this energy range.

Acknowledgements

I would like to express my sincere gratitude to

Joanna Kiryluk

Mariola Lesiak-Bzdak

Eike Middell

Jakob van Santen

Dmitri Kharzeev

Dominik Schneble

Ludwig Krinner

and finally my parents, to whom I dedicate this thesis.

Contents

List of Figures

List of Tables

Chapter 1

Introduction to Neutrino Astronomy

It is of greatest interest to understand the acceleration and propagation of high energy cosmic rays. A large step forward would be to identify their sources. Such a search based on the detection of the cosmic ray particles themselves is intrinsically difficult due to the fact, that charged particles get deflected in galactic magnetic fields ($B \sim 3\mu$G). Only particles at the highest energies are less affected by magnetic deflection.

One approach to avoid this problem is to use the neutrino as cosmic messenger, which can travel almost undeflected from its source to the detector due to its low interaction cross-section with matter. It is because of this small probability of detection and the typically low fluxes, that huge instrumented volumes are required in oder to accumulate enough statistics, required for a possible discovery of extra-terrestrial high energy neutrinos.

The largest instrument, built up to date, possessing realistic chances to discover astrophysical neutrinos, is the IceCube Neutrino Observatory [1], covering a cubic kilometer of glacial ice at the South Pole. IceCube has been collecting data since 2006 in different partial configurations during its construction. It was completed in December 2010. Ice-Cube detects the Cherenkov light, radiated by charged leptons, which are created when neutrinos interact in or near the detector, starting at $\sim 100\,$GeV up to $\sim 100\,$EeV. Its main goal, the discovery of extra-terrestrial high energetic neutrinos, is yet to be achieved. In that context the Glashow Resonance process is particularly interesting. At an energy of $E_{\bar{\nu}_e} = 6.3\,$PeV electron anti neutrinos possess a drastically enhanced probability to interact with atomic electrons, while traversing the detector. A discovery of that resonance would likely imply the first observation of astrophysical neutrinos in IceCube.

1.1 Cosmic Rays

Cosmic rays denominate extra-terrestrial particles, which impinge on earth's atmosphere and produce extensive air showers of secondary particles. Most primary nucleons are free protons (79%). About 70% of the remaining fraction are bound Helium nuclei [2]. Small contributions of heavier nuclei [3] exist. Our current knowledge about the energetic distribution of incident high energetic cosmic rays, as measured by various such experiments, is summarized in Figure 1.1.

At energies below 100 TeV one typically performs direct measurements of the primary cosmic rays in balloon or satellite based experiments, to extract charge, mass and energy of the respective particle. However at larger energies due to the low fluxes (less than one particle per km^2 and century above 100 EeV [3]) by far larger collective areas are necessary for detection, hence direct measurements are not feasible anymore. Information about high energetic cosmic rays is thus provided by large earth based air shower experiments, which infer the properties of the primary particle from the measured observables of the air shower.

The Cosmic Ray Spectrum
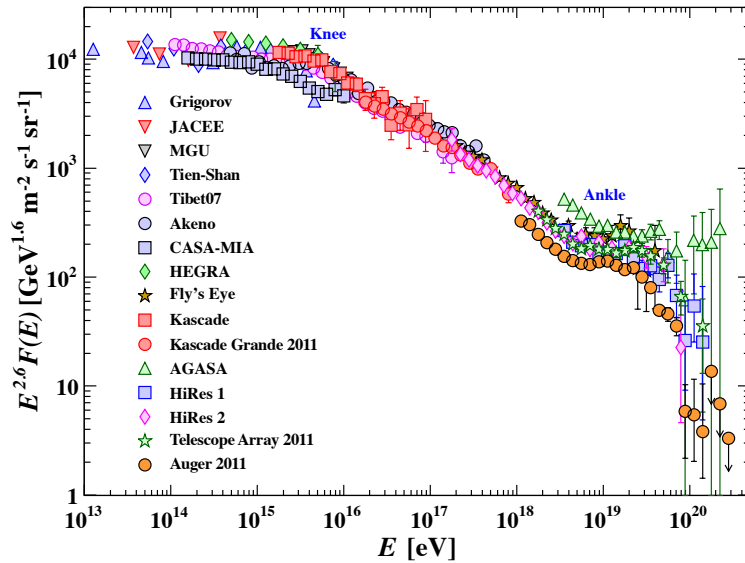
FIGURE 1.1: The flux of high energetic cosmic rays as measured by various experiments, weighted with $E^{2.6}$. The transition into the knee region (at 10^{15} eV) and the transition from the knee region to the ankle (at 3×10^{18} eV) are clearly visible. At highest energies several measurements are consistent with the presence of a cut-off. (Figure from [2])

The cosmic ray spectrum, shown in Figure 1.1, can be described as a series of power

laws ($E^{-\gamma}$, with γ being the spectral index) which holds over 8 orders of magnitude in energy and about 24 orders of magnitude in flux [4]. It can be characterized as follows:

- $100\,\mathrm{GeV} < E_{CR} < 1\,\mathrm{PeV}$: $\gamma \approx 2.7$

- $1\,\mathrm{PeV} < E_{CR} < 3\,\mathrm{EeV}$: $\gamma \approx 3.0$ (knee)

- $3\,\mathrm{EeV} < E_{CR} < 30\,\mathrm{EeV}$: $\gamma \approx 2.6$ (ankle)

This spectrum has two interesting regions: the steep knee region and the high energy ankle, which is cut off around $30\,\mathrm{EeV}$ [4]. Although until today the physical processes which cause the change of the spectrum at the lower bound of the knee region are not unambiguously identified, two scenarios are generally discussed. One idea is that the begin of the knee region indicates an upper bound of energies, to which galactic supernovae, a favored candidate source for cosmic rays up to PeV regime, could accelerate particles. Another explanation could be leakage of particles from the galaxy, since above a certain energy the galaxy is expected not to be able to confine those particles anymore. This bound can be approximately estimated using the following relation between the Larmor radius r_L of a proton and the strength of the galactic magnetic field B [3]:

$$r_L = 1.08\,\mathrm{pc}\,\frac{E/\mathrm{PeV}}{Z \cdot B/\mu\mathrm{G}} \tag{1.1}$$

where Z is the atomic number. From this one can see that the energy cut-off increases for heavier nuclei. The kink in the spectrum is thus thought to be the energy at which the proton energy is cut-off. The knee region is then made up from the fluxes of heavier nuclei with their individual cut-offs along the knee. The ankle might indicates a change from dominantly galactic cosmic rays to those of extra-galactic origin, which may have been accelerated to higher energies, thus having a harder spectrum [4]. The presence of an overall cut off at energies around $30\,\mathrm{EeV}$ in the cosmic ray spectrum has been observed by the HiRes [5], Auger [6] and Telescope Array[7] experiments, rejecting an earlier non-confirmation of the AGASA experiment [8].

The GZK Limit

This natural end of the spectrum is particularly interesting since it was predicted already in 1966 by Kenneth Greisen [9] and independently by Vadim Kuzmin and Georgiy Zatsepin [10] to appear around $50\,\mathrm{EeV}$. They attributed the cut-off to be due to interactions between cosmic ray protons and photons of the cosmic microwave background, which lead to resonant $\Delta\,(1232)$-production and subsequent decay into nucleons and pions.

$$p + \gamma \rightarrow \Delta \rightarrow p + \pi^0 \tag{1.2}$$

$$p + \gamma \rightarrow \Delta \rightarrow n + \pi^+ \tag{1.3}$$

This means that only sources within the "GZK-horizon" will contribute to the corresponding flux of UHE cosmic rays observed at earth. For example 90% of the protons with $E > 60$ EeV, observed at earth, have been produced within $L = 130$ Mpc [11]. As for now it is not unambiguously clear, that the CR cut-off, observed in various experiments, is due to the processes mentioned above, or whether the CR sources simply can not provide the required energy above this threshold. Both scenarios could be distinguished by observing neutrinos produced by the decay of charged pions, which were created in GZK interactions:

$$\pi^+ \to \mu^+ + \nu_\mu \tag{1.4}$$

$$\mu^+ \to e^+ + \nu_e \tag{1.5}$$

In case the GZK cutoff is realized in nature, those neutrinos should contribute to the diffuse flux of astrophysical neutrinos, which neutrino telescopes like IceCube aim to observe.

Candidate Source of Cosmic Rays

There has been a long term interest in the sources of cosmic rays. Up to know it is not known where these particles get accelerated to their enormous energies (up to 10^{20} eV). However some considerations allow to largely constrain possible sources. First, the geometry of the respective object should be such that the particle can be trapped inside the source while being accelerated. Secondly the source should have enough energy to provide the particles with the required power. Furthermore the acceleration process in the source should not lead to a massive emission of radiation in form of photons or neutrinos in order not to conflict with already established flux limits on earth. The geometric constraint can be expressed as $r_L \leq R$ (with R being the source "radius", i.e its extension). This yields a maximum particle energy E_{max}, which a source of extension R and average magnetic field strength B is capable to confine [12], as was first suggested by A. M. Hillas in 1984 [13].:

$$E_{max} \approx 0.03 \cdot \eta \cdot Z \cdot \frac{B}{G} \frac{R}{km} \, GeV \tag{1.6}$$

η is a source efficiency factor.

Viable cosmic ray sources can thus be visualized in the B-R parameter space, the so called Hillas-Plot (Figure 1.2). Among all the possible sources, which fulfill the necessary but not sufficient conditions, shown in Figure 1.2, the most promising are AGNs (Active Galactic Nuclei) and GRBs (Gamma Ray Bursts).
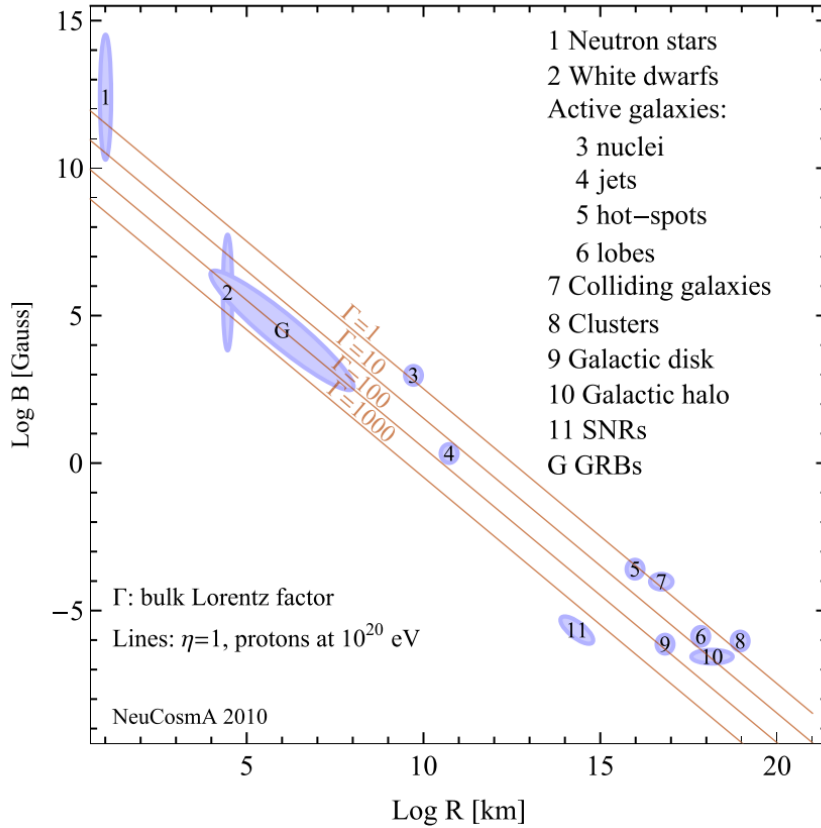
FIGURE 1.2: The figure shows possible sources of Cosmic Rays according to the Hillas criterion (Active Galactic Nuclei,GRBs, etc.). The influence of the source movement is depicted by showing the relation for different bulk lorentz boosts Γ. An optimistic acceleration efficiency of $\eta = 1$ is assumed. (Figure from [12])

Active Galactic Nuclei are the very bright regions in some galaxies, which host supermassive black holes. Gravitationally bound material forms an accretion disc, which heats up due to dissipative processes, leading to intense emission over a large range in the electromagnetic spectrum. In some AGNs relativistic jets have been observed, which are typically produced in the accretion disc. These jets could constitute an environment in which so-called first order Fermi acceleration might happen. Given typical properties of an AGN like its extension, which is of the order $R \sim 1.5 \cdot 10^{10}$ km, and magnetic field strengths in the center of $B \sim 300$ G (for a black hole with mass $m \sim 10^9\, M_\Theta \sim 2 \cdot 10^{30}$ kg), these objects could confine particles up to $E_{max} \sim 150$ EeV. Electrostatic processes in the black hole magnetosphere would then allow for an acceleration up to 100 EeV [4]. In 2007 the Pierre Auger Collaboration announced to have found a correlation between the arrival directions of their highest energetic cosmic ray events ($E_{CR} > 57$ EeV) and the locations of known AGNs. The hypothesis of their arrival directions being isotropic was rejected at 99% confidence [14]. Nevertheless it was not possible to unambiguously deduce that AGNs are the long searched source, since their location is itself correlated with the abundance of nearby matter, i.e. galaxies.

Furthermore additional data collected by Auger drastically lowered the significance of this observation and their claim did not persist [15].

Gamma Ray Bursts are the most violent electromagnetic processes, so far observed in the universe. They release large amounts of energy in a short flash of gamma rays, typically on a timescale of milliseconds up to one minute. Multiple shock regions formed by these events are the potential zones in which cosmic rays might get accelerated to their energies. Typical magnetic fields are of the order of $B \sim 10^6$ G at a distance of $R \sim 10^7$ km of the center, allowing for acceleration up to 100 EeV [4]. The recently published non-observation of neutrino events correlated in space and time with known GRBs by the IceCube Collaboration, either strongly challenges current GRB models or, given these models are correct, disfavors GRBs as being the source of UHECRs [16].

Fermi Acceleration

It is important to model the acceleration processes, which give rise to the observed energy spectrum. A first explanation was published by Enrico Fermi in 1949. He proposed moving magnetic fields, created by wandering matter clouds of the interstellar medium, as being mainly responsible for the acceleration [17]. Charged particles in the vicinity of these clouds would spiral along magnetic field lines and scatter of inhomogeneities, which are present in such fields. Given the random nature of these scatterings, some particles will loose and some particles will gain energy. Assuming elastic scattering of the inhomogeneities, Fermi showed that in this model a relativistic particle would on average gain energy per scattering, and this gain would be proportional to the square of the ratio between the (non-relativistic) velocity V of the cloud and the vacuum speed of light c [18]:

$$\left\langle \frac{\Delta E}{E} \right\rangle = \frac{8}{3} \left(\frac{V}{c} \right)^2 \tag{1.7}$$

It can be shown that this model naturally predicts a power-law energy spectrum [18]:

$$N\left(E\right) \propto E^{-x} \tag{1.8}$$

with $x = 1 + (\alpha \tau_{esc})^{-1}$ and τ_{esc} being the time scale, for which the particle stays in the acceleration region. α describes the rate of the energy increase $\frac{dE}{dt} = \alpha E = \frac{4V^2}{3cL}$ with L being the mean free path between clouds along a magnetic field line. This so called second order Fermi acceleration leads to a slow energy gain per particle. Following the line of argument of Fermi, a more efficient mechanism was proposed by several groups in the late 1970s [19][20][21], the so called diffusive shock acceleration, also known as first order Fermi acceleration. Given a strong shock, which propagates through a diffuse

medium at super sonic speeds, the average energy gain per particle scales linearly with the ratio between the (still non-relativistic) velocity of the shock V and the speed of light c, when the particles cross from the upstream (in front of the shock) to the downstream (behind the shock) region (and vice-versa) [18]:

$$\left\langle \frac{\Delta E}{E} \right\rangle = \frac{2}{3} \left(\frac{V}{c} \right) \tag{1.9}$$

This scenario predicts the following energy spectrum

$$N\left(E\right) \propto E^{-2} \tag{1.10}$$

for primary particles emitted from the respective source.

1.2 The Neutrino and its role in the Standard Model

The neutrino was first proposed in 1930 as a neutral spin-$\frac{1}{2}$ particle by Wolfgang Pauli, in an attempt to resolve the tension between observations in the context of β-decay and the energy conservation law [22]. The first theoretical description was given by Enrico Fermi in 1934 who concluded, that the mass of the neutrino must either be zero or at least very tiny compared to the mass of an electron [23]. However due to the small probability of neutrino interactions with matter, it took more than 20 years until it was first observed by the team of Cowen and Reines in 1956, who used reactor neutrinos to observe inverse beta decay in a liquid scintillator [24]. Since then various experiments concerning the neutrino but also other particles and their interaction have led to a consistent picture of physics at the smallest scales, the Standard Model of particle physics.

The Standard Model of Particle Physics
The Standard Model (SM) describes the interplay between all presently known particles, induced by the known fundamental forces, except gravity. In this model the forces are mediated by exchange of the so called gauge bosons. The strong force, which acts among particles, that possess color charge, for example protects larger nuclei from disintegration due to repulsive electromagnetic forces. The corresponding mediators are eight massless gluons. The well-known electromagnetic force which exists between particles, that carry electric charge, is mediated by the massless photon. Neutrinos interact via weak interactions, since they carry neither electric nor color charge. This interaction acts on the weak isospin of a particle and is caused by the exchange of the massive $W^{\pm}$ and Z^0 bosons. Since β-decay is a weak process, it is not surprising that the neutrino

was first proposed in that context. Unfortunately up to now it was not possible to include gravity in that description. However since gravitational interactions are negligible in strength, compared to the other three forces at all energy scales relevant for current (and probably future) measurements, the Standard Model with that respect provides a complete description of particles dynamics.

The particle content of the Standard Model can be divided according to the spin of the respective particle in scalar particles (Spin 0), fermions (Spin $\frac{1}{2}$) and gauge-bosons (Spin 1). The fermions, which make up the matter particles, can subsequently be organized as leptons, which do not participate in strong interactions, and quarks which do. Since for this thesis mainly the weak part of the Standard Model is of interest and only left handed particles (right handed anti-particles) participate in those interactions, we can represent this fermionic structure as follows:

Leptons:

$$\begin{pmatrix} \nu_e^L \\ e_L^- \end{pmatrix} \qquad \begin{pmatrix} \nu_\mu^L \\ \mu_L^- \end{pmatrix} \qquad \begin{pmatrix} \nu_\tau^L \\ \tau_L^- \end{pmatrix} \tag{1.11}$$

Quarks:

$$\begin{pmatrix} u_L \\ d_L \end{pmatrix} \qquad \begin{pmatrix} c_L \\ s_L \end{pmatrix} \qquad \begin{pmatrix} t_L \\ b_L \end{pmatrix} \tag{1.12}$$

Each fermonic particle in the SM is accompanied by an anti-particle (not shown above). The electromagnetic and weak part of the SM were shown to originate from one fundamental interaction, the so-called electroweak interaction described in the Glashow-Weinberg-Salam model [25] [26], unifying both interactions above energies $\sim 100\,\mathrm{GeV}$.

1.3   Neutrino Interactions with Matter

In neutrino astronomy with IceCube it is important to understand interactions between the neutrinos and the matter constituents of the glacial ice. These are electrons and nucleons. Neutrino-electron scattering due to its small cross-section typically is negligible[1].

Neutrino-Nucleon Scattering - DIS
At energies which are of interest to IceCube ($E > 100\,\mathrm{GeV}$) all scatterings between the primary neutrino and the nucleons of the ice happen inelastically, which means,

---

[1]Neutrino electron scattering becomes important only in the vicinity of the Glashow Resonance at energies around $E_\nu = 6.3\,\mathrm{PeV}$

that the typical momentum transfer Q^2 to the nucleon target is such, that the nucleon fragments into hadrons ($Q^2 > 1\,\mathrm{GeV}^2$), which subsequently due to various strong interactions gives rise to a hadronic shower. Given such a momentum transfer, the process is well described by the parton picture of nucleons being composite objects made of non-interacting quarks. Hence in this regime neutrino nucleon scattering really means neutrino quark scattering and is referred to as Deep Inelastic Scattering (DIS, see figure 1.3).

From a fundamental point of view nucleons are to be regarded as dynamical objects. They consist of three valence quarks, which continuously interact strongly. Hence in addition to the valence quarks, a nucleon further consists of gluons, which mediate those interactions, and so-called sea quarks, which denote virtual quark anti-quark pairs, created in higher order interactions. Due to the asymptotic freedom in QCD, those interactions between the nucleon's constituents weaken with increasing Q^2. Above $Q^2 = 1\,\mathrm{GeV}^2$ they are negligible over the timescale of the scattering and hence during such an interaction the participating constituents (valence quarks and sea quarks) appear as non-interacting, free particles. In this approximation the nucleon structure then is independent of the momentum transfer Q^2. This is known as Bjorken scaling and becomes more and more accurate with increasing Q^2. An additional approximation, used to describe DIS processes, concerns the momentum of the interacting quark. Since for a fast moving nucleon the transverse momentum of its constituents is negligible compared to their longitudinal motion, the interacting quark is assumed to carry a fraction ξ of the total nucleon's momentum P with $p_q = \xi P$. For $Q^2 > 1\,\mathrm{GeV}^2$ this fraction ξ equals the Bjorken scaling variable $x = \frac{Q^2}{2Pq} = \frac{Q^2}{2M\nu}$. The last equality only holds in the rest frame of the proton, with M being its mass and ν denoting the energy, transferred from the neutrino to the proton system. The momentum fraction x is used to characterize the kinematic distributions of the nucleon's quark content in form of the parton distribution functions $f_i(x)$.

They describe the probability that the primary neutrino interacts with a quark of
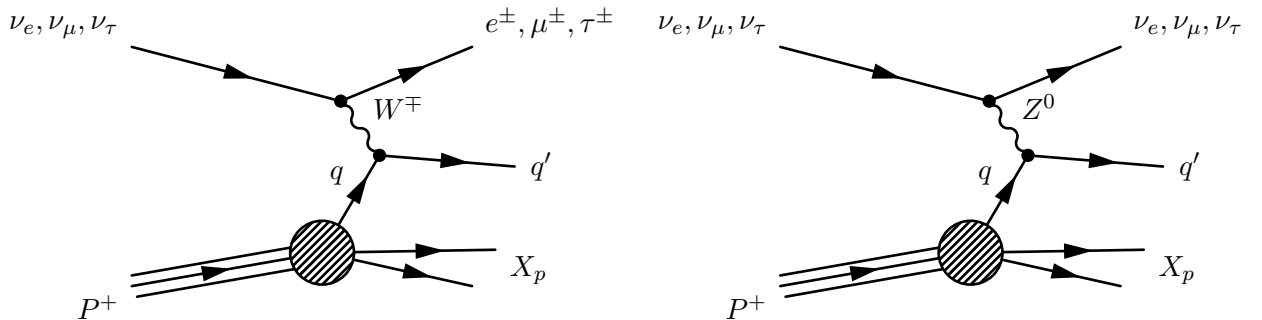
FIGURE 1.3: Deep Inelastic Neutrino Nucleon Scattering (leading order): Charged Current interaction via W-boson (left), Neutral Current interaction via Z boson (right).

type i carrying a momentum fraction x. They are normalized according to the valence quark content, with valence quarks being dominant in the region at large x and sea

quarks being important at low x. These distributions slowly vary with Q^2 in the region, where valence quarks dominate. Strong violations of Bjorken scaling exist in the region of small x [27].

In charged-current interactions (CC) the incoming neutrino interacts with the nucleon via $W^\pm$ exchange (left graph in figure 1.3). This results in an emerging charged lepton and the already mentioned hadronic shower. This is opposed to neutral-current interactions (NC) in which the scattering is mediated by the Z^0-boson. Here the neutrino simply exchanges momentum with the nucleon, which subsequently produces a hadronic shower and an outgoing neutrino (right graph in 1.3). The corresponding DIS cross-sections, a measure for the probability of these processes to happen, have been calculated using electroweak theory in [28]. In order to avoid treating neutrons and protons separately, they assumed iso-scalar nucleons $N := \frac{n+p}{2}$, which can be thought of being an admixture of the quark contents of both. Up to 10^4 GeV the cross-sections scale linearly with the incident neutrino energy [28]:

for CC-interactions (inclusive) $\nu_\ell N \rightarrow \ell^\pm + X$:

$$\frac{d^2\sigma}{dxdy} = \frac{2G_F^2 M E_\nu}{\pi} \left(\frac{M_W^2}{Q^2 + M_W^2} \right)^2 \left[xq\left(x, Q^2\right) + x\bar{q}\left(x, Q^2\right)(1-y)^2 \right] \qquad (1.13)$$

for NC-interactions (inclusive) $\nu_\ell N \rightarrow \nu_\ell + X$:

$$\frac{d^2\sigma}{dxdy} = \frac{2G_F^2 M E_\nu}{\pi} \left(\frac{M_Z^2}{Q^2 + M_Z^2} \right)^2 \left[xq^0\left(x, Q^2\right) + x\bar{q}^0\left(x, Q^2\right)(1-y)^2 \right] \qquad (1.14)$$

The cross-sections above are differential in the Bjorken variables x and $y = \frac{\nu}{E_\nu}$ with $\nu = E_\nu - E_\mu$ (for NC $\nu = E_\nu - E'_\nu$) being the energy lost to the nucleon in the lab frame. M and $M_{W/Z}$ denote the masses of the nucleon and the weak bosons respectively, with the Fermi constant $G_F = \frac{\sqrt{2}g^2}{8M_W^2} \approx 1.17 \times 10^{-5}$ GeV^{-2} being the coupling constant of weak interactions below the electroweak unification. $q, \bar{q}, q^0, \bar{q}^0$ denote different superpositions of parton distribution functions (see [28] for details). At PeV energies about 26% of the neutrino energy gets deposited into the hadronic shower ($\langle y \rangle = 0.26$) [29].

The parton distribution functions, used in the results given above, cannot be calculated analytically, so they have to be extracted from measurements and subsequently extrapolated into kinematic regions, that are not accessible by those experiments. The difficulty here lies in the fact that with increasing neutrino energy, interactions at small values of x (down to $x \sim 10^{-8}$ at 10^{12} GeV [30]) have to be described [31]. In a second step violations of Bjorken scaling, (i.e. the Q^2 dependence) have to be calculated by evolving the parton functions in Q^2 using the DGLAP equations. Important constraints come from the HERA electron-proton collider located at DESY in Hamburg. From their measurements parton distribution functions up to an equivalent of 54 TeV neutrino energy

have been extracted, covering the region $x \geq 10^{-5}$ [30]. Global fits to various experimental results are for example provided by the CTEQ Collaboration [32]. According to the CTEQ4-DIS parametrization the neutrino DIS cross-sections scale as follows in the range between $10^7 \, \mathrm{GeV} \leq E_\nu \leq 10^{12} \, \mathrm{GeV}$ above $E_\nu = 10 \, \mathrm{TeV}$ [28]:

$$\sigma_{tot} \left(\nu N \right) = 7.84 \cdot 10^{-36} \mathrm{cm}^2 \left(\frac{E_\nu}{1 \, \mathrm{GeV}} \right)^{0.363} \tag{1.15}$$

$$\sigma_{tot} \left(\bar{\nu} N \right) = 7.80 \cdot 10^{-36} \mathrm{cm}^2 \left(\frac{E_\nu}{1 \, \mathrm{GeV}} \right)^{0.363} \tag{1.16}$$

The uncertainty of UHE neutrino nucleon cross-sections due to different extrapolation schemes has been estimated to be within a factor of 2 [28]. One of those extrapolations is shown in figure 1.4. Below that threshold, they scale linearly with the neutrino energy.
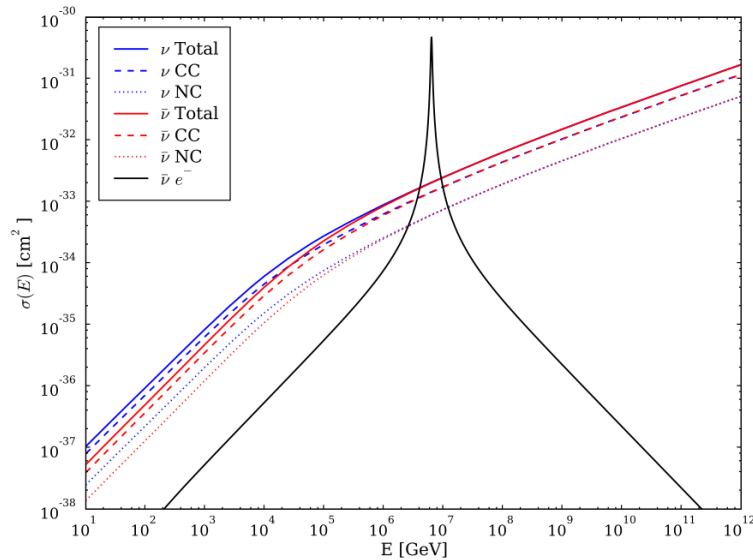
FIGURE 1.4: The figure shows the energy dependence of the neutrino-nucleon and neutrino-electron scattering cross-sections for neutrinos and anti-neutrinos respectively. The figure is taken from [33] and is based on data from [31]

Given a flux of high energy neutrinos, IceCube measurements may be able to constrain the uncertainty in the parton distribution functions using the fact that an isotropic flux of high energy astrophysical neutrinos is expected to produce a zenith dependent neutrino event rate in IceCube. This is because the interaction length $l_{int} = \frac{1}{n\sigma_{\nu N}}$ (with n being the number density of targets and $\sigma_{\nu N}$ denoting the neutrino-nucleon scattering cross section) remains constant with increasing zenith angle, while the distance, the neutrino would have to travel through the earth to reach the detection volume, increases. Since above $1 \, \mathrm{PeV}$ the earth becomes opaque for neutrinos, a clear asymmetry between the rates for up and down going neutrinos would allow to measure parton distribution functions at energies complementary and above the range of current collider experiments

[34]. Such a strategy however requires the analysis to provide enough zenith resolution in order to distinguish both directions. In this context this thesis provides a feasibility study by investigating the reconstruction performance of shower reconstruction algorithms at PeV energies, which are currently used in IceCube.

The Glashow Resonance

Neutrino-electron scattering typically is negligible compared to neutrino-nucleon scattering. However one exception exists. For electron anti-neutrinos, which scatter of electrons, a unique interaction channel exists. At an electron anti-neutrino energy of $E_{\bar{\nu}_e} = 6.3\,\mathrm{PeV}$, which corresponds to a center-of-mass energy of $E_{CMS} = M_W = 80.4\,\mathrm{GeV}$, resonant production of an on-shell W^- boson becomes possible, which then subsequently decays according to its decay modes (see table 1.5). This drastically enhances the neutrino interaction cross-section and can be thought of being an inverse muon decay, which was first suggested by Sheldon L. Glashow in 1960 [35]. This resonance thus manifests itself as a sharp peak in the neutrino-electron cross-section shown in figure 1.4. The process is visualized in the respective Feynman graph in figure 1.5.

W^- Decay Modes	Fraction(Γ_i/Γ_{tot})
$e^- \bar{\nu}_e$	$(10.75 \pm 0.13)\,\%$
$\mu^- \bar{\nu}_\mu$	$(10.57 \pm 0.15)\,\%$
$\tau^- \bar{\nu}_\tau$	$(11.25 \pm 0.27)\,\%$
hadrons	$(67.60 \pm 0.27)\,\%$
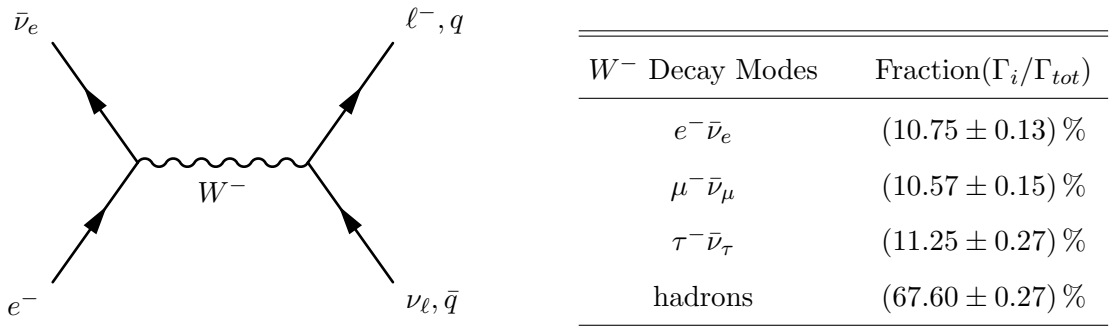
FIGURE 1.5: Glashow Resonance: (Left) resonant s-channel scattering between electron anti-neutrino and electron, tree level. (Right) the respective branching ratios, determined by the W^--decay, are given in the table.

The respective cross-sections are given by [29]:

for $\bar{\nu}_e e \to \bar{\nu}_\mu \mu$:

$$\frac{d\sigma}{dy}\left(\bar{\nu}_e e \to \bar{\nu}_\mu \mu\right) = \frac{G_F^2 m E_\nu}{2\pi} \frac{4\left(1-y\right)^2 \left(1 - \left(\mu^2 - m^2\right)/2mE_\nu\right)^2}{\left(1 - 2mE_\nu/M_W^2\right)^2 + \Gamma_W^2/M_W^2} \quad (1.17)$$

for $\bar{\nu}_e e \to hadrons$:

$$\frac{d\sigma}{dy}\left(\bar{\nu}_e e \to hadrons\right) = \frac{d\sigma}{dy}\left(\bar{\nu}_e e \to \bar{\nu}_\mu \mu\right) \cdot \frac{\Gamma\left(W^- \to hadrons\right)}{\Gamma\left(W^- \to \bar{\nu}_\mu \mu\right)} \quad (1.18)$$

with m and μ being the masses of electron and muon respectively.

Since the decay widths into charged leptons are pretty similar, the cross-sections for electron and tau production are almost the same as the cross section for muon production. The total resonant cross-section $\bar{\nu}_e e \to anything$ is about 360 times higher than the charged-current neutrino-nucleon cross-section at this energy [29]. However due to the small width of the resonance ($\Gamma_W = 2.05\,\text{GeV}$ [36]) the cross-section rapidly drops below the DIS cross-section for energies different from $E_\nu = 6.3\,PeV$. The main decay channel of the W^- into hadrons ($\sim 70\%$) does not produce a secondary neutrino in the final state. Hence the primary electron antineutrino deposits almost all its energy in the detector.

Experimentally the Glashow Resonance has not yet been observed. Due to the lack of artificial neutrino sources reaching far enough in energy, searches for that resonance would have to rely on the natural neutrino abundance. Although not being discovered yet, the existence of a flux of high energetic astrophysical neutrinos is expected from various models describing for example cosmic ray acceleration. Hence a discovery of the Glashow Resonance in IceCube would potentially imply two achievements at the same time: the confirmation of a 50 year old prediction and the first observation of high energetic astrophysical neutrinos. The study of the reconstruction performance of current reconstruction algorithms at the energy of the resonance, done in this thesis, is a starting point for such a search.

1.4 Extraterrestrial Neutrino Flux

The accelerated protons are still subject to interactions with the particle content of the respective source, while being confined to the source region. These reactions produce mesons (mainly pions) which subsequently decay giving rise to a flux of high energetic astrophysical neutrinos.

$$\pi^+ \to \mu^+ + \nu_\mu \tag{1.19}$$

$$\pi^- \to \mu^- + \bar{\nu}_\mu \tag{1.20}$$

The muons further decay via $\mu^+ \to e^+ + \nu_e$ and $\mu^- \to e^- + \bar{\nu}_e$. Since the neutrinos are unaffected by magnetic fields, they leave the source after production. The flavor ratios of those neutrinos depends upon the ratio between the charged pions $\pi^\pm$, which in turn depends on the source properties, determining the proton interactions during acceleration. Among several models, which appear in the literature, for example [12], two limits are most often used to discuss the implications for an experiment on earth:

the pure *pp* source and the *pγ* source, which is assumed to be optically thin to neutrons [12] [29]. In a *pp* source, the following interactions are assumed to dominate:

$$p + p \rightarrow N \left[\pi^0 + \pi^+ + \pi^- \right] + X \tag{1.21}$$

with N being the multiplicity of the secondary pions [1]. This yields a flavor composition at the source of $(\nu_e, \nu_\mu, \nu_\tau,) = (\bar{\nu}_e, \bar{\nu}_\mu, \bar{\nu}_\tau) \approx (1, 2, 0)$ which due to neutrino oscillation over the large distance from source to the earth turns into $(\nu_e, \nu_\mu, \nu_\tau,) = (\bar{\nu}_e, \bar{\nu}_\mu, \bar{\nu}_\tau) \approx (1, 1, 1)$ [29]. In the case of photo-meson production in a *pγ* source the situation is different. Protons are assumed to interact via the Δ-resonance with the light fields present in the source [12].

$$p + \gamma \rightarrow \Delta^+ \rightarrow \begin{cases} n + \pi^+ & \frac{1}{3} \text{ of all cases} \\ p + \pi^0 & \frac{2}{3} \text{ of all cases} \end{cases}$$

This yields a flavor distribution at the source of $(\nu_e, \nu_\mu, \nu_\tau,) = (1, 1, 0)$ and $(\bar{\nu}_e, \bar{\nu}_\mu, \bar{\nu}_\tau) = (0, 1, 0)$. This changes to $(\nu_e, \nu_\mu, \nu_\tau,) \approx (0.78, 0.61, 0.61)$ and $(\bar{\nu}_e, \bar{\nu}_\mu, \bar{\nu}_\tau) \approx (0.22, 0.39, 0.39)$ at earth [29]. It is important to note that those two source models differs with respect to the predicted ratio $\hat{T} = \frac{\Phi_{\bar{\nu}_e}}{\Phi_{\nu_\mu} + \Phi_{\bar{\nu}_\mu}}$ between the fluxes of electron antineutrinos and muon (anti-)neutrinos at earth [12].

Suppose the fraction ϵ of the proton energy, which is deposited in the produced pion during such collisions, is a constant (independent of the proton energy). Then the primary neutrino spectrum follows the proton spectrum at the source, as expected from shock acceleration [37].

$$E_\nu^2 \frac{dN_\nu}{dE_\nu} \approx \frac{\epsilon}{4} t_H E_{CR}^2 \frac{dN_{CR}}{dE_{CR}} \tag{1.22}$$

Here $t_H \approx 10^{10}$ a denotes the Hubble time. N_{CR} and E_{CR} denote the amount and energy of cosmic ray particles. The reduction by a factor of $\frac{1}{4}$ in addition to $\epsilon \approx 0.05$ is due to neutral pions (do not contribute to neutrinos) being produced at equal rate as charged pions during *pγ* encounters. In addition half of the pion energy gets deposited in the muon neutrino during decay [37]. Expression (1.22) overestimates the neutrino flux in the case of sources, that are dominated by *pp* interactions [38]. However the neutrino spectrum should still follow the proton spectrum. These considerations can be used to derive a theoretical constraint on the diffuse astrophysical neutrino flux, also known as the Waxman-Bahcall upper bound, which does not depend on detailed models of different sources (AGNs,GRBs, etc.). Given a cosmic ray generation rate of $E_{CR}^2 = 10^{44} \, \text{erg} \, \text{Mpc}^{-3} \, a^{-1}$ the subsequent neutrino flux should not exceed the following

value [37]:

$$E_\nu^2 \phi_{\nu_i} = \frac{\epsilon \xi_z}{2} \cdot 1.5 \cdot 10^{-8} \, \mathrm{GeV \, cm^{-2} s^{-1} sr^{-1}} \tag{1.23}$$

$$\phi_{\nu_i} \in \left\{ \phi_{\nu_e}, \phi_{\nu_\mu}, \phi_{\bar{\nu}_\mu} \right\} \tag{1.24}$$

The factor ξ_z accounts for redshift corrections and the fact that the universe at earlier times may have had an enhanced cosmic ray production rate. Depending on the evolution of the neutrino energy generation rate with redshift z, ξ_z was found to vary from $\xi_z \approx 3.0$ to $\xi_z \approx 0.6$ [37]. The bound also applies to *pp* dominated sources [38].

A diffuse flux is important in searches for astrophysical neutrinos, since, although single sources of neutrinos may be to weak to be observed, the cumulative diffuse flux of a collection of sources might be detectable [39]. The general strategy in such searches is to look for a hardening in the observed neutrino spectrum. Conventional atmospheric neutrinos, produced in pion and kaon decays in the atmosphere, follow a power law with $\gamma = 3.7$. At higher energies a so-called prompt contribution to the atmospheric neutrino flux from the decays of charmed mesons is expected to follow the harder cosmic ray spectrum at earth with $\gamma = 2.7$. Prompt neutrinos should dominate the atmospheric flux for $E_\nu > 30 \, TeV$ and are yet to be observed [39]. However both are significantly softer then the expected astrophysical spectrum with $\gamma = 2.0$, as discussed above. In
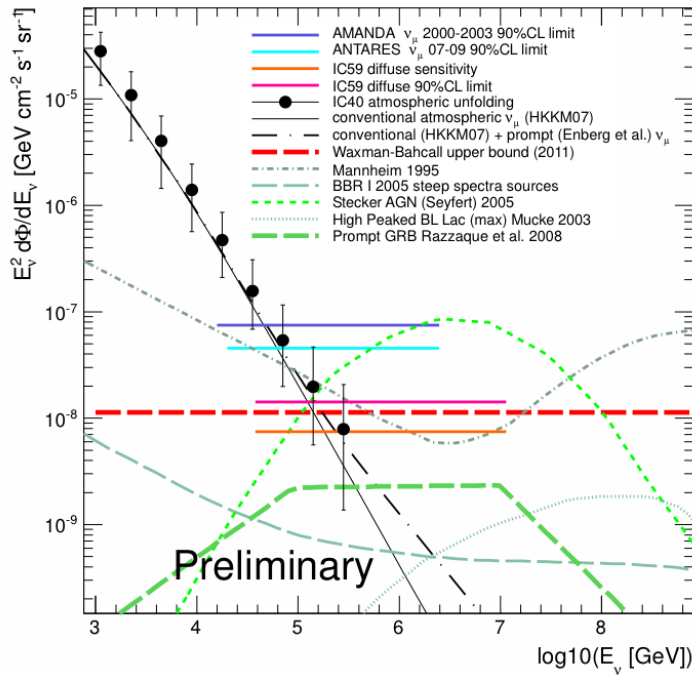
FIGURE 1.6: The figure shows the upper limits on an astrophysical ν_μ flux based on an assumed spectrum of E^{-2} as derived by several neutrino detectors. These limits can be compared to various theoretical predictions. Furthermore the measured flux of atmospheric muon neutrinos and its expectations are shown. (Figure from [40])

IceCube such searches are performed in the track channel being sensitive to muon neutrinos and the cascade channel, being an all-flavor search. By using data accumulated with the IceCube detector in its partial IC-22 (22 strings) configuration, a cascade analysis yielded an diffuse upper limit of $E^2\phi_{90\%CL} < 3.6 \times 10^{-7}\,\mathrm{GeV\,cm^{-2}\,s^{-1}\,sr^{-1}}$ at the 90% confidence level. This analysis assumed a flavor ratio $\nu_e : \nu_\mu : \nu_\tau$ on earth of 1:1:1 [39] and was sensitive at neutrino energies between 24 TeV and 6.6 PeV. Based on measurements in the track channel (ν_μ) with IceCube in its larger IC-59 (59 strings) configuration, a preliminary upper limit on the diffuse flux of muon neutrinos has been set at $E^2\phi_{90\%CL} < 1.4 \times 10^{-8}\,\mathrm{GeV\,cm^{-2}\,s^{-1}\,sr^{-1}}$ [40]. The current status of searches for diffuse fluxes of astrophysical neutrinos in the muon channel, as well as in all-flavor searches, is summarized in figure 1.6 and compared to flux predictions of various models. It was recently argued that a diffuse flux of astrophysical neutrinos - given it is strong enough - is likely to emerge from the background of atmospheric neutrinos in the PeV range (see Figure 1.6), which would then be close to the Glashow Resonance [29]. Hence this resonance provides a promising opportunity to search for a diffuse flux of astrophysical neutrinos due to its enlarged cross-section. Despite the enhanced cross-section the Glashow Resonance provides additional unique features, which will be very interesting, once a flux of such neutrinos has been discovered. Only electron anti-neutrinos have the chance to interact via this resonance. Due to this asymmetry IceCube should have sensitivity to the electron neutrino to anti neutrino ratio, which otherwise is impossible to distinguish. Thus by determining the measured ratio $\hat{T}$ at the Glashow Resonance, statements about the asymmetry in the abundance of the charged pions in the source region can be made, which may allow the identify the underlying dominant interactions pp or $p\gamma$ [12]. If the corresponding fluxes of neutrinos are strong, it my even be possible
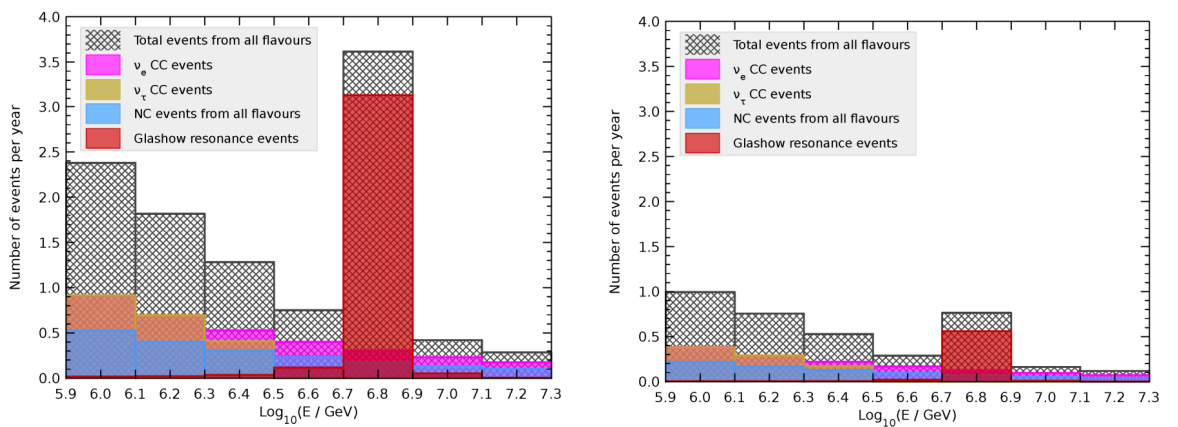
FIGURE 1.7: **Glashow Resonance Eventrates:** Energy distribution of shower events in IceCube at PeV energies for the case of pure pp-sources (left) and pure $p\gamma$-sources (right). The Glashow Resonance is shown in red. (Figure from [29])

to separate both scenarios based on the energy distributions of the associated showers in

IceCube, as shown in Figure 1.7 for pure *pp*-soures (left) and for pure *pγ*-sources being dominant (right) [29]. The Glashow Resonance thus provides an interesting channel to look for astrophysical neutrinos. With the recent observation of two neutrino induced $\sim 1\,\mathrm{PeV}$ particle showers [41], IceCube has already entered the era of PeV scale neutrino physics. The discovery potential w.r.t. astrophysical neutrino fluxes of PeV neutrino events is reflected in the fact, that, not including systematic uncertainties, those two events already imply a preliminary 2.9σ deviation from the conventional atmospheric neutrino background expectation [41].

Chapter 2

Neutrino induced Cascades

This chapter covers the processes that give rise to the observable signatures of interest in IceCube, which for the purpose of this thesis are the properties of neutrino induced particle showers in the ice. Two different kinds of such showers can be distinguished. An electromagnetic shower is produced when an incoming electron neutrino (electron anti-neutrino) produces an electron (positron) in a charge current interaction. In contrast, whenever a neutrino of any flavor interacts with a nucleon via the neutral current channel, a hadronic particle shower is initiated. None of those showers is purely electromagnetic or purely hadronic. First, the electromagnetic cascade, emerging from a CC interaction, is contaminated with a hadronic contribution due the nucleon being fragmented. Second, any hadronic cascade contains an electromagnetic component due to electrons, positrons and high energetic photons being produced, when secondary pions decay. For simplicity, purely electromagnetic cascades will be considered first to introduce shower development in general. In a next step the different phenomenology of hadronic cascades will be discussed.

2.1 Passage of Electrons through Matter

An electromagnetic cascade is produced by the primary electron or positron via its energy loss in the ice. These mechanisms will be discussed in this section.
When an electron propagates through a medium such as ice, it interacts via different channels with the particle constituents of the ice. First of all, the primary electron may elastically scatter off a nucleus in the ice resulting in a change of its direction, while not loosing energy. But given that this process is strongly forward peaked at IceCube energies [42], it can safely be ignored. Secondly in inelastic Coulomb interactions the

incoming electron can excite an electron in the atom into a different state or even ionize the atom by providing more than the binding energy to the atomic electron. Both processes reduce the energy of the primary electron. In addition, during an electromagnetic encounter the electron might emit a high energetic photon in a process called Bremsstrahlung, dominating at high energies.

Excitation and Ionization

Energy losses of the primary electron through excitation and ionization of atoms in the medium can be described using the 'mean stopping power' formula, which was derived by Hans Bethe in the late 1920s based on the cross-section for Moller scattering. Thus it is only valid at high incident electron energies, when the typical energy transfer is large compared to the binding energy of the target electron in the atom [42]:

$$L_{ion}(E) \equiv -\frac{dE}{dx} = \frac{2\pi N Z e^4}{mv^2} \left\{ \ln\left[\frac{(\gamma+1)E^2}{2I^2} \right] - \left(\frac{2}{\gamma} - \frac{1}{\gamma^2} \right) \ln 2 + \frac{1}{\gamma^2} + \frac{1}{8}\left(1 - \frac{1}{\gamma}\right)^2 - \delta \right\}$$

(2.1)

with N being the number density of atoms in the material being transversed. The γ-factor is defined as usual $\gamma = \left(\sqrt{1 - \frac{v^2}{c^2}} \right)^{-1}$; m and v denote the mass and velocity of the primary electron, while Z and e are the atomic number and the elementary charge respectively. The mean excitation energy I depends on the material. The δ-correction term accounts for the so called density effect. An electron passing through the medium with dielectric constant ϵ_r polarizes it, thus altering its subsequent interactions. For highly relativistic electrons $\gamma \gg 1$ it contributes as follows [42],

$$\delta = \ln\left[\frac{\gamma^2 (\hbar\omega_p)^2}{I^2} \right] - 1,$$

(2.2)

with $\omega_p = 4\pi \frac{e^2 N Z}{m}$ being the plasma frequency of the atomic electrons in the medium. In this limit the energy loss becomes independent of the mean excitation energy I, thus describing ionization only. The ejected electron ("knock-on electron") can carry up to 50% of the primary electron. These so called δ-rays can still contribute to an electromagnetic shower [42]. However in water or ice most of them are produced at energies below the Cherenkov threshold ($E_{th} \approx 0.26\,\mathrm{MeV}$ [43]) and hence do not contribute to the light, visible in a Cherenkov detector.

Bremsstrahlung

The most important energy loss of the primary electron at energies relevant for IceCube is given by bremsstrahlung, which was first described by Walter Heitler and Hans Bethe. The cross-section (differential in photon energy) takes the following form in the extreme

relativistic limit $\gamma \gg 1$ [42]:

$$\frac{d\sigma}{dE_\gamma} = 2\alpha Z^2 \left(\frac{e^2}{mc^2}\right)^2 \frac{1}{E_\gamma} \left[1 + \frac{E_0'^2}{E_0^2} - \frac{2E_0'}{3E_0}\right] \left[2\ln\frac{2E_0 E_0'}{mc^2 E_\gamma} - 1\right] \tag{2.3}$$

with $E_0 = E_{kin} + mc^2$ being the total energy of the incident electron. $E_0' = E_0 - E_\gamma$ denotes the total energy of the scattered electron, with E_γ being the energy of the radiated photon. The fine structure constant is given by α.

Hence the probability of radiating a bremsstrahlungs photon decreases with increasing mass of the charged primary particle. Moreover from this relation it can be shown that the energy loss rate is approximately proportional to the energy of the electron

$$L_{rad}(E) \equiv \frac{dE}{dx} \approx \frac{-E}{X_0} \tag{2.4}$$

$$E(x) = E_0 \exp\left(-\frac{x}{X_0}\right) \tag{2.5}$$

Here x describes the amount of material which was transversed: $x = l\rho$, with ρ being the mass density of the material. The mean radiation length is denoted by X_0[1]. It can approximately be parametrized [42]:

$$\frac{1}{X_0} = 4N_g \alpha Z (Z+1) \left(e^2/mc^2\right)^2 \ln\frac{183}{Z^{1/3}} \tag{2.6}$$

with N_g being the atomic density of the target ($[N_g] = g^{-1}$).

The number of bremsstrahlungs photons, which are produced per unit of transversed material (g/cm^2) with energies $E \in [E_1, E_2]$, then is [42]

$$\frac{dN}{dE}(E_1, E_2) = \frac{2L_{rad}(E)}{E} \left[\ln\frac{E_2}{E_2} - \frac{E_2 - E_1}{E}\right] \tag{2.7}$$

The transition for bremsstrahlung to become dominant over ionization losses happens in the MeV regime.

2.2 Electromagnetic Showers

In this section the basic properties of electromagnetic shower development in ice will be described. Highly energetic electrons loose energy through radiation of photons during momentum exchange with nucleons. These γ-rays are a key ingredient in the development of a cascade. In the vicinity of the electric field of a nucleon, the photon is able to deposit all its energy into the production of an electron-positron pair in a process called

---

[1]For water (and ice) the radiation length for bremsstrahlung is $X_0 = 36\,\text{g/cm}^2$.

pair-production. The electric field of the nucleon is needed for this process in order to become kinematically possible. These processes, energy loss via bremsstrahlung and subsequent bremsstrahlung, will iteratively be repeated, thus forming an electromagnetic cascade.

Pair-Production

The photon needs to possess enough energy to create an electron positron pair. If the momentum conservation is assured due to electromagnetic scattering with a heavy particle (i.e. the nucleus), the threshold energy for pair production is given by the rest masses of the created particles $E_\gamma^{th} = 2m_e c^2$. It was shown by Walter Heitler, that in the high energy limit the pair production cross-section in the vicinity of a nucleon becomes a constant [42]

$$\lim_{E \to \infty} \sigma_{pair}^{nuc} = \alpha Z^2 \left(e/mc^2\right)^2 \frac{28}{9} \left[\ln \frac{183}{Z^{1/3}} - \frac{1}{42}\right] \tag{2.8}$$

If one also includes pair-production in the vicinity of the Coulomb field of electrons in the target (possible for $E_\gamma > 4m_e c^2$), the Z^2 prefactor in eq. (2.8) has to be replaced by $Z(Z+1)$ [42]. Neglecting the second term in eq. (2.8), the high energy limit of the cross-section can be expressed in terms of the bremsstrahlung's radiation length (2.6). It is given by [44]

$$\sigma_{pair}^{tot} = \frac{7}{9} \frac{1}{N_g X_0} \tag{2.9}$$

Hence the interaction length of pair-production L_{pair} and the radiation length of bremsstrahlung X_0 are closely related $L_{pair} = \frac{9}{7} X_0$.

A simplified Model for electromagnetic Cascades

Cascade development is typically treated using Monte-Carlo simulations due to its highly stochastic nature. However a better insight is provided by approaching the problem approximately in an analytic manner. A first description of shower development was given by Walter Heitler in 1937 [45]. The simplest of his models [46] shall be summarized here. As described, the number of particles (electrons, positrons and photons) in the shower increases with the distance transversed by the primary particle, mainly due to bremsstrahlung and pair production. This is only true until the energy of the particles inside the shower drops below some critical energy E_c, since the cross-sections for both processes decrease with energy and other energy loss mechanisms become important. This threshold can be defined as the energy at which the energy loss over one radiation length equals the electron energy. The critical energy can be parametrized (for solids)

as follows [44]:

$$E_c = \frac{610\,\text{MeV}}{Z + 1.24} \tag{2.10}$$

The critical energy for ice is $E_c = 80\,\text{MeV}$ [33].

Now following [46] consider an incident high energetic electron with energy E_0. It is assumed that this electron radiates a photon with energy $E_\gamma = \frac{1}{2}E_0$ after having transversed one splitting length $d = X_0 \ln 2$, which corresponds to the distance, after which the electron has lost half of its energy. In the next iteration the the photon creates an electron-positron pair over the same splitting length[2]. This process is visualized in Figure 2.1. It repeats until the energy of the particles inside the shower reaches the critical energy, where the shower is assumed to stop. This is visualized in Figure 2.1. After n steps the shower consists of in total $N_p = 2^n$ particles (electrons, positrons and
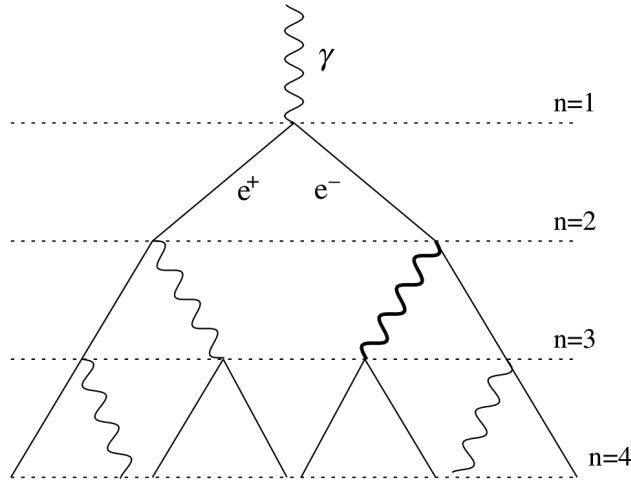
FIGURE 2.1: The figure shows a simplified model of electromagnetic shower development (Figure from [46])

photons). The length of the shower then amounts to $L = n\frac{X_0}{\rho} \ln 2$. The primary electron energy E_0 can be related to the critical energy using the maximum number of iterations n_{max}:

$$E_0 = E_c N_p = E_c 2^{n_{max}} \tag{2.11}$$

The shower maximum is thus reached at

$$L_{max} = \frac{X_0}{\rho} \ln \frac{E_0}{E_c} \tag{2.12}$$

From there on can give a rough estimate of the length of a $1\,\text{PeV}$ cascade in ice $(\left(\frac{X_0}{\rho}\right)_{ice} = 39.3\,\text{cm}$ [44], $E_c^{ice} = 80\,\text{MeV})$ of $L_{max}^{ice}(1\,PeV) \sim 6.4\,\text{m}$. The key features

---

[2]reminder: bremsstrahlung and pair production have almost the same radiation length

of this model are, that amount of secondary particles in the shower at its maximum is proportional to the primary energy E_0, and that the length of the shower increases logarithmically with the primary energy E_0. While overestimating the number of charged particles of the shower, the position of the shower maximum was shown to agree well with simulations [46]. Finally since the number of Cherenkov photons emitted per charged particle and splitting length N_γ^d is a constant for highly relativistic particles (eq. (2.19)), the model predicts that the primary energy E_0 of such a cascade is proportional its total Cherenkov light yield N_γ, and vice-versa [47]:

$$E_0 \approx \frac{3}{4} \frac{E_c}{N_\gamma^d} N_\gamma^{tot} \tag{2.13}$$

The linear relationship between cascade energy E_0 and light yield N_γ is extensively used during event reconstruction.

As final remark: it was shown in simulation that the longitudinal energy loss of a cascades in units of the radiation length $t = \frac{x}{X_0}$ is better approximated by a gamma distribution [44].

$$\frac{dE}{dt} = E_0 b \frac{(bt)^{a-1} e^{-bt}}{\Gamma(a)} \tag{2.14}$$

For water the following parameters hold: $a = 2.03 + 0.604 \ln \frac{E_0}{GeV}$ and $b = 0.633$ [48].

2.3 Hadronic Showers

The description of hadronic showers is more involved, since in addition to the electromagnetic processes, hadronization needs to be considered. First the light yield of a hadronic cascades is smaller than the light yield of an electromagnetic cascade with the same energy, since in hadronic cascades some of the energy gets deposited into neutrons, as well as in binding energies during hadronization processes [49]. Furthermore the Cherenkov threshold for hadrons is larger than for electrons or positrons, since they have a larger mass. The main contribution to hadronic cascades comes from pion ($\pi^\pm$, π^0) production and decay. A simplified model analogous to the electromagnetic case above has been derived in [46]. Since neutral pions decay almost instantaneous into a pair of gamma-rays after their production, they introduce an electromagnetic component into the hadronic shower, which becomes more and more important with increasing shower energy [49]. For the purpose of IceCube most of the subtle details of hadronic physics in the shower can be neglected and hence hadronic cascades are modeled in a first approximation as electromagnetic cascades with a reduced light yield [50], which can be described by

downscaling the energy of a hadronic shower compared to an electromagnetic shower.

$$F = \frac{E_{had}}{E_{em}} \tag{2.15}$$

This scaling is energy dependent, since the amount of neutral pions in the shower increases with increasing shower energy. It is shown in Figure 2.2.
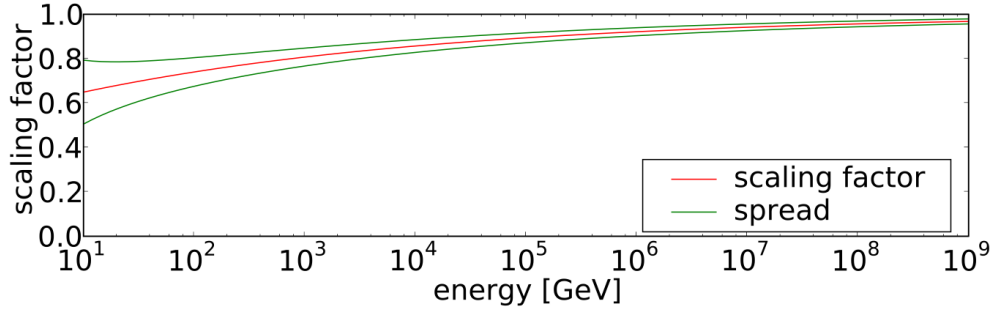
FIGURE 2.2: Energy dependence of the relative fraction of the light yield of a hadronic cascade w.r.t an electromagnetic cascade of the same energy. The redline corresponds to the best fit, while the green lines mark the 1σ error band (Figure from [50])

2.4 Vavilov-Cherenkov Radiation

Cherenkov light is radiated, when charged particles propagate through a medium with refractive index $n = \sqrt{\epsilon_r}$ (ϵ_r: dielectric constant) at a speed, exceeding the phase velocity of light $c_n = \frac{c_0}{n}$ (c_0: vacuum speed of light). This emission was first observed by Pavel A. Cherenkov in 1934 [51], who had sent fast electrons through purified liquids. Such fast moving electrons polarize the atoms close to their track. During relaxation those atomic electrons get accelerated and radiate [52]. It was shown by I. M. Frank and I. E. Tamm that constructive interference of this coherent emission takes place for $v_p > c_n$ (v_p: velocity of the charged particle). The predicted properties of that radiation showed good agreement with Cherenkov's observations [51].

Tamm considered a point charge being at rest at $z = -z_0$ for $t < -t_0$ [53]. This charge then moves at a constant velocity v in the time interval $-t_0 < t < t_0$. At $t = t_0$ the particle stops at $z = z_0$. By looking at the emitted energy, he found bremsstrahlung for the instantaneous acceleration and deacceleration. In case of $v > c_n$ an additional contribution appeared, which was identified with the Cherenkov radiation. The corresponding energy loss (differential in frequency and length) scaled as follows [53]:

$$\frac{d^2E}{d\omega dx} \propto \left(1 - \frac{1}{\beta^2 n^2}\right) \tag{2.16}$$

with β being the velocity measured in units of the vacuum speed of light $\beta = \frac{v_p}{c_0}$.

The amount of radiated energy per unit length increases with the frequency ω. Hence in an optical medium transparent at optical frequencies, Cherenkov light will be most intense in the blue and near UV region. The amount of radiated photons per unit length and frequency can be expressed as [44]:

$$\frac{d^2 N_\gamma}{d\lambda dx} = \frac{2\pi\alpha}{\lambda^2}\left(1 - \frac{1}{\beta^2 n\left(\lambda\right)^2}\right) \tag{2.17}$$

This is the so called Frank-Tamm-equation. The angular emission profile was shown to be sharply peaked at the Cherenkov angle θ_c [53]. With increasing track length, the emission profile peaks more and more at θ_c, until it behaves like $\delta\left(\cos\theta_c - \frac{1}{n\beta}\right)$ for an infinite track $(\omega t_0 \to \infty)$ [53]. The Cherenkov angle is thus given by [44]:

$$\cos\theta_c = \frac{1}{n\beta} \tag{2.18}$$

For a highly relativistic particle $(\beta \approx 1)$ this yields $\theta_c \approx 41°$ in ice $(n_{ice} \approx 1.33$ [50]). Whereas the angular emission profile (i.e. the Cherenkov angle) provides the basis for the reconstruction of directional information of a particle shower, the energy can be estimated by convolving the radiated number of photons with the spectral acceptance of the detector. Using equation (2.17) and neglecting dispersion, one can estimate the number of radiated Cherenkov photons per unit length in an interval $\lambda \in [\lambda_1, \lambda_2]$ to:

$$\frac{dN_\gamma}{dx} = 2\pi\alpha\left(1 - \frac{1}{\beta^2 n^2}\right)\frac{\lambda_2 - \lambda_1}{\lambda_1\lambda_2} \tag{2.19}$$

Hence the the number of photons per unit length is constant. The energy loss due to Cherenkov emission is neglectable compared to collisional or radiative losses [42].

Chapter 3

The IceCube Detector

This section shall describe how the design of the IceCube detector allows to measure the Cherenkov light caused by the charged secondary particles, created when a neutrino interacts with the glacial ice, and how information about the incident particles can then be deduced from that signals.

3.1 Design of the IceCube Array

The IceCube Detector consists of 5160 DOMs (Digital Optical Modules), which are distributed among 86 strings, which have been deployed into the ice by using a hot water drilling technique. The 86 strings, which connect to the counting house in the center of the array and provide power and communication to each of its 60 DOMs, have then been lowered into those holes until the DOMs reached their final position between 1450 m to 2450 m below the surface of the glacial ice. The geometry of IceCube is based on a triangular grid (shown in Fig. 3.1). The distance between closest strings amounts to ~ 125 m, whereas DOMs on the same string have a spacing of 17 m [1].

There are two reasons why it is beneficial to deploy the DOMs at the large depths mentioned above. First, the 1450 m layer of ice above the DOMs lowers the muon background and second, more important, at larger depths IceCube profits from the improved optical quality of the ice, since above 1400 m the ice is contaminated with small air bubbles of about $50\,\mu$m diameter, which significantly reduces the scattering length of light [1]. Unfortunately this not true for the small region between ~ 2000 m and ~ 2100 m, the so-called dust layer, with a high concentration of dust particles, thus enhancing scattering and absorption.
There exists a subarray of 15 "DeepCore (DC)" strings (marked green in Figure 3.1)
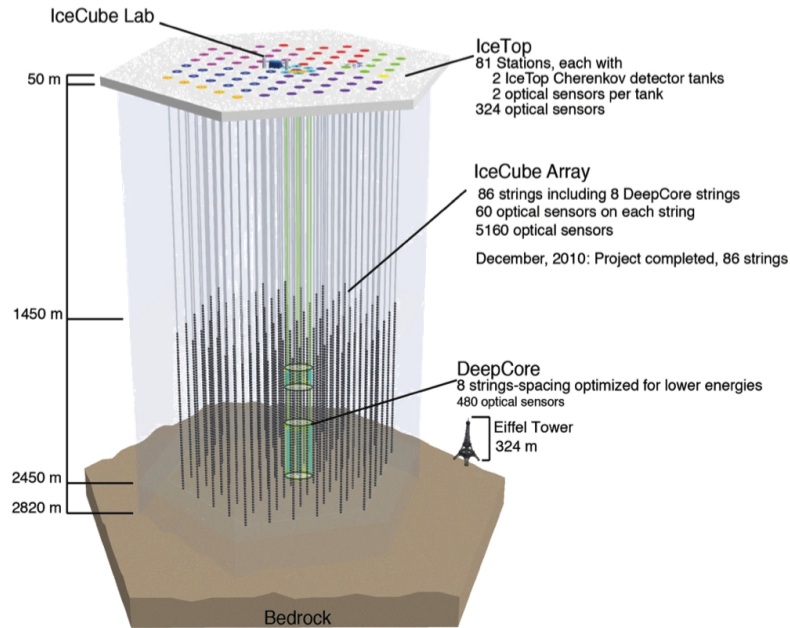
FIGURE 3.1: In total 5160 DOMs, distributed over an cubic kilometer of arctic ice, make up the instrumented volume of the IceCube Detector. The IceCube extension DeepCore is shown in green (Figure from [1]).

among the 86 IceCube strings, which have a denser population of DOMs (down to 7 m vertical distance) and a smaller inter string distance (down to 42 m) than regular IceCube strings. The DeepCore gap visible in Figure 3.1 is due to the dust layer mentioned above. The PMTs in the DC DOMs of the 8 closest DC strings, deployed at the largest depths to take advantage of the clearest ice, have a 35% higher quantum efficiency than the regular IceCube PMTs.

The very top of IceCube, the surface of the arctic ice shield, is instrumented as well. Two Cherenkov tanks with two standard IceCube DOMs each have been placed on top of each IceCube string. These tanks make up an extensive air shower array called IceTop [54], which indirectly measures the cosmic rays themselves. IceTop improves IceCube's extra terrestrial neutrino physics related capabilities by providing a possibility to veto events accompanied by atmospheric air showers.

To specify the position of events in the detector a coordinate system is needed. The "IceCube coordinate system" is defined as follows. It has its origin close to the center of the detector array at a depth of 1948.07 m with the z-axis being normal to the ice surface, while pointing upwards. The y-axis is aligned along the prime meridian towards Greenwich (UK). The system is right-handed. The zenith angles θ and azimuth Φ are defined by the direction of the possible source of the measured particles, i.e. its arrival direction. This definition is visualized in figure 3.2.
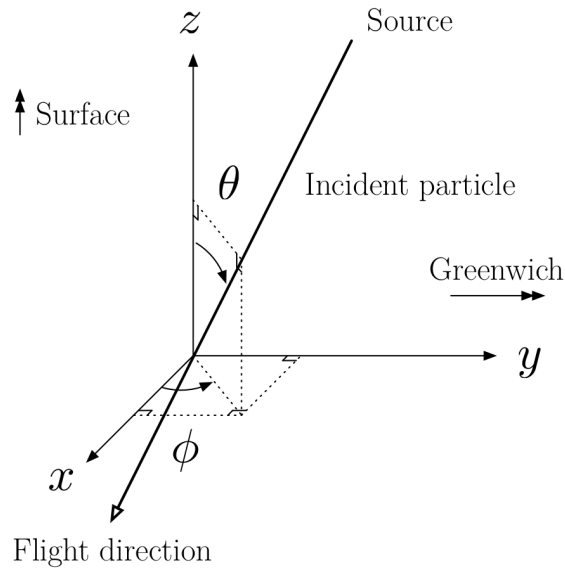
FIGURE 3.2: The IceCube coordinate system. (Figure from [55])

3.2 The Digital Optical Modules

The measurement in IceCube is done in single instrumentation units, called Digital Optical Modules (DOMs). Its heart is a $25\,cm$ diameter photomultiplier tube (PMT), the R7081-02, which was manufactured by the Hamamatsu Corp. A schematic view of a standard IceCube DOM is given in Figure 3.3.
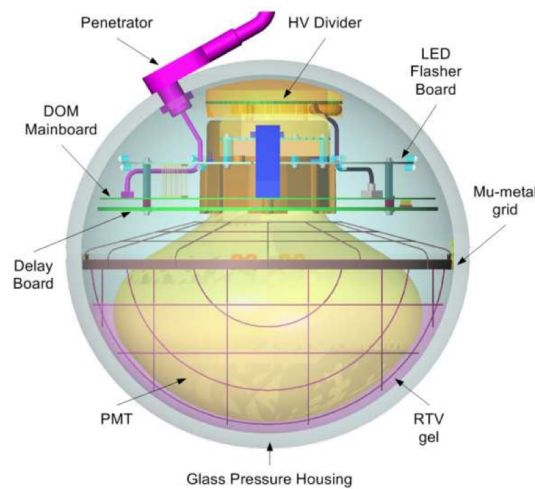
FIGURE 3.3: The figure shows the structure of the standard DOM used in IceCube. A photomultiplier tube, which is served by a high voltage divider, connects to the DOM main board, which takes care about signal recording and digitization. The DOM is bounded by a pressure sphere of glass, containing a flexible gel providing an optical coupling to the PMT (Figure from [1]).

The DOM is bounded by a borosilicate glass sphere with a diameter of $33\,cm$. In order to be able to withstand the pressure of an ice layer of more than $1400\,m$ thickness as

well as to withstand the pressure occurring during refreezing, the glass boundary itself has a diameter of 1.3 cm [56]. Therefore this sphere can be used in environments with a pressure up to 70 Mpa [1]. The optical properties inside the DOM are given by a flexible gel, which holds the DOM electronics, which in addition to the PMT consists of the DOM main board, controlling the whole recording and digitization procedure, a high voltage divider, providing the power needed by the PMT and finally the LED flasher board, which is used for in-situ calibration purposes. An additional metal grid, more precisely a nickel-iron alloy, which wraps around the the PMT, shields it from earths magnetic field. Furthermore the whole pressure vessel is filled with dry nitrogen at a pressure about $\frac{1}{2}$-atmospheres [56]. The design goal of the IceCube DOM was to match requirements set by the experimental needs (e.g. low dark noise[1]) within the limits imposed by the infrastructure at the south pole (i.e. power consumption, reliability etc.) [1].

The IceCube Photomultiplier Tube

The PMT used in the IceCube DOM is the large-area Hamamatsu PMT R7081-02, which provides low noise rates, while maintaining large gains, as well as a good time and charge resolution [57] [58]. The purpose of a PMT is to measure small amounts of incoming light by turning it into an electronic signal, using several stages of amplification. The general structure is shown in figure 3.4.
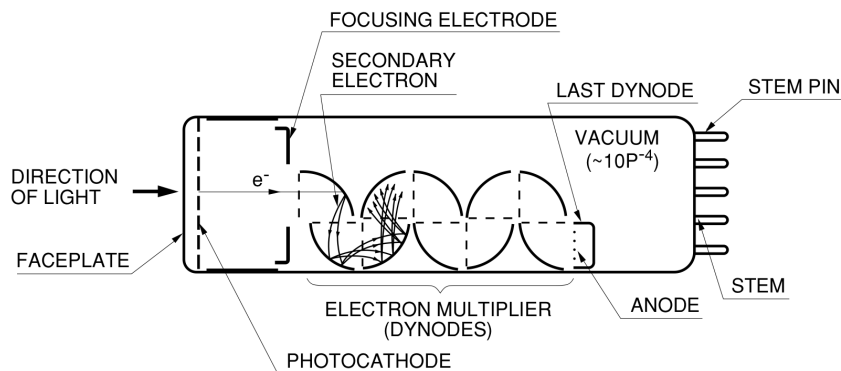
FIGURE 3.4: Light incident on the photocathode creates a small photocurrent (photo-electric effect) which gets amplified during several dynode stages (secondary emission) to finally produce a measurable signal at the anode (Figure from [59]).

Incoming photons hit the photocathode, which in case of the IceCube PMT is a bialkali photocathode (Sb-Rb-Cs and Sb-K-Cs) [1], leading to electromagnetic interactions between those photons and some electrons of the solid system of the photocathode, in which those electrons gain energy. If a single photon carries more energy than the energy at which a single electron is bound to the system (working function), the resulting

---

[1]dark noise denotes light signals seen by the PMT although no light source is present; the main contribution is thought to be due to radioactive processes in the glas sphere and/or the PMT

increase of the single electron's energy will allow the electron to leave its bound state. This is known as the photoelectric effect.

Typically the amount of emitted electrons is too small to provide a measurable photocurrent, hence this signal needs to be amplified. This is achieved in steps by several dynodes inside of the vacuum tube via secondary emission of electrons into the dynode chamber. Neglecting that the above mentioned processes are highly stochastic, giving rise to a non-trivial charge response of the PMT (cf. equation (3.4)), the physics of such a PMT can approximately be summarized as follows:

$$U_{PMT}(t) = RI(t) = R\frac{d}{dt}Q(t) \xrightarrow{\Delta t \to 0} R\frac{\Delta Q}{\Delta t}(t) \tag{3.1}$$

$$Q(t, \Delta t) = \gamma N_e(t, \Delta t)e \tag{3.2}$$

$$N_e(t, \Delta t) = \eta N_\gamma(t, \Delta t) \tag{3.3}$$

with R being the resistance of the resistor at which the current I induces the Voltage drop U. The total charge Q is collected after amplifying the number of emitted primary photoelectrons N_e by the overall dynode gain of γ. In IceCube a gain of $\gamma = 10^7$, is achieved (U=1, 3 kV). This was chosen to produce single photon pulses of 8 mV, in order not to conflict with the digitizer precision [58].

Quantum Efficiency
The IceCube PMT has its peak quantum efficiency of $\eta = 0.25$ at an incident photon wavelength of 390 nm [58], which lies at the lower end of the visible spectrum (blue), where Cherenkov radiation is most intensive.

Dark Noise
Another parameter of the PMT important for IceCube physics is the so-called dark noise rate. Even in the absence of any light source a PMT records light signals, which contribute to the background of any real incoming light. The typical dark noise rate of the IceCube PMTs has been estimated to be about 300 Hz at temperatures between $-20°$C and $-40°$C [58], which is the temperature range of the instrumented ice. An additional contribution to the dark noise comes from the glass sphere of the DOM. It is generally assumed, that radioactive decays (K^{40}, U, Th-contaminations in the glass [56]) in combination with scintillation are causing that noise [58].

Spectral Response of the PMT
The fraction between the number of photons, causing a PMT signal, and the number of photons incident to the DOM, defines the DOM acceptance η_{DOM}. It is a convolution of effects including transmission of photons through the DOM glass and gel, as well as the PMT quantum efficiency and collection efficiency. The DOM acceptance $\eta(\lambda)$ therefore

depends on the photon's wavelength, which is shown in Figure 3.5 (left). It peaks at a wavelength of 400 nm with η_{DOM} (400 nm) $\sim 13\%$.

Single Photo Electron (SPE) Charge Response

In order to be able to extract physics information out of the measured light yield, it is
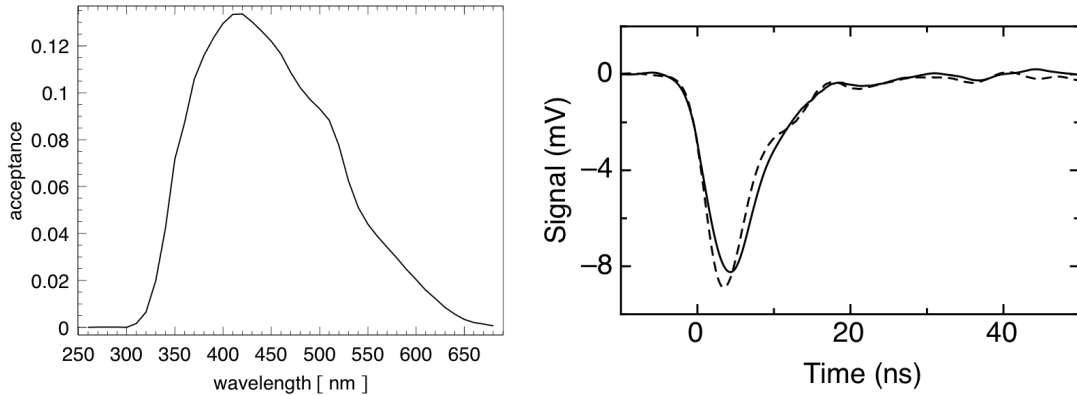
FIGURE 3.5: **Left:** The spectral dependence of the DOM's photon acceptance η is shown (from [60]); **Right:** The average of 10.000 SPE waveforms is shown. Single SPE waveforms were found to vary only in terms of absolute amplitudes, but the shapes agree at the 1%-level (Figure from [58]).

of crucial importance to understand the PMT response to single photoelectrons (SPE), since, due to the detector geometry, many DOMs will detect only small amounts of light during an event. This response was studied by using a dim UV LED (375 nm) with an average light output of 0.1 photons per shot [58]. It was shown that individually measured SPE waveforms differ w.r.t their amplitudes. The shapes were consistent at the few percent level. The average of several thousand SPE waveforms is shown in Figure 3.5 (right).

It was found that 90 % of the total SPE charge was detected within a 10 ns time window after the main peak in the waveform. That justifies to measure the distribution of the total charge of these SPE events as the charge seen within a 70 ns time window, which was triggered by the synchronization signal of the light source. The resulting distribution is shown in the left plot of Figure 3.6. It shows some characteristic features. At very low charges, slightly above 0 pC, one can see a sharp pedestal peak, which is an artifact of the digitizer, used to record the signal. Pedestal in that context refers to the signal measured by the digitizer, when there is no voltage drop present at the resistor (i.e. no signal in the PMT). At larger charges charges, a clear SPE peak q_0 is present. Its Gaussian contribution indicates a SPE resolution of nearly 30 % [61] [58]. However the intermediate region between the sharp pedestal peak and the Gaussian part of the SPE peak is given by an exponential decay of the measured charge. It was checked
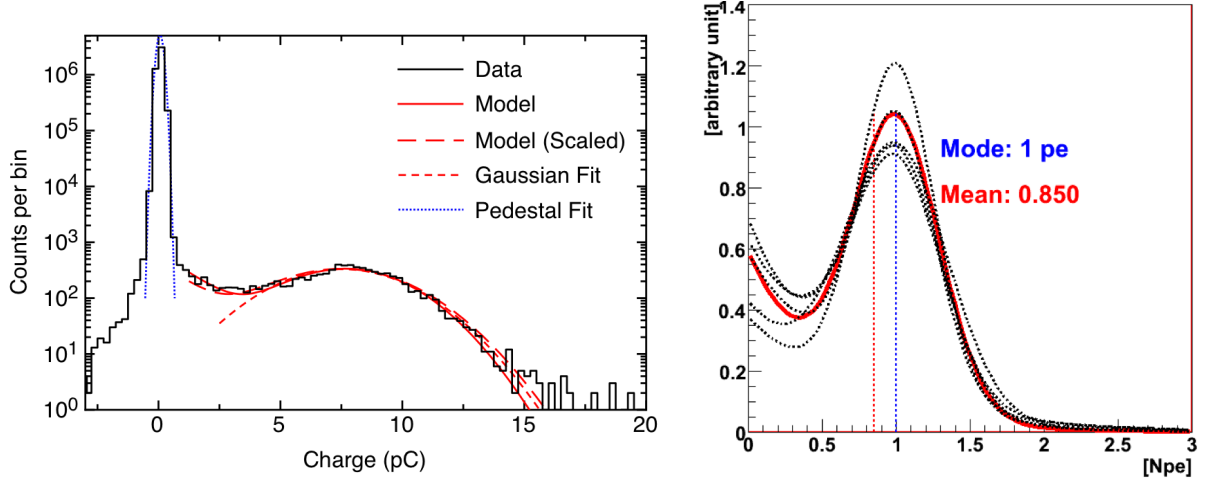
FIGURE 3.6: **left:** The plot shows the measured SPE charge response of an IceCube PMT. As expected a SPE peak (around 7pC) and a pedestal peak (close to 0pC) are visible (Figure from [58]). **right:** The plot show the SPE charge response function (3.4) of the IceCube PMT for different PMTs. In addition the average charge response function of a set of DOMs is shown (Figure from [61]).

by removing the light source (but keeping the synchronization trigger signal) that this exponential part is in fact a real contribution to the SPE signal [58]. It is assumed that this is mainly caused by back-scattering at the first dynode, which leads to a reduced amount of electrons entering the second stage. Omitting the pedestal dominated low-charge region ($q < 0.15 \, q_0$), the distribution was thus fit using an exponential and a Gaussian term [58]:

$$f\left(q\right) = \frac{P_e}{q_\tau} e^{-\frac{q}{q_\tau}} + \left(1 - P_e\right) \frac{1}{\sqrt{2\pi}\sigma_q} e^{-\frac{(q-q_0)^2}{2\sigma_q^2}} \tag{3.4}$$

with P_e being the fraction of counts in the exponential part, q_τ being a decay constant and σ_q being the width of the gaussian SPE-peak. q_0 describes the charge, at which the SPE part has its maximum.

The right plot of figure 3.6 shows the fits of the two terms in the charge response function (3.4) in the respective regions, as well as the global overall fit. The left plot of figure 3.6 shows the same charge response function in units of q_0 for some individual PMTs (dotted lines), as well as the average charge response (solid line). It was found that the mean expected SPE charge is 15 % smaller than the SPE peak charge q_0 ($q_{mean} = 0.85 \, q_0$) [61].

With a similar set-up it was possible to investigate the time resolution of the IceCube PMT, which for the vast majority of the events has been measured to be 2 ns. However a small amount of the events ($\sim 5\,\%$) showed so-called late hits with delays compared to the synchronization signal of up to 160 ns. These are again most likely caused by

backscattering at the first dynode. The delay time would then correspond to the distance traveled by the primary electron before it starts the pulse [58].

Saturation of the IceCube PMT

For highly energetic neutrino events (like Glashow Resonance cascades), which are among the most interesting for IceCube, additional effects have to be considered. At low energies, it is expected that the signal measured at the PMT output scales linearly with the brightness of the event [58]. However it is natural to assume that this scaling breaks down at very high energies. This effect is called saturation. It has been studied in [58] by illuminating the IceCube PMT with a LED, operated at different brightnesses. The
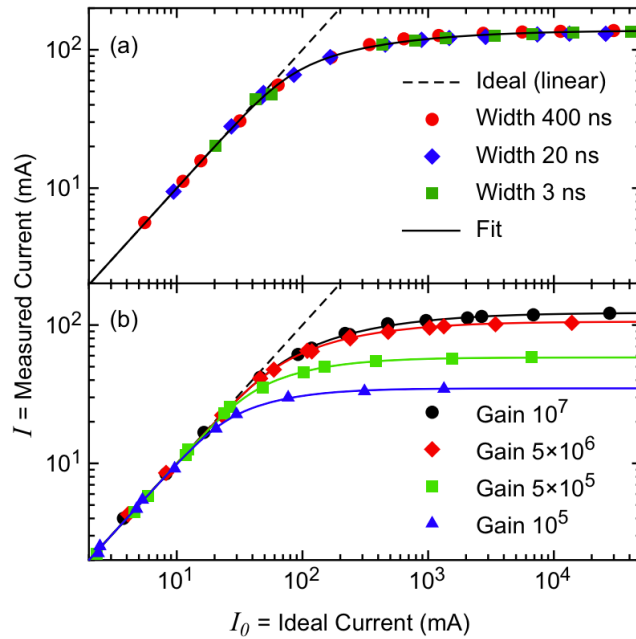
FIGURE 3.7: A comparison between the expected peak photocurrent I_0 given linear PMT response vs the actually observed photocurrent I. The LED pulse shape was varied as well as the PMT gain (Figure from [58]).

illumination level of the PMT was measured using an attenuation filter, which damped the light such, that the PMT was operating in the linear region. Then a set of different filters was used to slowly increase the light output. Based on the ratio between the attenuation coefficients of the filters, it was possible to determine the ideal peak photocurrent I_0, which would be expected, if the PMT would respond linearly over the whole range [58]. By comparing this ideal current to the measured Photocurrent I_{phot} at the PMT output, it was found, that the PMT response stays linear within 10% up to photocurrents of $I_{phot} = 50$ mA. This comparison is shown in figure 3.7 for different LED settings (various pulse widths) and different PMT settings (various gains). No peak photocurrent larger than 150 mA is visible. It was discussed whether the visible saturation is an effect of the charge collected in total, or whether it is an instantaneous effect of overly bright illumination. Since the saturation behavior was found to be independent of the

shape of the emitted light pulse, the instantaneous saturation interpretation is favored [58]. The saturation curve shown in figure 3.7 was parametrized as follows:

$$\ln I_0 = \ln I_{phot} + C \frac{(I_{phot}/A)^B}{(1 - I_{phot}/A)^{1/4}} \tag{3.5}$$

Unfortunately the parameters A,B,C used in this parametrization were found to vary strongly among the set of PMTs used in IceCube, which according to the authors, makes it unusable for reconstruction. Hence measurements of high energetic cascades have to rely on data of DOMs far away from the shower center. Although as of now it is not possible to extract meaningful information from the amplitudes of badly saturated DOMs, the photon arrival times can still help to constrain the region of the shower in the detector [58].

3.3 The IceCube Data Acquisition System

Data recording and digitization is controlled separately in each DOM by an FPGA (field-programmable gate array) chip on each DOM's mainboard. Only the digitized data is sent to the counting house on top of IceCube. This decentralized strategy was chosen in order to meet the required large dynamic range of each DOM, which is set by the large differences in signal strength [56]. This has the advantage that for one event at the same time those DOMs, which receive small amounts of light, are able to further amplify the PMT signal during recording, whereas those DOMs, which are close to the light source, can digitize at a lower gain to prevent the PMT signal to exceed the range of the digitizer. However in order to be able to later combine these individual data to one measurement, the time still needs to be defined globally. Thus the mainboard in each DOM receives timing information provided from a GPS-based Master Clock (synchronized to UTC standard) using the same cable network over which power is distributed. The design of the DOM mainboard is shown in Figure 3.8.

Light that enters the PMT, induces an electrical signal at the PMT output. This signal is then spread among the different mainboard components. First of all it is sent to a trigger, which is connected to the FPGA, which constitutes the mainboard logic. If this signal exceeds the trigger threshold, which is set to an equivalent of 0.25 spe, the FPGA starts the machinery needed to produce the data corresponding to this possible event. First of all the trigger information is transmitted to the LC (local coincidence) unit of the mainboard, which in turn is connected to the two vertically neighboring DOMs. This allows to introduce an LC-criterium, upon which the data recoding depends, which will be described later.

FIGURE 3.8: The figure shows the mainboard layout, used in the IceCube DOM. Its logic is controlled by the FPGA-chip starting the recording of the signal, once the charge trigger threshold of 0.25 *spe* gets exceeded. It also decides which digitization strategy (ATWD,fADC, see text) will be used according to the LC response of neighboring DOMs. (Figure from [56])

Another signal path connects the PMT output to the two ATWDs (Analog Transient Waveform Digitizer) where the signal arrives with a 75 ns delay. This delay is enough for the mainboard trigger to start ATWD recording, once the trigger threshold gets exceeded. At the ATWD the signal is split among the three possible ATWD input channels. At each of those ATWD inputs, the signal strength is controlled by an additional amplifier with amplifications of 0.25, 2, and 16 respectively. The ATWD also provides enough memory to store 128 samples (1 sample every 3.3 ns) of each of the three analog signal, taken at the input channels. This means that the ATWD is capable of covering a time window of 450 ns. Wether or not the stored sampling information is digitized depends on the LC feedback of the FPGA, since the digitization of the waveform at the ATWD precision of 10-bits takes 29 μs, which is a relatively large deadtime. This deadtime is the reason why the DOM mainboard provides a second ATWD chip, which can record an incoming signal, when the other ATWD digitizes an earlier waveform [56]. This strategy is called "ping-pong mode".

In addition to the ATWDs, the PMT output signal is sent to the FADC chip (Fast Analog to Digital Converter). The FADC, which only has one channel at a fixed amplification (x23.5) covers a time window of 6,4 μs in order to record signals which exceed the ATWD window. The smaller sampling rate of the FADC (25 ns per sample, 256 samples in total) allows is to digitize signals without deadtime.

As mentioned above, the ATWD digitization of the recorded waveform depends on local

FIGURE 3.9: **upper plot:** The plot shows two ATWD waveforms recorded by the two different ATWD chips. Since the strong signal exceeded 768 ATWD counts for the mid- and high gain channels, the lowest gain channel (blue) is shown. Due to the deadtime of the first ATWD after digitization, the second ATWD records the late part of the signal at the highest gain (red). **lower plot:** The fADC waveforms corresponding to the same signals shown above. The first fADC waveform (blue) exceeds the dynamic range of the digitizer.

coincidence (LC). Given that the trigger thresholds of the neighboring DOMs on the same string have been exceeded within a time window of $\pm 1\,\mu$s, the signal gets flagged as LC, which leads to ATWD digitization. The ATWD waveform, which was recorded at the highest gain (x16), is digitized first. If at some point the digitized signal of that channel exceeded the equivalent of 768 ATWD counts, the second channel is digitized as well. The same condition may trigger the digitization of the lowest gain channel. This strategy was chosen in order to provide at least one waveform which does not suffer from ATWD clipping, while saving space by not digitizing redundant information [56]. During analysis all available waveforms will be combined (up to three ATWD channels + one FADC channel).

However, if the signal did not meet the LC criterium, then only the FADC digitizes the waveform. This is justified since isolated hits (SLC) compared to HLC hits (with LC flag), are by far more likely to be PMT induced noise, than to be physics related information. An example of the digitized waveform of a very bright cascade ($\sim 1\,$PeV)

measured in a single DOM, is shown in figure 3.9 and clearly exhibits the different digitization features described above.

The technical design of the IceCube allows for two main event topologies, which form the basis of lepton flavor discrimination in IceCube. Electrons propagating through the glacial ice experience rapid energy loss (compare section 2) thus forming an electromagnetic cascade, which due to photon scattering in the ice is characterized by an almost spherical light distribution. Such a cascade with an energy about 1 PeV is shown at the top of figure 3.10. Since for contained cascades, all primary neutrino energy gets deposited in the detector, this channel has the best energy resolution, but provides a worse pointing accuracy [50] compared to the other main signature, the muon track. The cascade channel is typically used in searches for diffuse fluxes of astrophysical neutrinos. The signature left by a muon inside of IceCube differs significantly from those cascades. Since the muon is around 200 times heavier than an electron, it radiates less energy, leading to a larger propagation length (several kilometers at PeV energies). Hence they appear as tracks in the detector, as shown in the middle picture of Figure 3.10 for a simulated PeV event. Due to their long range this channel provides an excellent directional resolution (less than 1 degree) and an enhanced effective area. Therefore this is the channel, used to look for point sources of neutrinos in the sky.
A very unique signature arises from the rare Glashow resonance muon channel. Since this interaction does not involve a hadronic component, the final state muon will not be accompanied by a cascade, thus showing a starting track at the bottom of figure 3.10 (simulated). However the most "creative" particle in this context is the tau particle, which produces a variety of different signatures with a double bang (hadronic components of tau creation and decay) being expected at PeV energies. As for now neither tau related signatures nor the Glashow resonance have been found.

3.4 Artifical Light Sources in IceCube: Flashers and Standard Candles

For an experiment like IceCube it is very important to understand the detector response to an incoming signal, in order to properly simulate and reconstruct those events. Since the IceCube is a detector for natural sources of neutrinos, it does not include an accelerator machine to create a particle beam, that could be used for calibration. Hence studying the detector response including measuring the optical properties of the arctic ice has to rely on different methods. The main tools used for this purpose are the flasher boards in each DOM and the two lasers, which have been deployed.

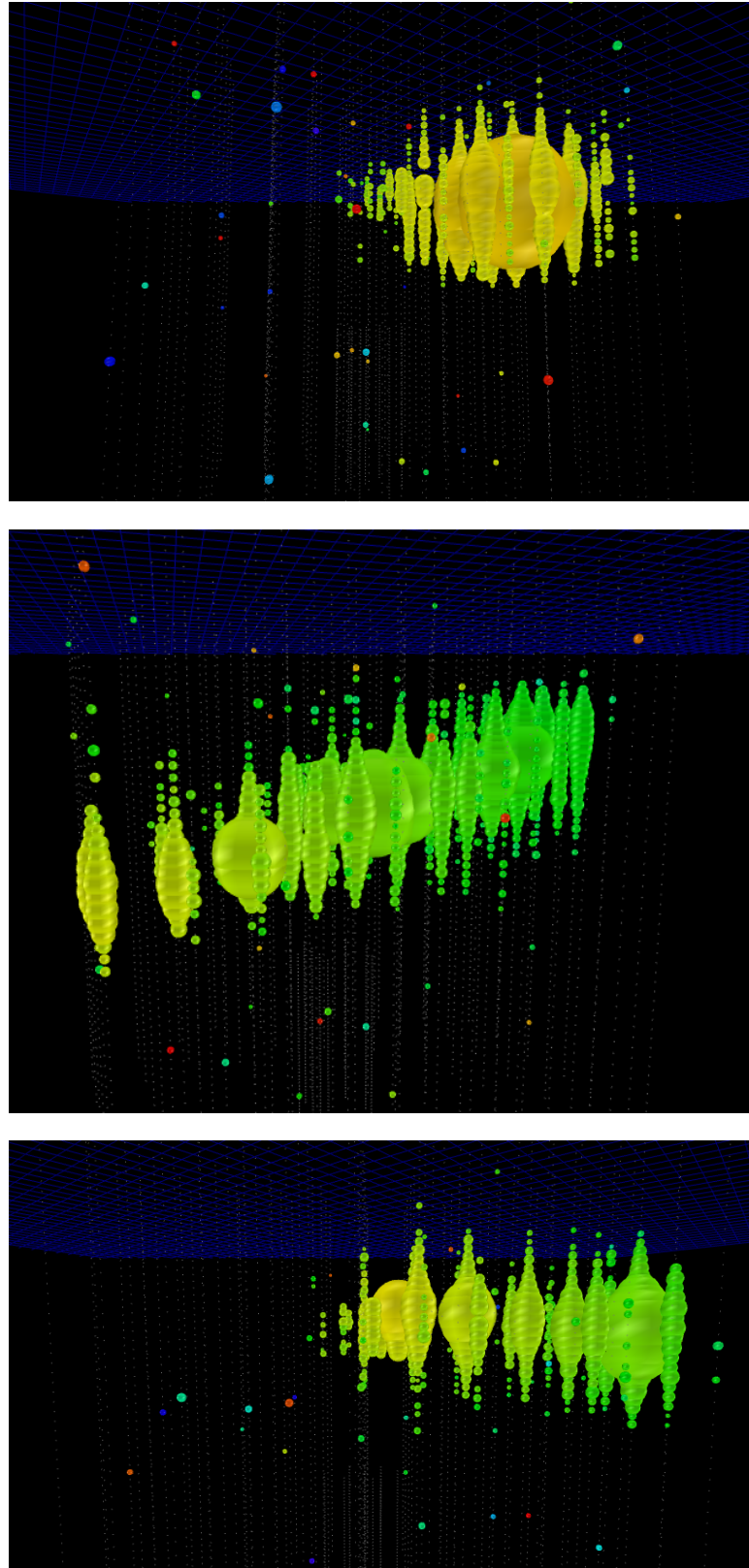FIGURE 3.10: **top:**A PeV neutrino induced cascade event is shown (data). This event topology is beneficial in diffuse searches. **center:** A PeV neutrino induced through going track is visible (simulation). Such events are used in searches for point sources of neutrinos. **bottom:** A muon produced in a Glashow Resonance interaction will miss the hadronic cascade at its vertex, hence producing a starting track

The Flashers

Each IceCube DOM is equipped with a flasher board, which holds 12 LEDs. They can emit light pulses at a wavelength of $\lambda = 405$ nm. Half of the LEDs are oriented horizontally with an azimuthal spacing of $60°$. The other half uses the same azimuthal spacing but is tilted upwards by $40°$. The light output of the LEDs can be varied in terms of pulse width and brightness, with a maximum light output per LED of 8×10^9 photons which mimics a 80 TeV cascade. Calibration based on Flashers therefore aims at the TeV energy regime. For the purpose of this thesis however the in-situ calibration needs to address higher energies in the PeV range. Hence it can not rely on Flasher data.

The Standard Candles

A more powerful light source is given by the two standard-candle lasers SC1 and SC2 which have been deployed at depths of 1811 m (on string 40, pointing upwards) and 2153 m (on string 55, pointing downwards) respectively. The nitrogen laser Lastertechnik-Berlin MNL-100 produces pulses with a width of 4 ns at a near-UV wavelength of 337 nm. Per pulse, a maximum energy of $120\,\mu$J is released [62]. A custom filter wheel allows to regulate the intensity from 0.5% to 100% in steps of 0.5%. By using a highly reflective cone, the beam is shaped according to the Cherenkov angle, thus mimicking point-like Cherenkov emission. The effect of the beam shaping is shown in Figure 7.1. For the pur-
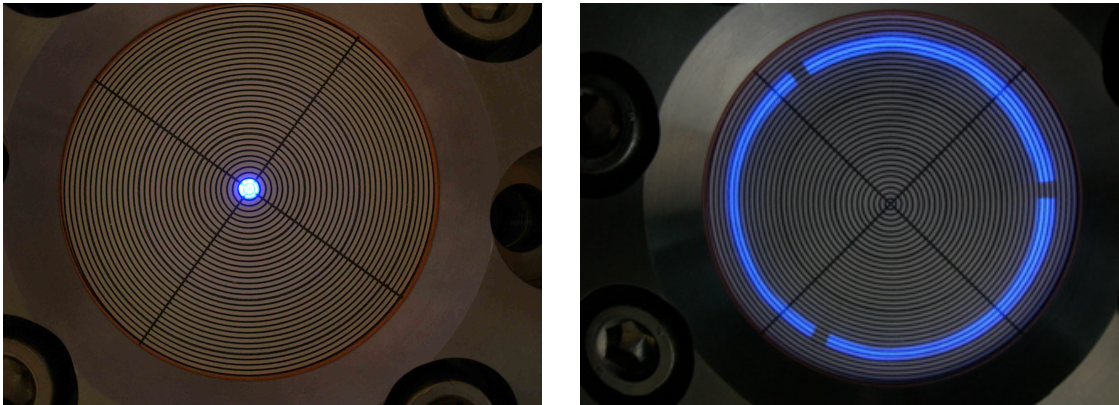
FIGURE 3.11: The effect of the beam shaping of the SC: before using the reflective cone, i.e. no shaping (left) and after (right).

pose of IceCube two properties are important. First, the number of photons released in different pulses should be stable (pulse-to-pulse stability). During calibration measurements of the standard-candle in the laboratory, a pulse-to-pulse stability better than 3% for temperatures between room temperature and $-25°$C has been found in agreement with the manufacturer's specification [62]. Secondly the absolute output needs to be known very well, in order to use the Standard Candle in-situ as a calibration device to gauge cascade reconstruction algorithms, especially targeting the absolute energy scale.

Nominal	0.5%	1%	3%	10%	30.5%	51%	100%
SC1	0.9%	1.39%	3.5%	10.9%	32.2%	53.9%	100%
SC2	0.07%	1.4%	2.92%	8.4%	26%	37.2%	100%

TABLE 3.1: Lab calibrated filter attenuations of SC1 and of SC2 (preliminary)

In that context, by measuring the rations between the filter wheel settings E_s and a reference setting E_r for 10,000 pulses, it was found that the actual attenuation by those filters deviate from the manufactures specifications. The effective intensity of the laser and filter wheel combination was found to scale according to a factor of 110 within the nominal range 0.5% to 100% (for SC1). The measured effective attenuations by the different filter wheel settings for both lasers are given in table 3.1. For SC1 the total number of emitted photons at 100% brightness is known to within 10% (stat.). However large unresolved systematics exist [62]. For SCII the preliminary maximum intensity corresponds to 2.5×10^{13} photons. Hence the SCII output covers a range from $\sim 10^{11}$ to $\sim 10^{13}$ photons, which should approximately be $1\,\mathrm{PeV}$ to $100\,\mathrm{PeV}$ cascade energy equivalent.

3.5 The IceCube Data Processing Chain

Since data transmission resources are limited and the vast majority of the incoming data consists of background (cosmic ray muons), it is neither necessary nor feasible to sent all data to the analyzers in the north. In this section we summarize the steps involved in reducing the data stream.

Triggering and Filtering

After a signal is digitized, a decision has to be made whether or not that signal is interesting enough to be stored on disk. This decision depends on a set of selection criteria (triggers). One example is the so-called Simple Multiplicity Trigger (SMT). In IceCube SMT8 is required, so this trigger keeps events, that produced light in at least 8 optical modules during a time window of $5\,\mu s$. In addition, those eight DOMs have to satisfy local coincidence. The overall trigger rate (SMT8 and others) in IceCube amounts to about $\sim 2700\,\mathrm{Hz}$, which implies a data rate of almost $1\,\mathrm{TB/day}$. However the satellite bandwidth available, to be used by IceCube, is limited at $\sim 100\,\mathrm{GB/day}$ [63]. Hence different so-called "Online Filters" have been designed, which choose the most interesting events (among the set of triggered events) to be sent north via satellite. The decisions made by those filters, are based on the results of fast reconstruction algorithms, which

are used at the pole. If an event did not pass those filters, it gets stored on tapes, which are shipped north once a year. The most important online filters are the Cascade Filter, designed to select events with a cascade like light pattern, the Muon Filter, which selects events with a track like signature and the EHE filter, which keeps events with a high multiplicity (bright events). For the purpose of this thesis the Cascade Filter is of interest. For neutrinos with energies above $10\,\text{TeV}$ the Online Cascade Filter (2012) achieves a signal efficiency of $\sim 90\%$, while removing $\sim 99\%$ of background. Once the data arrived at the computing center in the north, further so-called offline processing is applied. The first step is named offline Level2. No filtering in addition to the online filter is applied, but further reconstructions are performed. Based on those results additional filtering is done at Level3, to further remove background events, thus reducing the amount of data. At Level3 of the Cascade Filter stream, the most sophisticated and computationally intensive reconstruction methods are applied, which will be discussed in this thesis. For cascade-like events, contained in the detector, the Level3 filtering is almost 100% signal efficient compared to Level2.

Calibration and Pulse Extraction

As already described, the data consists of ATWD waveforms at different amplifications as well as one fADC waveform. Before being ready for reconstruction, the data needs to be processed in order to account for effects caused by the DOM electronics. Furthermore light pulses have to be extracted from the calibrated waveforms, which are the input to reconstruction methods.

Throughout the work of this thesis, whenever raw data needed to be calibrated, the **WaveCalibrator** module was used. Before the ADC counts in each bin of the different waveforms can be converted into a voltage, the contribution due to digitizer pedestal need to be subtracted (compare figure 3.6). The baseline contribution in each DOM was measured using so-called beacon launches, which means that the waveform recording and digitizing procedure was triggered by the CPU of the FPGA on the DOM mainboard. Since the so recorded waveforms typically due not contain pulses induced by real light, they can be used to determine the pedestal baseline (digitizer response to zero input charge). The average of these beacon waveforms is the beacon-baseline to be subtracted by the WaveCalibrator. In a next step the start time of all waveforms are corrected for the PMT transit time and the delay times between the different digitizer channels. In addition all waveforms need to be corrected for possible distortions due the transformer between the PMT and the High Voltage control board in the DOM.

For reconstruction purposes it is important to know the arrival times of the light pulses incident on the PMT during an event. However due to the PMT charge response to

single photons the pulse timing information get smeared. If multiple photons (a pulse) hit the PMT, the final signal will be a superposition of those single photo-electron signals. Hence the calibrated waveforms represent a convolution of a light pulse with the detector response to single photons. In order to reconstruct the charge and timing information of incident light pulses, one needs to find the photon distributions in each time bin of the corresponding waveform, which when convoluted with the spe charge response, would give rise to the observed waveform. Several algorithms exist which are able to unfold light pulses from the calibrated waveforms. These pulses are then characterized by their charge (number of photons), their starting time and width of the respective pulse. For the purpose of this thesis, if pulses needed to be extracted the tool **WaveDeform** was used. It is able to deconvolve the above described processes by using a linear algebra based non-negative least squares algorithm. ATWD and fADC signals are processed simultaneously. The output of this module gets stored in the frame as so-called OfflinePulses, which contain all recorded light pulses (HLC and SLC). For some algorithms it is beneficial to remove background contributions (i.e. noise). One example is the so called time window cleaning, which only keeps the light pulses within a $6\,\mu s$ time window around the largest fraction of hits. If in addition the pulses are required to satisfy local coincidence, the result is called TWOfflinePulsesHLC.

Chapter 4

The IceCube Simulation Framework

In experimental physics dedicated simulations are needed, in order to not only predict the detector response for a single event but also to determine the signal distributions for an ensemble of events of a given physics hypothesis. Those predictions are necessary to relate the observables, extracted from the data, to the underlying physics quantities of interest. Within the IceCube Collaboration the software IceSim provides the available simulation tools. They allow to produce simulated data from a given flux of neutrinos, handling the details like neutrino propagation through the earth, lepton production and propagation in the detector, light emission and tracking and finally the light induced detector response.

4.1 Neutrino Generator

In the energy range of interest for this thesis, the processes related to neutrino propagation from primary neutrino injection at earth's surface to primary lepton production in the vicinity of the detector are simulated using the neutrino-generator [64]. It creates neutrinos according to a neutrino flux at Earth's surface following a power law with spectral index γ. These neutrinos are subsequently injected into the earth and then propagated, in order to determine the corresponding neutrino flux at the surface of the detection volume, while accounting for the interactions the neutrino might face. With the tau neutrino being an exception, a charge current interaction between a neutrino and a nucleon somewhere in the earth leads to the absorption of the corresponding neutrino and hence that particular neutrino does not contribute to the flux at the detector surface. In contrast the tau neutrino is "regenerated", when the secondary tau lepton decays,

thus producing a tau neutrino. Neutrinos of all flavors are subject to neutral current interactions, in which the neutrino looses energy. If a neutrino finally reaches the detection volume and eventually produces detectable charged leptons, it adds to the number of detectable neutrino events $N_{detection}^{MC}(E_\nu)$. Hence neutrino-generator allows to determine the expected event rate $R = J_\nu(E_\nu) \cdot A_\nu^{eff}(E_\nu)$ with $A_\nu^{eff}(E_\nu) = \frac{N_{detection}^{MC}(E_\nu)}{N_{injected}^{MC}(E_\nu)} A_0$ being the neutrino effective area of the detector, while A_0 denotes the geometric area [64].

In order to accumulate sufficient Monte Carlo statistics an event weighting technique is applied. That means that neutrino generator forces every neutrino, which reaches the surface of a cylindrical volume, fully containing the detector, to interact. The interaction point along the trajectory (parametrized with x) inside that cylinder of length L is randomly chosen with probability $p(x) = \frac{1}{L}$. Since this is an unphysical choice, the event has subsequently to be weighted according to the true interaction probability $P_{int}(x) = N_A\rho\sigma_{tot}(E_\nu)e^{-N_A\rho\sigma_{tot}(E_\nu)x}$. Hence the weighting factor is:

$$W_{int}(x, E_\nu) = \frac{N_A\rho\sigma_{tot}(E_\nu)e^{-N_A\rho\sigma_{tot}(E_\nu)x}}{1/L} \tag{4.1}$$

with $N_A\rho$ being the number density of target nucleons in the detector material and $\sigma(E_\nu)$ being the total νN cross section. The cross-sections used in neutrino generator are provided by the CTEQ Collaboration (CTEQ5, see sec. 1.3). In addition it is possible to save computing resources by oversampling events with high energies (i.e. by using a hard injection spectrum), which subsequently need to be reweighed to a physical flux $\frac{d\Phi_\nu(E_\nu)}{dE_\nu}$. The overall weighting information is stored as OneWeight variable and reads:

$$\text{OneWeight} = \left(\frac{P_{int}^{tot}}{E^{-\gamma}}\right)\int_{E_{min}}^{E_{max}} E^{-\gamma}dE \cdot A_0 \cdot \Omega \cdot T \tag{4.2}$$

with P_{int}^{tot} being the combined probabilities of the neutrino propagation and interaction, as described above. Ω and T denote the solid angle and collection time respectively. Using OneWeight, the weighting factor for a single event i based on the neutrino flux of interest $\frac{d\Phi_\nu(E_\nu)}{dE_\nu}$ can be expressed as:

$$w_i = \frac{OneWeight_i}{NEvents} \cdot \frac{d\Phi_\nu(E_\nu)}{dE_\nu} \tag{4.3}$$

with NEvents being the total number of injected neutrinos.

4.2 Muon and Cascade Monte Carlo (MMC and CMC)

In a second step the charged leptons produced in the detection volume have to be propagated in order to determine their light yield. In case of muons and taus this is done using the Muon Monte Carlo (MMC [65]), which simulates the stochastic energy losses due to ionization, bremsstrahlung, photo-nuclear interactions and electron pair production based on the respective cross sections. Since the number of stochastic energy losses diverges with $\frac{1}{E_{lost}}$, a lower bound e_{cut} on the energy is introduced. Below that threshold the total energy loss is treated continuously [65].

In this thesis the secondaries of interest are electrons and hadrons, which produce electromagnetic and hadronic showers. The light yield of these cascades is calculated using the tool Cascade Monte Carlo. When the secondary particle, responsible for the subsequent shower, is created by neutrino-generator, that particle is assumed to be point like. However with increasing energy the spatial extension of a cascade becomes important. The basic idea behind CMC is to account for the longitudinal elongation of a cascade by splitting the "point like" primary cascade into several sub cascades according to its energy loss profile in the longitudinal direction. Below energies of $1\,\mathrm{PeV}$ the energy loss of the respective electromagnetic shower is based on parametrization eq. (2.14). This is visualized in Figure 4.1 for a shower with $E = 100\,\mathrm{TeV}$.

Above $1\,\mathrm{PeV}$ the longitudinal shower development is simulated based on the pair production and bremsstrahlungs cross-sections, with the suppression due to the LPM effect[1] being taken into account. Particles are tracked in one dimension until their energy falls below a given energy, typically $1\,\mathrm{TeV}$. The energy loss profile of the full shower is than given by the sum of the profiles of the individual particles. It should be mentioned, that due to the infrared divergence of the differential bremsstrahlungs cross section, the total cross section used, only considers radiation of photons with energies larger than $1\,\mathrm{GeV}$. In section 2 it was discussed that the average light yield of a hadronic cascades scales with the light yield of their electromagnetic counterparts. The same scaling is used in CMC to derive the energy loss profile of hadronic cascades. However due to their stochastic nature, the scaling factor is sampled from a Gaussian distribution around the mean light yield. In addition hadronic cascades may contain low energetic muons. The amount of produced muons in a given hadronic cascades relies on a parametrization derived from Corsika [66] simulations.

---

[1]The LPM effect denotes a strong decrease of the Bremsstrahlungs cross-section due to quantum interference between the scattering amplitudes of different atoms. Since this effect is only important above $E_e \approx 10\,\mathrm{PeV}$ it has no influence for the purpose of this thesis.
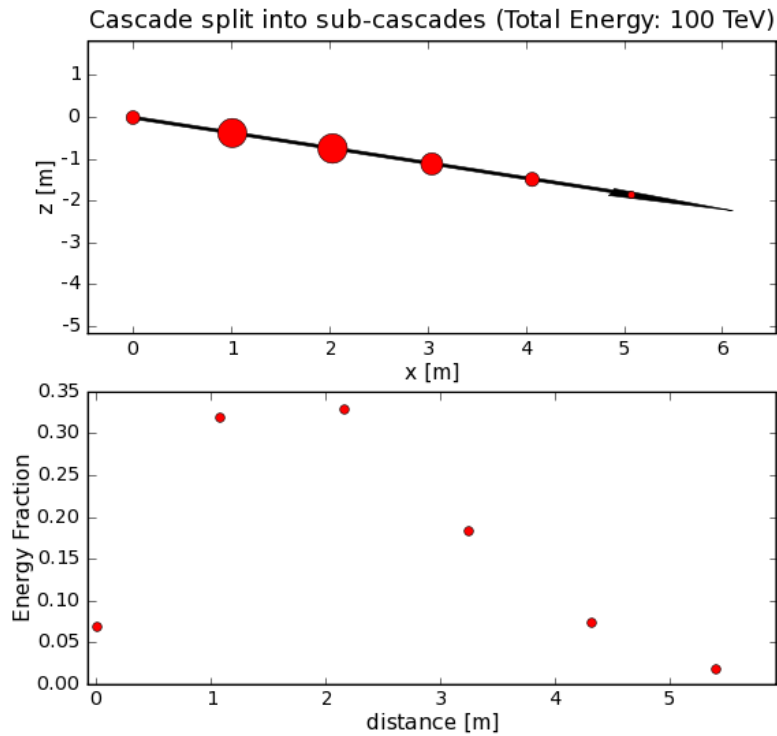
FIGURE 4.1: A Cascade with energy $E = 100\,\text{TeV}$ is split by CMC into sub cascades (top) according to its longitudinal energy loss (bottom)

4.3 Modeling the optical properties of arctic Ice

Understanding the optical properties of the glacial ice, scattering and absorption lengths of photons, at the south pole is a necessity for simulation and reconstruction of events in IceCube. Glacial ice is the most transparent known solid for light in the blue and near UV regime $\sim (200\,\text{nm} - 400\,\text{nm})$. It is also an inhomogenous medium [67]. First of all, the scattering of light in the shallow ice above depths of $1500\,\text{m}$ is primarily dominated by the presence of air bubbles, leading to short scattering lengths. Due to the pressure gradient present in the ice their density depends on the depth. With increasing depth, those air bubbles slowly transform into air-hydrate crystals until at depths of $1500\,\text{m}$ and larger, no air bubbles remain. Since those crystals share their refractive index with the surrounding ice, they can be transversed by a photon almost without scattering [67]. Secondly, since a glacier slowly forms when existing snow gets compressed to ice under the pressure of new snow, climate changes in the past left imprints to the ice in form of its dust and ash contamination. Hence below $1500\,\text{m}$ the optical properties of the ice are determined by the depth dependent concentration of those dust particles. The most recent description of the optical properties of the ice in IceCube is given by the south pole ice model (SPICE) [68]. By using the flasher LEDs of the 60 DOMs on String 63 as

a light source and the DOMs on the strings surrounding string 63 as light sensors, the effective scattering coefficient b_e and the absorption coefficient a_{dust} have been extracted for depths between $1400\,\mathrm{m}$ and $2500\,\mathrm{m}$ in steps of $10\,\mathrm{m}$ [2]. Although the emission of the flasher LED peaks at $405\,\mathrm{nm}$, the light emitted by the DOM peaks at $400\,\mathrm{nm}$ due the influence of the pressure vessel. Hence the wavelength dependent coefficients have been extracted at $400\,nm$. However parametrizations exist, which allow to extrapolate those coefficients to other wavelengths [67].

In order to determine the parameters b_e, a_{dust} at $400\,nm$, the response of the receiving DOMs to the flashing string 63 has been simulated based on the direct photon propagation code PPC [69] for many different sets of scattering and absorption coefficients. PPC propagates photons from their source until they reach a DOM or are absorbed in the ice based on a linear combination of the Heney-Greenstein function (HG) and the simplified Liu scattering function (SL), describing the distribution of the scattering angle θ of a photon [68]:

$$p\left(\cos\theta\right) = (1 - f_{SL}) \cdot HG\left(\cos\theta\right) + f_{SL} \cdot SL\left(\cos\theta\right) \tag{4.4}$$

with f_{SL} being a constant, which was varied as well, in order to find the best fitting value. The HG and SL scattering functions read:

$$HG\left(\cos\theta\right) = \frac{1}{2}\frac{1 - g^2}{\left(1 + g^2 - 2g\cos\theta\right)^{\frac{3}{2}}} \tag{4.5}$$

$$SL\left(\cos\theta\right) = \frac{1 + \alpha}{2} \cdot \left(\frac{1 + \cos\theta}{2}\right)^{\alpha} \tag{4.6}$$

with $\alpha = \frac{2g}{1-g}$ and the mean scattering angle $g = \langle\cos\theta\rangle$. The PPC result provides an estimate of the total cumulative charge $s_{oo'}$ expected in DOM o for n_s flasher events from DOM o'. At the same time from the flasher data the corresponding measured charge $d_{oo'}$ for n_d flasher events is known. This allows to construct the following Likelihood [68]:

$$L = \prod_{o,o'} \frac{\left(\mu_s^{oo'} n_s\right)^{s_{oo'}}}{s_{oo'}!} e^{-\mu_s^{oo'}} \cdot \frac{\left(\mu_d^{oo'} n_d\right)^{d_{oo'}}}{d_{oo'}!} e^{-\mu_d^{oo'}} \cdot \frac{1}{\sqrt{2\pi\sigma^2}} e^{-\frac{\left(\ln\mu_d^{oo'} - \ln\mu_s^{oo'}\right)^2}{2\sigma^2}} \tag{4.7}$$

This Likelihood is minimized w.r.t. the per-event expected charge $\mu_s^{oo'}$ and the per-event measured charge $\mu_d^{oo'}$. The gaussian term accounts for the possible error of describing data with simulation. Once the best fit values for μ_d and μ_s are obtained for each simulated set (which differ w.r.t. of the assumed scattering and absorption coefficients), a final χ^2 fit selects the simulated set of coefficient with the best agreement between

---

[2]For more details about scattering and absorption coefficients, see sec. 4.4.

data μ_d and simulation μ_s:

$$\chi^2 = \sum_{oo'} \frac{\ln \mu_d^{oo'} - \ln_s^{oo'}}{\sigma^2} + R \tag{4.8}$$

where R denotes regularization terms, which have been introduced to suppress bias due to fluctuations (more details in [68]). The fit result yielded the SPICE1 ice model. In order the improve the result, a second iteration of the fitting procedure also included data obtained from the dust logger [70], a device, which was lowered into the IceCube boreholes to measure scattering by dust. In the regions above and below the instrumented region of IceCube, the dust logger data added useful information to the fitting routine. The final fit result is known as the SpiceMie ice model and is shown in figure 4.2. The effective scattering and absorption coefficients are compared to the AHA ice model [67], which is based on AMANDA[3] measurements and was previously used. The so called dust layer, a region with a high concentration of dust particles between $\sim 2000\,\mathrm{m}$ and $\sim 2100\,\mathrm{m}$, shows up as a strong peak in the scattering and absorption coefficients. It was formed during the last glacial period about $65,000$ years ago.
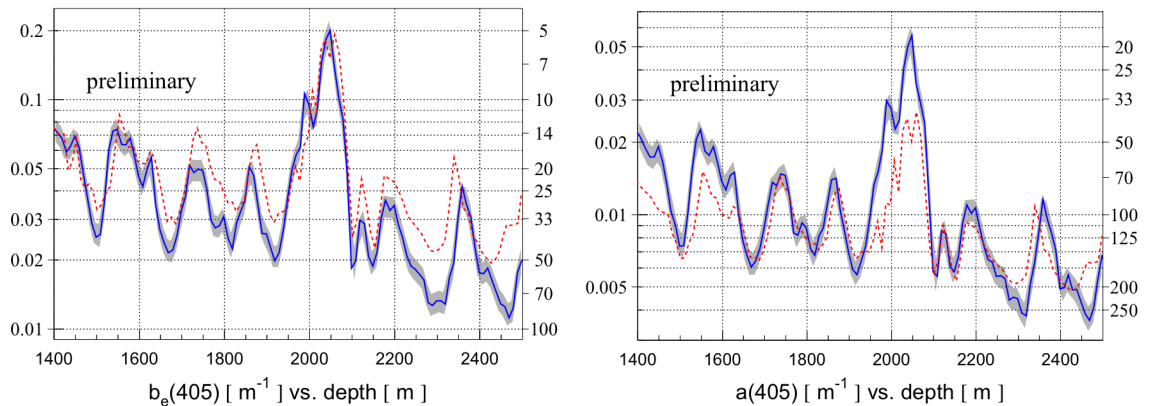
FIGURE 4.2: Depth dependence of the effective scattering coefficient b_e (left) and the absorption coefficient a (right) according to the SPICE Mie and AHA ice models. Values given for a photon wavelength of $\lambda = 405\,\mathrm{nm}$; Figure from [68]

4.4 The Photonics Simulation

The IceCube neutrino detection is based on detecting Cherencov photons. Hence it is of crucial importance to know the arrival time distributions as well as the total amount of expected photons at all DOM positions corresponding to a specific light source for both, event simulation and event reconstruction. Since photon propagation is a highly

---

[3]AMANDA was the predecessor of IceCube and was located at smaller depths between $1500\,\mathrm{m}$ and $1900\,\mathrm{m}$

stochastic process, these distributions can not be calculated analytically and have to be extracted from simulations, targeting photon propagation. In IceCube the Photonics [71] software is used. The optical properties of the inhomogenous glacial ice, which determine the scattering and absorption of the propagated photons are described by five parameters, which depend on the photon wavelength and the depth in the ice (assumed to possess azimuthal symmetry): $(n_g, n_p, \langle \cos\theta \rangle, \lambda_e, \lambda_a)$. The first two parameters are the group refractive index n_g, determining the velocity of the photons, and the phase refractive index n_p, describing the respective transmission and scattering coefficients of the ice. Absorption due to atomic and molecular excitation is modeled by the absorption length λ_a. The effective scattering length λ_e denotes the distance, which the light travels before the photon directions are completely randomized [71]. The latter is determined by two effects: the scattering length λ_s, the length scale defining the distance between two scatterings, and the angular distribution of the deflection at each scattering. The scattering centers in the ice (air bubbles, dust particles etc.) are assumed to have a spherical shape and hence the angular distributions used in Photonics are based on the Mie solution to the Maxwell equations in the limit of forward peaked scattering. Thus they are given by the Henyey-Greenstein distribution eq. (4.5), determined by $\langle \cos\theta \rangle$. With those parameters the Photonics simulation is able to track the propagation of each photon from its source to a given volume element dV. This propagation is described using a cylindrical coordinate system, which is aligned with the principal axis of the source, as shown in Figure 4.3. Due to the azimuthal symmetry of the ice only two coordinates are needed to describe the source: the tilt of the principal axis of the source $\pi - \Theta_s$ and its depth Z_s. Once the principal axis of the source is chosen, the cylindrical coordinate system used to describe the volume elements $dV(\rho, l, \Phi)$ is fixed. Here l denotes the distance of that element along that principal axis, whereas ρ and ϕ describe its position in the plane perpendicular to $\hat{l}$ at a given distance l, with $\Phi = 0$ defined such, that $\hat{\rho}$ is maximally aligned with $\hat{z}$ [71]. The distance between source and receiver dV is denoted as d. To determine the delay time distributions $\frac{dp}{dt}(Z_s, \Theta_s, \rho, l, \Phi, t_d)$ with $t_d = t - \frac{d}{c_{ice}}$ and the corresponding time integrated photon flux $I(Z_s, \Theta_s, \rho, l, \Phi, t_d)$, a given number of photon is injected at the source position following the cherenkov spectrum and angular distribution. Each photon is then propagated through the ice, with the length between two scatters and the survival probability being sampled from the corresponding exponential distributions characterized by the scattering coefficient λ_s and the absorption coefficient λ_a respectively. During that procedure the depth and wavelength dependence of those parameters is taken into account. Since photon fluxes are linear, a moving light source can be simulated as superposition of single source. F cascade like emission only stationary sources are considered. The results of simulating single sources are stored in large tables which are binned in the dimensions ρ, l, Φ, t_d. Due to the azimuthal symmetry of the ice it is sufficient to simulate Φ in the range of
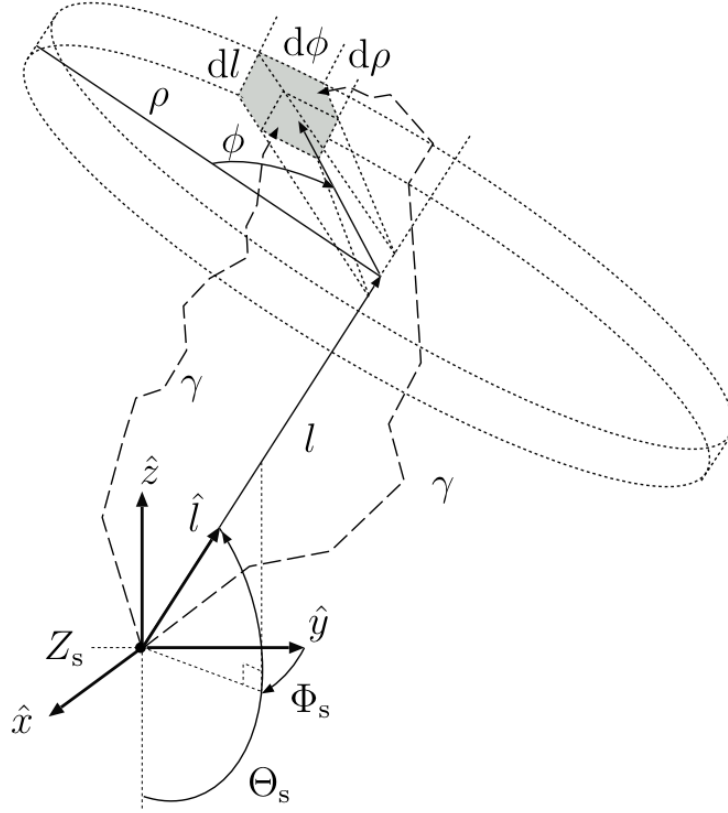
FIGURE 4.3: The coordinate system used in Photonics to simulate photon propagation from a source with principal axis $\hat{l}$ to a given volume element $dV = \rho \, d\rho d\phi dl$; Figure from [71]

$[0°, 180°]$, while still accounting for the depth dependence of the ice properties. For each source (Z_s, Θ_s) such a table is created and itself stored in a table of such sources. The tables, used in this thesis, are binned as follows: $\Delta Z_s = 10 \, \mathrm{m}$ and $\Delta \Theta_s = 20°$.

By construction the Photonics tables do not contain information about the dependence of the tabulated data on the cascade energy E_0. However since the stochastics of the photon propagation is independent of the source energy E_0, the arrival time distributions $\frac{dp}{dt} (Z_s, \Theta_s, \rho, l, \Phi, t_d)$ do not depend on energy. Only its normalization, the time integrated photon flux $I (Z_s, \Theta_s, \rho, l, \Phi, t_d)$, does. It was shown in section 2.2, that the light yield of a particle shower is approximately directly proportional the shower energy. This relation can be used to determine the total number of photoelectrons $\langle \mu_{tot} \rangle$ from the time integrated photon flux $I (Z_s, \Theta_s, \rho, l, \Phi, t_d)$, based on the photo effective area and the quantum efficiency of the IceCube DOMs [50]. Photonics results are based on a simulated source with a strength corresponding to $E_0 = 1 \, \mathrm{GeV}$ [47]. Hence the number

of photoelectrons $\langle\mu_{tot}\rangle_o$ in DOM o for arbitrary energies E_0 reads:

$$\langle\mu_{tot}\rangle_o = \langle\mu_{tot}\rangle_o^{1\,GeV}\ \frac{E_0}{1\,GeV} \tag{4.9}$$

$$\langle\mu_{tot}\rangle_o^{1\,GeV} = (1\,GeV)\cdot\frac{\partial}{\partial E_0}\langle\mu_{tot}\rangle_o \tag{4.10}$$

with $\langle\mu_{tot}\rangle_o^{1\,GeV}$ being the total number of photoelectrons corresponding to the time integrated photon flux $I\left(Z_s,\Theta_s,\rho,l,\Phi,t_d\right)$ at DOM o as determined by Photonics.

Two tools, which allow to query the Photonics tables to relate the simulation results of Photonics to a given cascade hypothesis $\underline{C}_0$ (eq. (5.1)), exist: PhotoRec and PhotoSplines. Due to the coarse binning used in Photonics, the tabulated results need to be interpolated. The PhotoRec interface is based on a fast linear interpolation and PhotoSplines uses a smooth spline fit to reduce interpolation artifacts, thus being computationally more intensive. An example of the precision of such a spline fit is shown in Figure 4.4 for a delay time distribution according to the Pandel PDF, eq. (5.12).
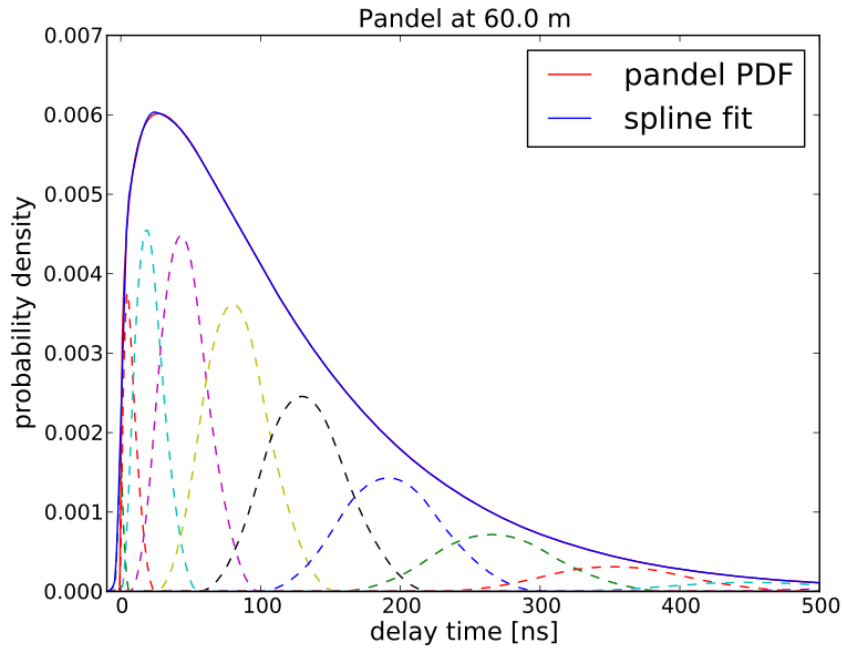
FIGURE 4.4: The figure shows a delay time pdf according to Pandel as well as a spline fit. The resulting curve for the fit is the sum of the base splines (dashed). Figure from [55]

4.5   Simulating the Detector Response

In the simulation chain, summarized in Figure 4.5, the last step is simulating the detector response to a given light signal. Based on the photon arrival time distributions of Photonics the HitMaker module characterizes the emission of photoelectrons at the

photocathode of the PMT. For each hit its arrival time and the corresponding number of emitted photoelectrons is derived. Together with additional information about stochastic features like PMT pre- and after pulsing, the results are stored for each DOM. In a next step the amplification of the emitted photoelectrons needs to be simulated. This is done by the PMTSimulator module. Base on the input from the HitMaker module, the amplified charge for each hit is calculated based on the PMT charge response function, eq. (3.4). In addition the pulse is smeared in time according to the PMT pulse shape. Finally a corresponding waveform is produced, taking into account that the PMT behaves non-linear for large input currents [55]. The very last step consists of simulating the DOM electronics, i.e. the FPGA logic. This is done using the DOMsimulator module.

FIGURE 4.5: The Figure shows a flow chart of the different steps necessary to produce Monte Carlo simulations of neutrino events in IceCube. Figure from [55]

Chapter 5

Cascade Reconstruction Algorithms

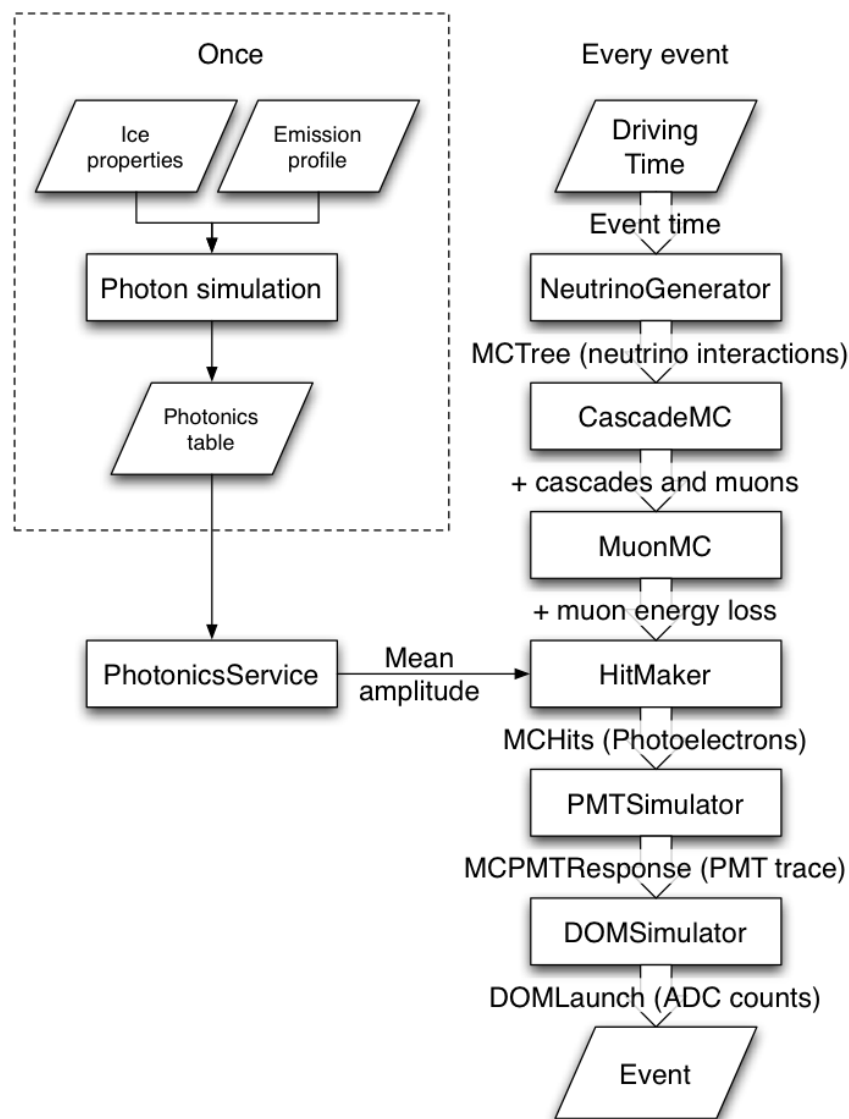A neutrino, that interacts via the Glashow resonance in the detector, will most likely (about 80% of all cases) produce a hadronic or electromagnetic particle shower. Hence a search for the Glashow resonance is a search for high energetic cascade like events, i.e. events with an almost spherical light distribution and a photon yield equivalent to a shower energy of $E_0 \sim 6\,\text{PeV}$. Thus this chapter will focus on cascade reconstruction algorithms. Those algorithms have been designed to extract a set of parameters $\underline{C}_0$ describing the properties of a cascade from the set of recorded signals. In a second step by addressing the question, which properties maximize the probability for such a neutrino to have caused the observed particle shower, the underlying neutrino properties would have to be inferred from those observables. This is not straightforward, since not only the Glashow Resonance produces such showers, but also charge-current $(\nu_e, \bar{\nu}_e)$ and neutral current (all flavors) interactions contribute. In addition possible interactions of the primary neutrino during the propagation through the earth have to be taken into account. This thesis primarily addresses the first step.

Cascades with energies below the LPM regime[1] typically have a longitudinal extension of less than 10 m. Given a smallest possible distance between two DOMs of 17 m, the elongation of a shower can not be resolved in IceCube. Hence such cascades appear as point-like Cherenkov emitters and thus can be described by a set of seven parameters (to be reconstructed):

$$C_0 = \{\vec{x}_0, t_0, \theta_0, \Phi_0, E_0\} \tag{5.1}$$

---

[1] The LPM effect causes significant longitudinal shower elongation for $E_0 > 100\,\text{PeV}$.

The first three parameters $\vec{x}_0$ are given by the the position of the cascade, i.e. the point-like emitter. The time, at which the emission started, is denoted by the vertex time t_0. Two parameters describe the direction of the cascade (zenith θ_0 and azimuth Φ_0, anti-parallel to direction of the longitudinal shower development). Finally the energy of the cascade is referred to as E_0. The convention of the shower direction (θ_0, Φ_0) to be antiparallel to the direction of the primary lepton was chosen to point back to the source of the possibly underlying neutrino. Hence the cascade direction and the direction at which cherenkov photons are radiated form an angle of $\alpha = \pi - \theta_c$. Which methods are currently being used to determine these parameters from the measurement, shall be discussed in this section.

The IceTray Software

The IceTray Software provides the framework in which all data processing and data analysis tasks are performed. The data is organized in so called I3Frames, a container class which holds several frame objects, which themselves are classes within IceTray. Such objects are mainly raw data, waveforms and pulses (Q-frames) or subsequent reconstruction results (P-frames) corresponding to one event. Data, structured in that way, can be stored to disk in so called i3-files. Within IceTray the data can be processed by using the modules, provided by a meta project. The meta-project used for this thesis is the IceRec meta project, which provides a set of common reconstruction tools. A module can access frame objects in order to use the stored information to perform tasks. The result will then be stored in one or more additional frame objects. Some modules require so called services for successful processing. These services provide additional information to the modules (other than the data shipped as frame objects), such as the tabulated results of the photonics simulation.

In addition it is possible to convert data stored as frame objects into tabulated information, such as the ROOT and HDF5 formats for faster table based analysis.

5.1 The First Guess

Several first guess algorithms, which provide a rough estimate of the cascade parameters $\underline{C}_0$, are available within the IceRec framework. When using those algorithms, it should be noted that they are supposed to give somewhat reliable estimates for contained events only. Consider a partially contained cascade with an interaction vertex somewhere outside the detector boundaries. By construction the vertex provided by the center of gravity method (see below) will lie within the detector, which will subsequently

distort the reconstructed vertex time.

The first guess algorithms used in this thesis are described below.

CFirst

The CFirst algorithm aims at the reconstruction of vertex and time of a cascade [49]. In a first step the center of gravity (COG) is used to determine the vertex position. The positions $\vec{x}_o$ of the DOMs o, which recorded light, are weighted and averaged.

$$\vec{x}_{cog} = \frac{\sum_o w_o \vec{x}_o}{\sum_o w_o} \tag{5.2}$$

$$\tag{5.3}$$

They weights w_o are related to the total charge $Q_{o,tot}$ of the respective DOM o: $w_o = Q_{o,tot}^\alpha = (\sum_i q_{oi})^\alpha$. Here i runs over all pulses with corresponding charge q_{oi} in DOM o. The amplitude weight power α allows to adjust the weighting, from no weighting applied ($\alpha = 0$) to full weighting ($\alpha = 1$) [50]. When CFirst was used in this thesis, no weighting was applied.

In addition to determine the vertex position, CFirst provides an estimate of the time t_0, at which the cascade started, based on the previously estimated vertex position. The following trial time t^{trial} can be defined [50]:

$$t_o^{trial} = t_{o1} - \frac{|\vec{x}_k - \vec{x}_{cog}|}{c_{ice}} \tag{5.4}$$

with t_{o1} being the time of the first pulse in DOM o. In case of no scattering this time would be the same for each DOM with $t_o^{trial} = t_0$. However since light scatters until it reaches the DOM the earliest possible time needs to be found. One therefore selects all DOMs o' within a sphere of radius r=100m around the center of gravity position $\vec{x}_{cog}$ ($o' \in S = \{DOMs\}_{r<100m}$). For each DOM o' in this set S the trial time $t_{o'}^{trial}$ is calculated using (5.4). In the next step for all other DOMs o'' in S (with $o'' \neq o'$) one can calculate the the delay time w.r.t. straight propagation from $\vec{x}_{cog}$ to DOM o'', assuming $t_{o'}^{trial}$ would be the true interaction time t_0:

$$t_{o''}^d = t_{o''1} - t_{o'}^{trial} - \frac{|\vec{x}_{o''} - \vec{x}_{cog}|}{c_{ice}} \tag{5.5}$$

Now it is possible to count the number of DOMs N, which satisfy that their delay time $t_{o''}^d$ w.r.t. $t_{o'}^{trial}$ lies in a 200ns time window $t_d \in [0ns, 200ns]$. The algorithm returns the smallest $t_{o'}^{trial}$ with $N > 4$ [49] as interaction time t_0 [50].

Tensor of Inertia

The Tensor of Inertia algorithm estimates the direction of the cascade from the topology

of the light distribution among the DOMs o, which measured light during an event. It uses the well known expression for the tensor of inertia, with the mass m_o being replaced by the total charge Q_o, seen by the DOM o [47]:

$$I_{ij} = \sum_o Q_o^\alpha \left(\delta_{ij} \vec{x}_o^2 - x_{o,i} x_{o,j} \right) \tag{5.6}$$

α again controls by how much each DOM o is weighted by its charge Q_o in the above expression. The position of the DOM o is given by $\vec{x}_o$. By calculating the eigenvalues λ_i of this tensor, it is possible to find its principal axes. The principal axis corresponding to the smallest λ may give an estimate of the direction, since the light distribution is assumed to be elongated along the arrival direction at high energies, where elongation becomes non-neglectable. However the ratio between the eigenvalues $\frac{\lambda_i}{\lambda_j}$ $(i, j \in \{1, 2, 3\} ; i \neq j)$ provides a useful variable to discriminate spherical light patterns (i.e. cascades) from track-like structures, which have an overwhelming background contribution of downgoing atmospheric muons.

5.2 Maximum Likelihood Reconstruction

The most powerful and thus computationally intensive reconstruction algorithms included, make use of the likelihood principle. As we have already seen, many probabilistic processes are involved, until the final data is created in form of the calibrated light pulses of all DOMs. These range from the photon propagation through the ice to all the effects concerning the detector itself, like the SPE-charge response of the PMT. By convoving all these probabilistic processes, it is possible to formulate the conditional probability of observing data $\underline{R}$ given a cascade with parameters $\underline{C}$ as the probability $P(\underline{R}|\underline{C})$ [50]. Here the detector response $\underline{R}$ is a function of the parameters $\underline{C}$. However event reconstruction can be thought of as solving the inverse problem, namely to extract those parameters $\underline{C}$ from a given observation $\underline{R}$, which are best supported by the data. This problem is known as statistical inference. The difficulty lies in the fact that different classes of events (different sets $\underline{C}_i$) might have caused the observation $\underline{R}$. Two main approaches to statistical inference are found in statistics. The method of Bayesian inference, based on the Bayes theorem, requires pre-knowledge about the probability distribution $P(\underline{C})$, the so called prior-distribution. This knowledge allows to invert the conditional probability $P(\underline{R}|\underline{C})$ [55]:

$$P(\underline{C}_i|\underline{R}) = \frac{P(\underline{R}|\underline{C}_i) P(\underline{C}_i)}{\sum_j P(\underline{R}|\underline{C}_j) P(\underline{C}_j)} \tag{5.7}$$

Since the prior distribution is typically unknown for most experiments in physical sciences, another method is needed. According to [72] all necessary information to determine the relative support of one hypothesis $\underline{C}_i$ compared to another $\underline{C}_j$ by the data $\underline{R}$, is described by the likelihood function L, defined as follows:

$$L\left(\underline{C}_i|\underline{R}\right) \propto P\left(\underline{R}|\underline{C}_i\right) \tag{5.8}$$

The likelihood of a hypothesis $\underline{C}_i$ based on a measurement $\underline{R}$ is proportional to the probability that this observation occurs under the conditions $\underline{C}_i$. The likelihood itself can not be interpreted as a probability(density), as it may not be normalized and transforms differently under variable transformations. The absolute value of the likelihood therefore has no meaning w.r.t the support of a hypothesis and an absolute comparison of different hypotheses on different data is to be avoided. It is the ratio between the likelihoods of two competing hypothesis data, which, based on the same data, quantifies which hypothesis is preferred. This is summarized in the Likelihood axiom [72]:

> *"Within the framework of a statistical model, all the information which the data provide concerning the relative merits of two hypotheses is contained in the likelihood ratio of those hypotheses on the data, and the likelihood ratio is to be interpreted as the degree to which the data support the one hypothesis against the other".* (A. W. F. Edwards)

Hence the best matching hypothesis is defined by the set of parameters $\underline{C}_0$, which maximize the likelihood L. In that context it is useful to define the natural logarithm of the likelihood as the support function [72], since it avoids numerical difficulties while preserving the position of the maximum [50]. One thus minimizes the negative logarithm of the likelihood to find the best fitting parameters $\underline{C}_0$:

$$-\nabla_{\underline{C}} \ln L\left(\underline{C}|\underline{R}\right)\bigg|_{\underline{C}=\underline{C}_0} = 0 \tag{5.9}$$

In order to find the minimum of this expression, additional constants in the support function, such as the constant of proportionality of the likelihood function, can be discarded.

The data $\underline{R}$ in our case consists of the calibrated light pulses of all DOMs.

$$\underline{R} = \{t_{oi}, \Delta t_{oi}, n_{oi}\} \tag{5.10}$$

with the DOMs being indexed by o and the pulses in each DOM being denoted by i. A pulse is characterized by its starting time (leading edge) t_{oi}, its width Δt_{oi} and its charge n_{oi} in units of photoelectrons [50].

5.3 The Second Estimate

Cascade Likelihood Vertex Reconstruction

The Cascade Likelihood Vertex Reconstruction (CscdLlh) algorithm, which is based on the maximum likelihood technique, described above, is used in this thesis to further improve the result of the vertex and timing information provided by CFirst. CscdLlh, as used in this thesis, relies on the Powell algorithm [73] to minimize a likelihood, describing that DOM o at a distance $d_o = |\vec{x}_o - \vec{x}_0|$ from the hypothetical cascade vertex $\vec{x}_0$ measures its first pulse at a delay time $t_{o1}^d = t_{o1} - t_0 - \frac{d_o}{c_{ice}}$ w.r.t to the hypothetical vertex time t_0. The delay time thus is the additional time it takes for a photon to arrive at the DOM due to scattering compared to straight unscattered propagation. The support function reads:

$$-\ln L\left(t_0, \vec{x_0}|t_{o1}^d, \vec{x}_o\right) = -\ln\left[\Pi_o p_o\left(t_{o1}^d, \vec{x}_o|t_0, \vec{x_0}\right)\right] = -\sum_o \ln p_o\left(t_{o1}^d, \vec{x}_o|t_0, \vec{x_0}\right) \quad (5.11)$$

The probability density is based on the Pandel-pdf [74], which assumes homogenous and isotropic optical properties of the ice. It reads [50]:

$$p_o\left(t_o^d, d_o\right) = \frac{dp}{dt_o^d}\left(t_o^d, d_o\right)\Delta t = \frac{a\left(at_o^d\right)^{b-1}\exp\left(-at_o^d\right)}{\Gamma\left(b\right)}\Delta t \quad (5.12)$$

$$a = \frac{1}{\tau} + \frac{c_{ice}}{\lambda_a} \quad (5.13)$$

$$b = \frac{d_o}{\lambda} \quad (5.14)$$

The following coefficients are used: $\lambda = 47\,\text{m}$, $\tau = 450\,\text{ns}$, $\lambda_a = 98\,\text{m}$ [50], with λ_a being the absorption length in ice while τ and λ are free parameters in the parametrization, which have been extracted from simulations. Since the bias due to the assumption of homogenous ice increases with increasing number of scatterings, i.e. with increasing delay time t_d, only the first pulse of each DOM was used in the algorithm for the purpose of this thesis. However it is due to this simplified treatment of the optical properties of the ice, that Cscd-Llh is much faster than more sophisticated algorithms, which include a full treatment of the optical properties of the ice (compare sec. 4.3).

Atmospheric Cascade Energy Reconstruction

The Atmospheric Cascade Energy Reconstruction (ACER) algorithm is a likelihood based energy reconstruction, which semi-analytically solves for the cascade energy E_0 based on its vertex seed. For the purpose of this thesis ACER was seeded with the vertex solution provided by Cscd-Llh. Since ACER only reconstructs the energy, it includes a proper treatment of the ice by making use of the tabulated results of the

Photonics simulation, while being sufficiently fast. In section 4.4 it was shown, that the Photonics simulation allows to relate the mean total charge (number of photoelectrons) $\langle \mu_{tot} \rangle_o$, expected in DOM o given a cascade with hypothetical parameters $\underline{C}_0$, to the total charge $\langle \mu_{tot} \rangle_o^{1\,GeV}$ of a 1 GeV light source determined by simulation. It is assumed that the total charge n_o in DOM o follows a Poisson distribution, characterized by the total charge $\mu_o = \langle \mu_{tot} \rangle_o + \nu T$, where νT denotes the noise contribution (rate ν) over the event length T. The likelihood thus reads:

$$L\left(E_0|n_o\right) = \prod_{DOMs(o)} \frac{\mu_o^{n_o} e^{-\mu_o}}{n_o!} \tag{5.15}$$

The corresponding support function can be minimized analytically w.r.t E_0, which yields the following equation:

$$-\frac{\partial}{\partial E_0} \ln L\left(E_0|n_o\right) = \sum_o \left[\langle \mu_{tot} \rangle_o^{1\,GeV} \left(1 - \frac{n_o}{\frac{E_0}{1\,GeV} \langle \mu_{tot} \rangle_o^{1\,GeV} + \nu T} \right) \right] = 0 \tag{5.16}$$

$$\langle \mu_{tot} \rangle_o^{1\,GeV} = (1\,\text{GeV}) \cdot \frac{\partial}{\partial E_0} \langle \mu_{tot} \rangle_o \tag{5.17}$$

with $\langle \mu_{tot} \rangle_o^{1\,GeV}$ being the total charge returned by Photonics/PhotoRec for DOM o (compare 4.4). This 1-D root finding problem is solved numerically.

Since the predictions of PhotoRec rely on the tabulated Photonics results, which are based on the simulations for different ice models, one has to specify, which ice model shall be used. The AHA photorec tables have been used for ACER throughout this thesis, providing a fast energy estimate.

5.4 The Final Answer

Credo

The Credo algorithm [50] is a likelihood based cascade reconstruction algorithm, that determines all seven parameters C_0 from the calibrated pulses. The basic assumption of this algorithm is that the photonics simulation allows to predict the expected number of photons in each time interval and hence the charge of all pulses in each DOM for a given cascade hypothesis $\underline{C}_0$. The expected charge μ_{oi} of a pulse i with width Δt_{oi} in

DOM o at position $\vec{x}_o$ reads [50]:

$$\mu_{oi}\left(\vec{x}_o, t_{oi}^d, \Delta t_{oi}|\underline{C}_0\right) = \int_{\Delta t_{oi}} dt_o^d \left(\langle\mu_{tot}\rangle_o \frac{dp}{dt_o^d}\left(\vec{x}_o, t_o^d\right) + \nu_{noise}\right) \tag{5.18}$$

$$\approx \left(\langle\mu_{tot}\rangle_o \frac{dp}{dt_o^d}\left(\vec{x}_o, t_o^d\right) + \nu_{noise}\right)\Delta t_{oi} \tag{5.19}$$

$$t_{oi}^d = t_{oi} - \frac{d_o}{c_{ice}} - t_0 \tag{5.20}$$

with d_o being the distance from DOM o to the hypothetical vertex $\vec{x}_0$.

Given the stochastic nature of the involved processes like photon propagation and charge multiplication in the PMT, it is natural to assume that the charges μ_{oi} measured for different pulses (i.e. in different time intervals of the respective waveform) are statistically independent and can thus be modeled with a poisson distribution. The Credo likelihood reads [47]:

$$L\left(\underline{C}_0|\vec{x}_o, t_{oi}, \Delta t_{oi}, n_{oi}\right) = \prod_o \prod_i \frac{\mu_{oi}^{n_{oi}} e^{-\mu_{oi}}}{n_{oi}!} \prod_{o'} e^{-\mu_{o'}} \tag{5.21}$$

Here o and o' denote hit and unhit DOMs respectively. Those unhit DOMs, i.e. DOMs which did not measure light, are included in the fit, because they can provide important constraints to penalize wrong hypothesis. Any hypothesis which predicts charge for such a DOM will exponentially be suppressed.

The expression above yields the following support function:

$$-\ln L = \sum_o \left\{\mu_o - \sum_i \left(n_{oi}\ln\frac{\mu_{oi}}{\mu_o} - \ln(n_{oi}!)\right) - N_o \ln\mu_o\right\} - \sum_{o'}\mu_{o'} \tag{5.22}$$

$$\mu_o = \sum_i \mu_{oi} \approx \langle\mu_{tot}\rangle_o + \nu_{noise}\Delta t_{event} \tag{5.23}$$

with $N_o = \sum_i n_{oi}$ being the total charge recorded in DOM o. The approximation for the total expected charge μ_o of DOM o is valid as long as all pulses of the full waveform have been considered. Throughout this thesis the commonly used simplex algorithm [75] was applied to minimize the expression above in all seven parameters to determine the best fitting cascade hypothesis $\underline{C}_0$.

It should be noted that the contribution of a DOM to the likelihood increases with increasing charge, not only because they should have measured the most pulses, but more importantly because the relative error of a Poisson distribution $\frac{\Delta\mu}{\mu}$ decreases with increasing μ as $\frac{1}{\sqrt{\mu}}$. Thus the penalty for the same relative deviation of measured charge from predicted charge $\frac{\Delta\mu_{oi}}{\mu_{oi}} = \frac{\mu_{oi} - n_{noi}}{\mu_{oi}}$ for a single pulse increases with the expected charge. That means, that the Likelihood becomes more sensitive to possible deviations from the assumed poisson characteristics of the DOM with increasing charge. By a

DOM wise comparing the expected total charge and observed total charge, it was found in [50] that for bright DOMs (i.e. $Q_o^{tot} > O(100 p.e.)$) the relative error $\frac{\Delta \mu_{tot}}{\mu_{tot}}$ stays almost constant with increasing expected total charge μ_{tot}. This was interpreted as a hint, that bright pulses might not properly be described by a poisson distribution. The Credo likelihood was thus expanded such that bright pulses above a threshold charge with $n_{oi} > \alpha_t^2$ are compared to a Gaussian distribution with $\sigma = \frac{n_{oi}}{\alpha_t}$. Different values of α_t corresponding to relative errors of $\frac{\sigma}{n_{oi}} \in \{5\%, 10\%, 20\%, 50\%\}$ have been tested, but the results of this change have not been conclusive and hence are commonly not used during reconstruction. Details can be found in [50]. Throughout this thesis a value $\alpha_t = 1000$ ($\alpha_t^2 = 10^6$ p.e.) was chosen, making sure, that only poissonean terms enter the likelihood.

Monopod

Monopod, another likelihood based cascade reconstruction algorithm, is the single source specialization of the hybrid reconstruction algorithm millipede. Millipede is designed to reconstruct the energy loss in each segment of a track by fitting a cascade in each segment, using a pulse based Poisson likelihood similar to the one used in Credo. However since reconstructing single cascades similar to Credo already is computationally intensive, several changes were needed in order to speed up that process of dealing with multiple sources. Thus those changes are also present in Monopod, making that algorithm significantly faster than Credo. Whereas Credo numerically minimizes the full seven-dimensional likelihood, as discussed above, Monopod only minimizes in 6 dimensions, leaving the energy reconstruction for a subsequent semi-analytical treatment, using the ACER approach w.r.t to the charge measured in each time bin of the waveform. An additional gain in computational speed is obtained by using the spline interpolated version of the Photonics tables. Since the derivatives of those splines are known by construction, Monopod provides gradient information to the minimizer, making numerical minimization more efficient.

The Monopod Likelihood and support functions read:

$$L\left(\underline{C}_0 | \vec{x}_o, t_{oi}, \Delta t_{oi}, n_{oi}\right) = \prod_o \prod_i \frac{\mu_{oi}^{n_{oi}} e^{-\mu_{oi}}}{n_{oi}!} \tag{5.24}$$

$$\ln L\left(\underline{C}_0 | \vec{x}_o, t_{oi}, \Delta t_{oi}, n_{oi}\right) = \sum_{o,i} \left[n_{oi} \ln \mu_{oi} - \mu_{oi} - \ln \Gamma\left(n_{oi} + 1\right)\right] \tag{5.25}$$

o and i denote the DOM and the time window, in which a certain amount of charge was measured, respectively. The Γ function is used to generalize the factorial of the respective Poisson distribution to the case of having continuous parameters. The mean expected charge $\mu_{oi} = \langle \mu_{tot} \rangle_{oi} + \nu_o$ is based on the Photonics prediction $\langle \mu_{tot} \rangle_{oi}$. However similar to ACER the linear relationship between the energy of a cascade E_0 and its light

yield is used:

$$\langle \mu_{tot} \rangle_{oi} \left(\vec{x}_o, t_{oi}, \Delta t_{oi} | \underline{C}_0 \right) = \frac{E_0}{1\,GeV} \langle \mu_{tot} \rangle_{oi}^{1\,GeV} \left(\vec{x}_o, t_{oi}, \Delta t_{oi} | \underline{C}_{0;-1} \right) \qquad (5.26)$$

$$\langle \mu_{tot} \rangle_{oi}^{1\,GeV} \left(\vec{x}_o, t_{oi}, \Delta t_{oi} | \underline{C}_{0;-1} \right) = \int_{\Delta t_{oi}} dt^d \frac{dp}{dt^d} \left(\vec{x}_o, t^d \right) \langle \mu_{tot} \rangle_o^{1\,GeV} \qquad (5.27)$$

with $\underline{C}_{0;-1}$ being the set of all Cascade parameters $\underline{C}_0$ except the energy E_0. Once the position, time and direction of the Cascade have been determined via numerical minimization, the energy can be reconstructed in a next step by minimizing the support given above analytically:

$$-\frac{\partial}{\partial E_0} \ln L \left(E_0 | n_{oi} \right) = \sum_{o,i} \left[\langle \mu_{tot} \rangle_{oi}^{1\,GeV} \left(1 - \frac{n_{oi}}{\frac{E_0}{1\,GeV} \langle \mu_{tot} \rangle_{oi}^{1\,GeV} + \nu_o} \right) \right] = 0 \qquad (5.28)$$

This equation is solved for the energy E_0 numerically using the Newton-Rhapson method [76].

Monopod offers the user the option to provide a constant factor $\xi \in [0,1]$ to artificially downscale the Photonics prediction to $\langle \mu'_{tot} \rangle_{oi}^{1\,GeV} = \xi \langle \mu_{tot} \rangle_{oi}^{1\,GeV}$.

It is possible for all likelihood-based algorithms to apply an iterative fitting scheme as follows: based on the seed a first likelihood minimization is done to provide a first solution. At that point it is not possible to conclude that this minimum is global. One thus seeds that solution into another iteration of the respective algorithm, while the direction of the previous solutions is altered. If the support function, evaluated at the new solution, which is found after reminimization of all parameters, has a smaller value than the previous solution, then that new solution will be considered as best fitting hypothesis. This procedure can be repeated arbitrarily often.

5.5 The "True" Cascade Parameters

In order to make comparisons between the reconstructed cascade parameters and the simulated showers, as we intend in the next chapter, a meaningful Monte Carlo Truth must be chosen. "Meaningful" in this context means to use a value, to be found by the algorithm, which does not necessarily need to equal the respective property of the primary neutrino, as already discussed.

The **energy E_{true}**, which a cascade reconstruction is supposed to find, can only be given by its visible energy losses. This differs from the primary neutrino Energy E_ν for two reasons. First, in some interactions (CC/NC/GR leptons) the kinematic processes

involved need to be considered. Secondly as described in section 2.3 in case of hadronic showers, the visible energy might differ from the total energy deposited in the shower. Hence the Monte Carlo Truth of the Cascade energy E_{true} is given by the sum of all visible energy losses E_i according to CMC ($E_{true} = \sum_i E_i$ with E_i being the energy of a sub-cascade created by CMC, compare 4). This is visualized in figure 4.1.

One underlying assumption behind the cascade reconstruction algorithms, used in this thesis, is the point like emission profile of those showers. This approximation works as long as the elongation of a cascade is smaller than the distance between two optical modules in IceCube ($17\,m$). The **vertex $\tilde{x}_{true}$** will thus be defined as the position at which the shower brightness peaks (shower maximum), which is the energy loss weighted average position of the sub cascades created by CMC (center of gravity): $\vec{x}_{true,i} = \frac{\sum_i E_i x_i}{\sum_j E_j}$ (compare figure 4.1). The distance from the interaction vertex to the position of the
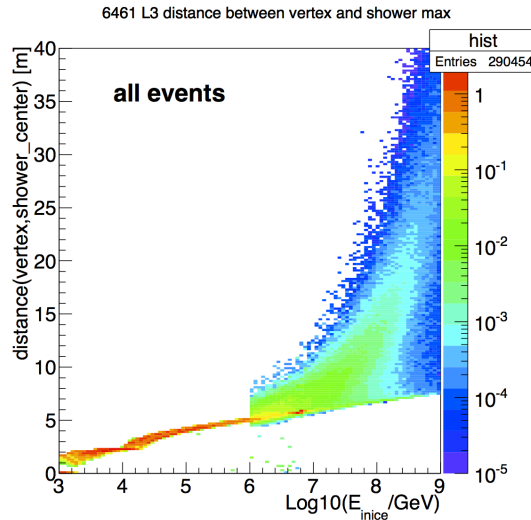

FIGURE 5.1: The figure visualizes the energy dependence of the cascade elongation as simulated in IceCube by showing the distance between the position of the shower maximum and vertex position of the neutrino interaction.

shower maximum gives a good estimate of the cascade elongation. The energy dependence of this distance is shown in figure 5.1. The sharp edge at $E_i = 1\,\mathrm{PeV}$ is due to the energy threshold above which the LPM[2] effect is simulated in CMC. The red dot at $\log \frac{E}{GeV} = 6.8$ shows the position of the Glashow Resonance. Thus those cascade have a typical length $5\,m < d < 7\,\mathrm{m}$ in good agreement with the estimated length $d \approx 6.4\,\mathrm{m}$ using the Heitler model (compare sec. 2) and hence the point like approximation is valid for Glashow Resonance Cascades.

---

[2]The LPM effect denotes a strong decrease of the Bremsstrahlungs cross-section due to quantum interference between the scattering amplitudes of different atoms. Since this effect is only important above $E_e \approx 10\,\mathrm{PeV}$ it has no influence for the purpose of this thesis.

Since the whole simulation chain assumes the secondary particles to follow the direction of the primary neutrino, its direction will be used to define the true shower zenith θ_{true} and azimuth Φ_{true}.

Chapter 6

Reconstruction Performance for Simulated Glashow Resonance Cascades

One important step towards exploiting the Glashow resonance in a search for a diffuse flux of astrophysical neutrinos is the capability to reliably reconstruct the properties of the neutrino induced electromagnetic and hadronic showers in IceCube. An increasingly precise knowledge of the properties of a single event would be beneficial in estimating the probability that a given sample of neutrino event candidates contains an astrophysical signal, i.e. that the distributions of the cascade parameters within that sample are likely not to be explained by background (i.e. cosmic ray muons, atmospheric neutrinos). In that context the energy distribution is of special importance, since rejecting the hypothesis, of that sample being consistent with atmospheric neutrinos, will almost entirely rely on the reconstructed energies.

Due to the absence of a viable artificial source of neutrinos, an analysis of the reconstruction capabilities of current reconstruction algorithms has to rely on the combined study of simulated data and the use of the IceCube Standard Candle Lasers. Only the Standard Candle provides a light yield strong enough to mimic particle showers with energies near the Glashow resonance $E = 6.3 \, \text{PeV}$. The goal of this thesis is to test the currently most sophisticated cascade reconstruction algorithms (Credo and Monopod) and evaluate their reconstruction performance using simulated neutrino events and Standard Candle data.

In this chapter the part of the analysis which is based on simulated data will be described.

6.1 Electron Neutrino Monte Carlo Dataset

This analysis is based on the IceCube IC79 (79 strings) electron neutrino Monte Carlo dataset 6461. The 79-strings detector configuration represents the largest detection volume, for which official Monte Carlo data were available.

Dataset Details

- dataset id: 6461 (processed to Level2)

- geometry: IC79

- ice model: SPICEMie

- photon propagator: Photonics

- generator: neutrino-generator

- energy range: $10^{1.7}\,\mathrm{GeV} < E_\nu < 10^9\,\mathrm{GeV}$ with $E^{-\gamma}$ ($\gamma = 1$)

- angular range: $0° < \theta < 180°$

- software version: simulation.releases.V02-06-02 with std-processing.releases.11-02-00

In order to provide sufficient statistics at high energies, this dataset was simulated using a hard primary neutrino spectrum with a slope of $\gamma = 1$. In order to make statements about an presumably astrophysical flux with a generic slope of $\gamma = 2$, all events have to be reweighted. The resulting neutrino spectrum after online filtering (black) as well as the individual contributions from several IceCube online data filters (colored) are shown in figure 6.1 . The Glashow resonance is visible as a very sharp peak at energies around $\log{(E/\mathrm{GeV})} \approx 6.8$. The cascade filter (green), which was designed to select events with cascade like light patterns, contains almost all Glashow Resonance events, as expected.

6.2 Cascade Reconstruction Performance for simulated Electron Neutrino Events

In this analysis we use the cascade Level3 filter data (cf. sec. 3.5), since it already contains the results of computationally expensive cascade reconstruction algorithms. Based on the reconstructed cascade position by Credo, as run at Level3, all events are tagged
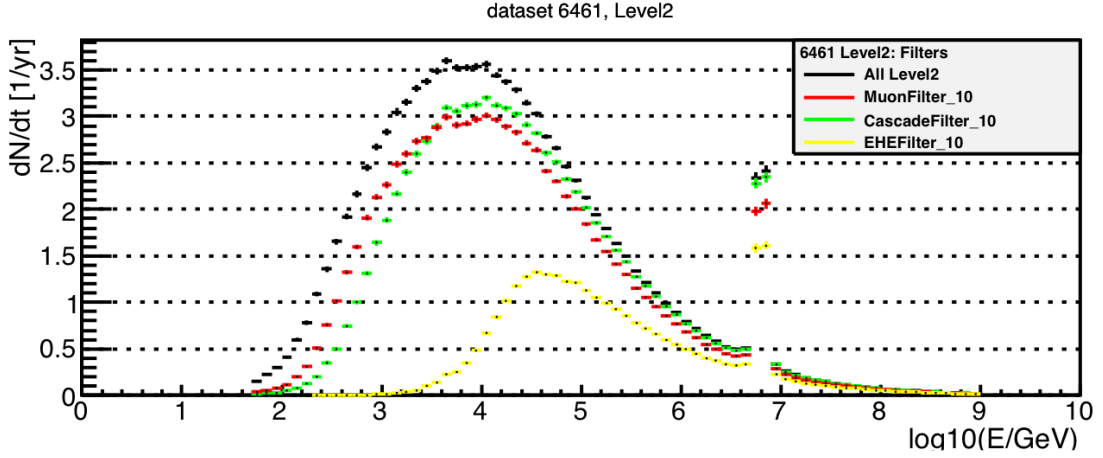
FIGURE 6.1: **Dataset 6461 at Level2:** The logarithmic energy spectrum of all events (black) and of individual IceCube filters (colors) is shown for a neutrino flux expectation of $\frac{d\Phi}{dE} = 10^{-8} \left(\frac{E}{\text{GeV}}\right)^{-2} \text{GeV}^{-1}\text{cm}^{-2}\text{s}^{-1}\text{sr}^{-1}$ and $\Phi_{\nu_e}/\Phi_{\bar{\nu}_e} = 1$. The Glashow resonance is visible as a sharp peak at $\log \frac{E}{\text{GeV}} \approx 6.8$

as contained or uncontained. Contained events have their reconstructed x and y coordinates within the detection volume and their brightest (highest charge) DOM not on the outer strings. In addition to the above mentioned result of 1-iteration Credo, the result of 1-iteration Monopod is available. The following settings for Credo and Monopod have been used for the Cascade Level3 processing:

Credo 1-iteration

- pulses: TWOfflinePulsesHLC

- ice model: AHA

- photonics interface: PhotoRec

- seed: Cscd-Llh (position and time), Tensor of Inertia (direction), ACER (energy)

- Credo "IC40-Corrections" [1] (dynamic scaling of the photonics predicted light yield)

Monopod 1-iteration

- pulses: OfflinePulses

- ice model used: SPICE1

- photonics interface: PhotoSplines

---

[1]This name reflects, that those corrections have been implemented at the time, when IceCube was run in its partial IC40 configuration.

- seed: Credo 1-iter (position, time, direction, energy)

- "Monopod Scaling Factor" (constant factor of 0.58, lowering the photonics pre-dicted light yield)

The electron neutrino Monte Carlo simulation dataset 6461 at Level3 was chosen for a first study of their performance. Figure 6.2 shows the distributions of events according to their reconstructed Credo vertex position in the xy-plane (right), as well as the distribution of the true positions (left). The distribution of the reconstructed and the true positions in that plane are very similar for contained events. Only at the boundary of the detector and beyond differences appear. This indicates that reconstructing uncontained events has to be regarded as a challenge. The distribution based on the Monopod reconstruction (not shown) does not differ from the Credo result.

In order to obtain a realistic estimate of the reconstruction performance, only contained
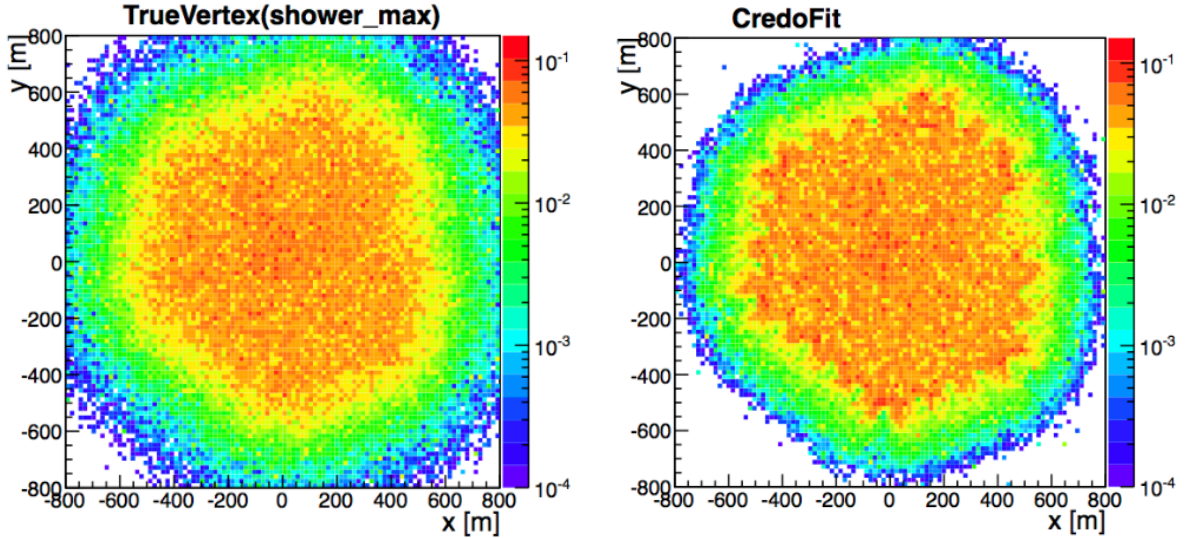

FIGURE 6.2: **Electron neutrino Monte Carlo (Level3):** x versus y position of the shower maximum (left) and of the reconstructed cascade position obtained by 1-iteration Credo (right).

events ($CascadeL3\_Containment = True$) will subsequently be considered, since those are easier to reconstruct. For the same reason an additional loose cut on the z-component of the true position of the shower maximum has been made, to select only those events, which deposited most of their light inside the detector ($-500\,\mathrm{m} < z_{true} < 500\,\mathrm{m}$). This set of cuts will subsequently referred to as "weak containment".

Vertex Resolution

The distributions of $\Delta x = x_{reco} - x_{true}$ and $\Delta z = z_{reco} - z_{true}$ for events, with primary neutrino energy E_ν satisfying $4.0\,\mathrm{PeV} < E_\nu < 6.3\,\mathrm{PeV}$, are shown in Figure 6.3
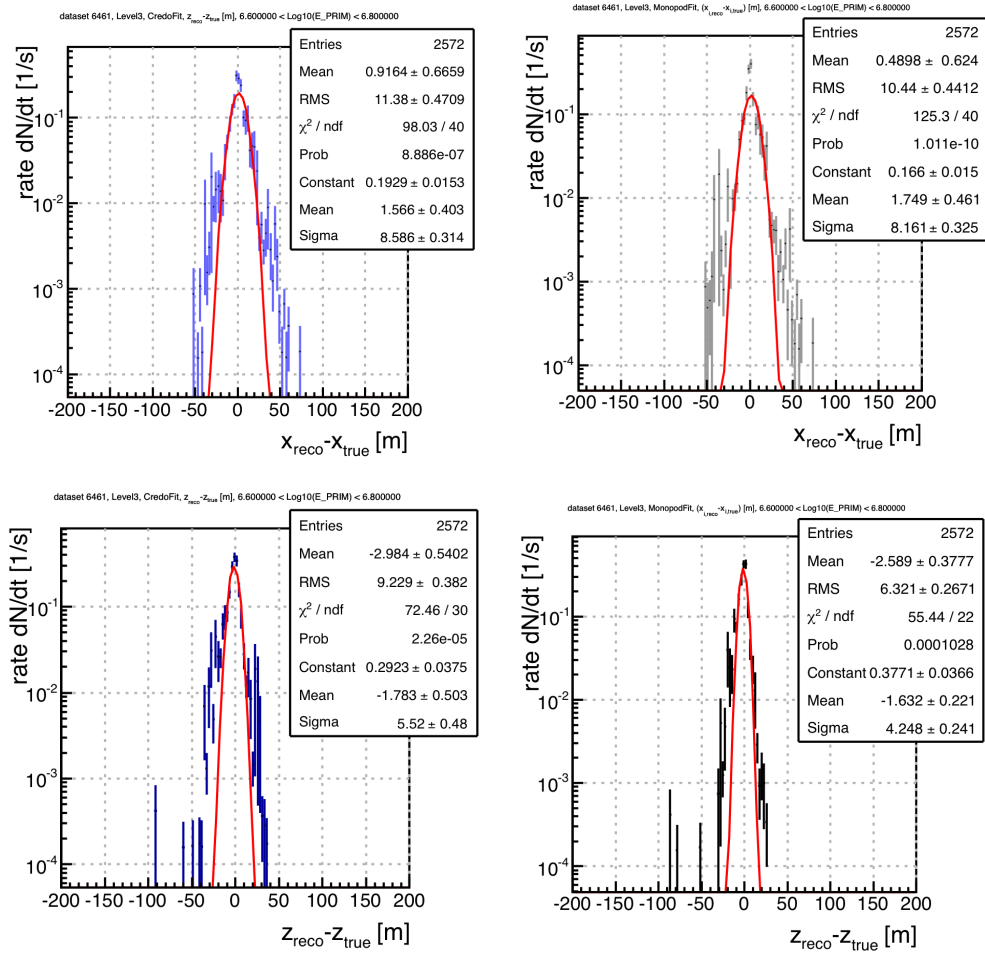
FIGURE 6.3: **Electron neutrino Monte Carlo (Level3):** A comparison of the vertex distribution Δx (top) and Δz (bottom) for Credo (left) and Monopod (right) for contained events with energies $4.0\,\text{PeV} < E_\nu < 6.3\,\text{PeV}$

for Credo and Monopod. Both algorithms show a resolution in x of about $\sigma_{\Delta x} \approx 8\,m$ in this energy range while showing a bias of up to $\mu_{\Delta x} \approx 2\,m$. The results for y are similar. Due to the denser population of DOMs in the z direction compared to x and y, the average resolution of the z coordinate is slightly better with $\sigma_{\Delta z} \approx 5\,m$. Both algorithms on average tend to underestimate the z position with $\mu_{\Delta z} \approx -2\,m$. It should be noted that the large non-Gaussian tails visible above, are due to events, that are close to the detector boundary or lie within the dust layer and thus are only partially contained. By further constraining the sample to be well-contained above the dust layer with $x_{true}^2 + y_{true}^2 < (350\,\text{m})^2$ and $50\,\text{m} < z_{true} < 350\,\text{m}$, those tails largely disappear as shown in Figure 6.4. This set of cuts which selects well contained cascades, will subsequently referred to as "strong containment".

The dependence of the vertex reconstruction performance on the neutrino energy E_ν is shown in Figure 6.5, for the case of weak containment. Both algorithms show their best vertex resolution between $E_\nu = 0.1\,\text{PeV}$ a nd $E_\nu = 1.0\,\text{PeV}$, while generally showing
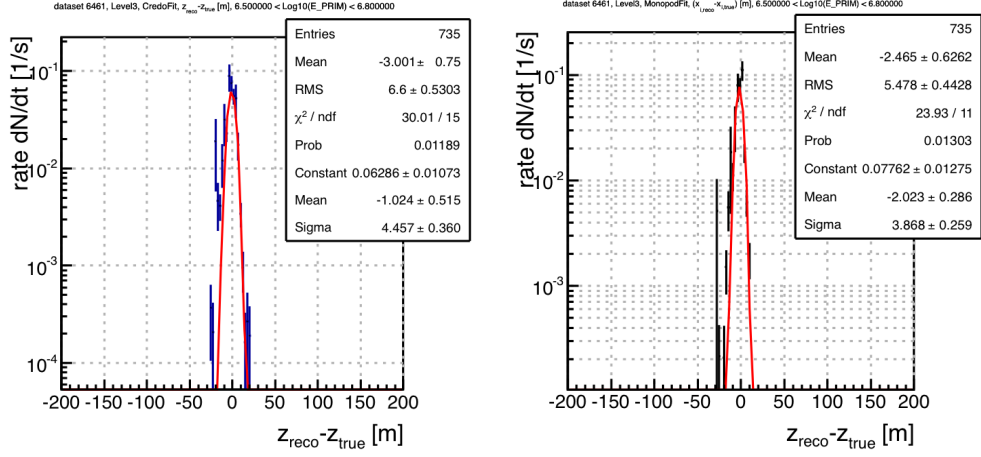
FIGURE 6.4: **Electron neutrino Monte Carlo (Level3)**: A comparison of the vertex distribution Δz for Credo (left) and Monopod (right) with strong containment and energy $3.2\,\mathrm{PeV} < E_\nu < 6.3\,\mathrm{PeV}$

FIGURE 6.5: **Electron neutrino Monte Carlo (Level3):** Bias (top) and resolution (bottom) of the reconstructed vertex coordinates Δx (left) and Δz (right) for Credo, Monopod and Cscd-llh. The bias and resolution are obtained from fits to gaussian distributions in each energy bin.

a very similar energy dependence as expected, since both algorithms essentially share the same likelihood (compare sec. 5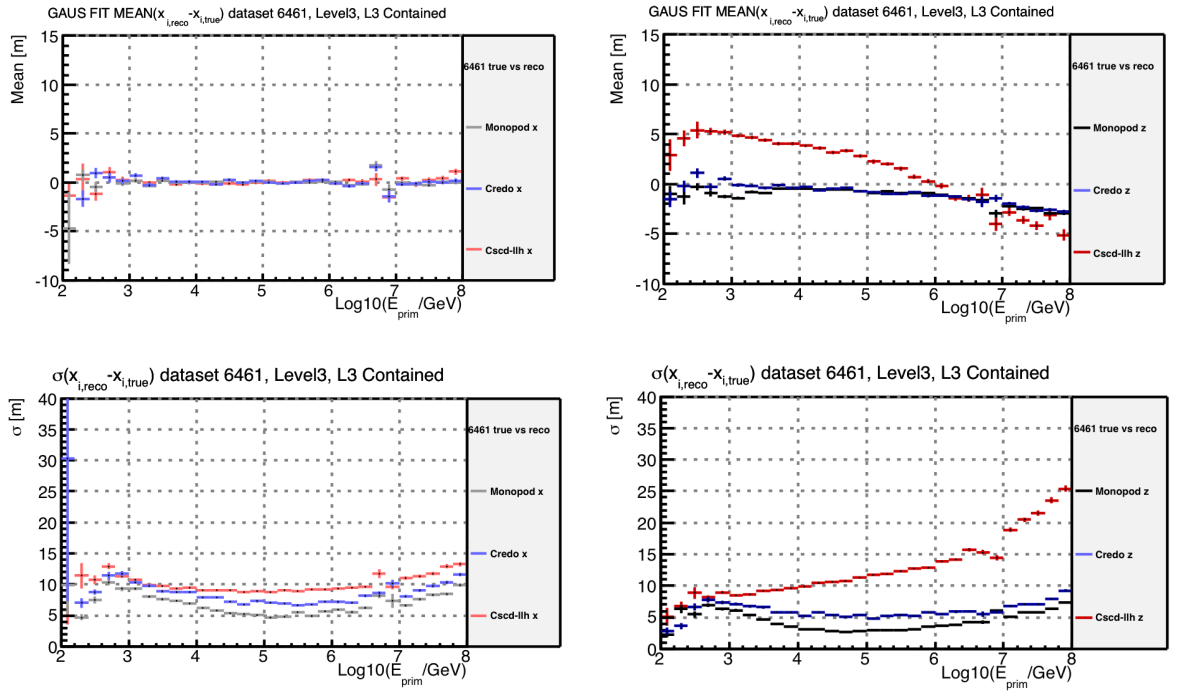.2). Monopod however generally performs better than Credo at all energies. This is mainly for two reasons. First Monopod benefits from having a better vertex seed (Credo Vertex) and secondly it used spline fitted photonics tables, thus minimizing problems due to the coarse binning in the standard photonics tables and its linear interpolations. Finally both algorithms show a significantly improved resolution compared to Cscd-llh (compare sec. 5.3), since they account properly for the inhomogenous optical properties of the ice.

Energy Resolution

The distributions of $\Delta \log E = \log_{10} \frac{E_{reco}}{E_{true}}$ (E_{true} defined as visible deposited energy) are shown for the range $4.0 \, \text{PeV} < E_\nu < 6.3 \, \text{PeV}$ in Figure 6.6 for the case of weak containment. In addition the influence of requiring strong containment, is displayed for the range $3.2 \, \text{PeV} < E_\nu < 6.3 \, \text{PeV}$. The first observation is the presence of large tails for both algorithms in case of weak containment. In addition these tails are systematically different for both algorithms. In case of Monopod those tails lie in the region of overestimated energies, whereas the opposite is true for Credo, which shows tails towards underestimated energies. Constraining the sample to be well contained above the dust layer cuts most of those tails and the distributions become largely Gaussian. For that sample the following biases can be read off: $\mu_{\Delta \log E} \approx -0.02$ (Monopod) and $\mu_{\Delta \log E} \approx 0.13$ (Credo). Both algorithms show a resolution of about $\sigma_{\Delta \log E} = 0.08$. The disagreement of both algorithms with respect to the reconstructed energies seems to be in tension with the expectation of both algorithms being very similar. This will be further investigated in section 6.3. The bias and the resolution of Monopod, Credo as well as ACER (compare sec. 5.3) are shown in Figure 6.7 over the full energy range. The energy dependence of the bias in the energy reconstruction is different for both algorithms. Monopod shows a nearly constant bias towards overestimated energies below the PeV region, whereas the bias of Credo rises with energy from less bias than Monopod to almost twice as much bias in $\Delta \log E$ around $1 \, \text{PeV}$. This disagreement will be investigated further in the next chapter (sec. 6.3). The rapid decrease in resolution for both algorithms at energies above $10 \, \text{PeV}$ is partially due to events at the detector boundary. In case of tighter containment, this decrease is weaker.

Directional Resolution

Reconstructing directional information from a cascade has been proven to be challenging [50]. Two angles are of interest: the zenith θ and the opening angle α between the true and reconstructed directions. Figure 6.8 shows the bias[2] in zenith $\langle \Delta \theta \rangle$, where $\Delta \theta = \theta_{reco} - \theta_{true}$ as well as the zenith resolution $\Delta_{\Delta \theta} = \langle |\theta_{reco} - \theta_{true}| \rangle$. At energies

---

[2]bias here: average of the histogrammed deviations. Not the parameter of a gaussian fit.
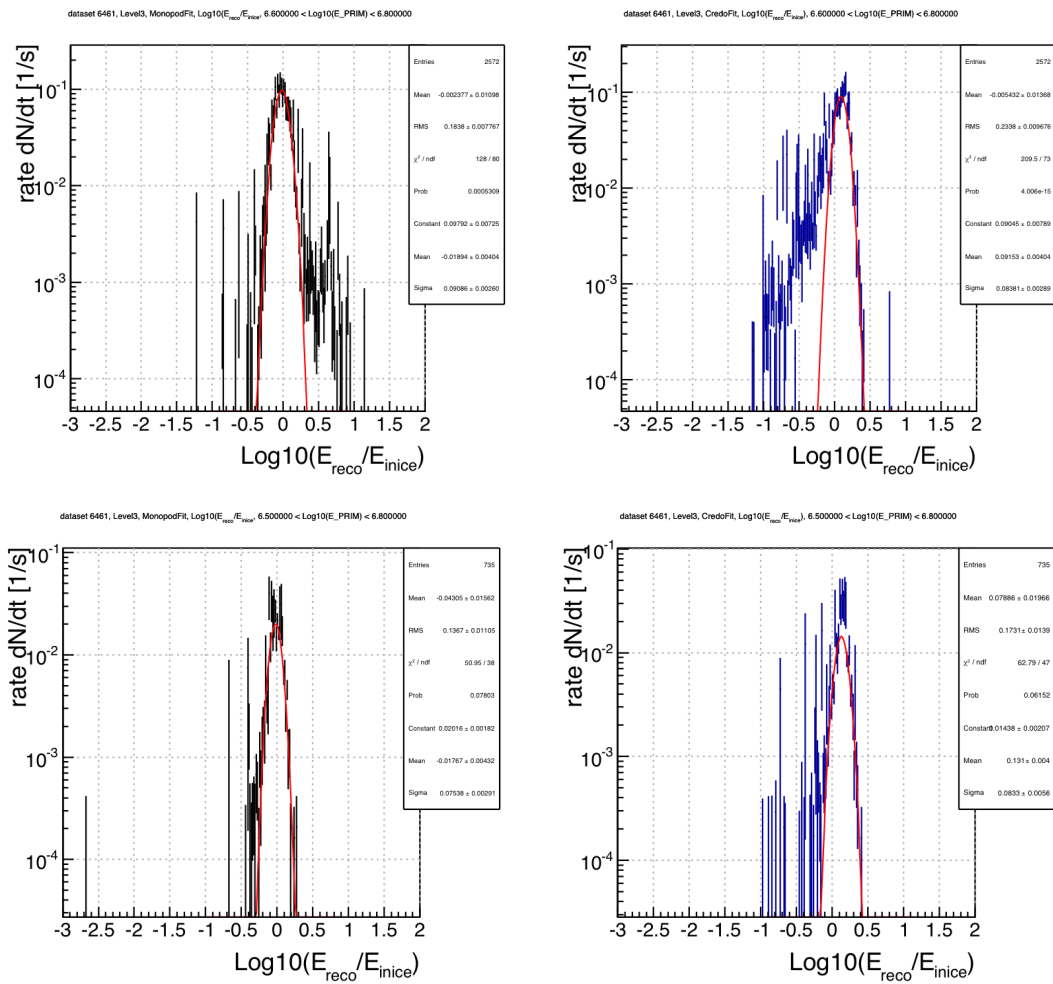
FIGURE 6.6: **Electron neutrino Monte Carlo (Level3):** The distributions of $\frac{\Delta E}{E}$ for weak containment and energy range $4.0\,\mathrm{PeV} < E_\nu < 6.3\,\mathrm{PeV}$ (top) as well as strong containment and energy range $3.2\,\mathrm{PeV} < E_\nu < 6.3\,\mathrm{PeV}$ (bottom): Monopod (left) and Credo (right).

FIGURE 6.7: **Electron neutrino Monte Carlo (Level3):** Resolution (right) and bias (left) of the reconstructed energy $\frac{\Delta E}{E}$ for Credo, Monopod and ACER. The bias and the resolution are obtained from fits to gaussian distributions in each energy bin. Events satisfy weak containment.

FIGURE 6.8: **Electron neutrino Monte Carlo (Level3):** Bias (left) and resolution (right) of the reconstructed zenith angle of Credo 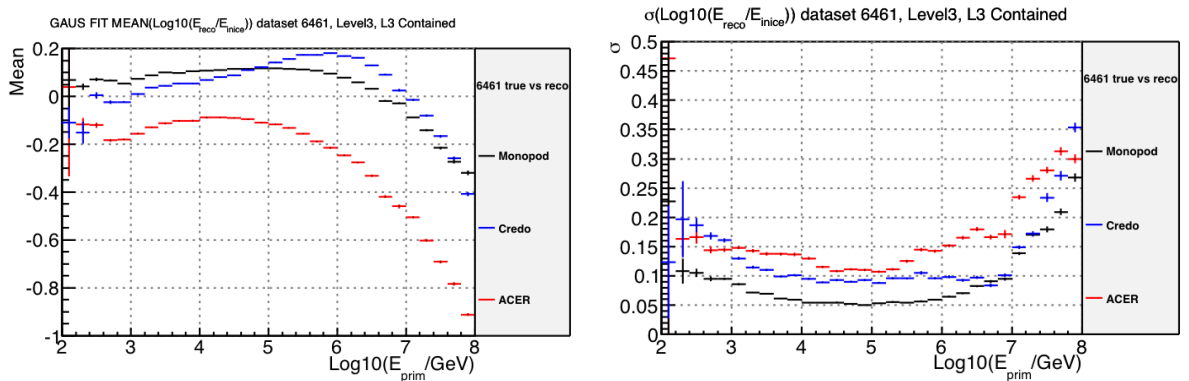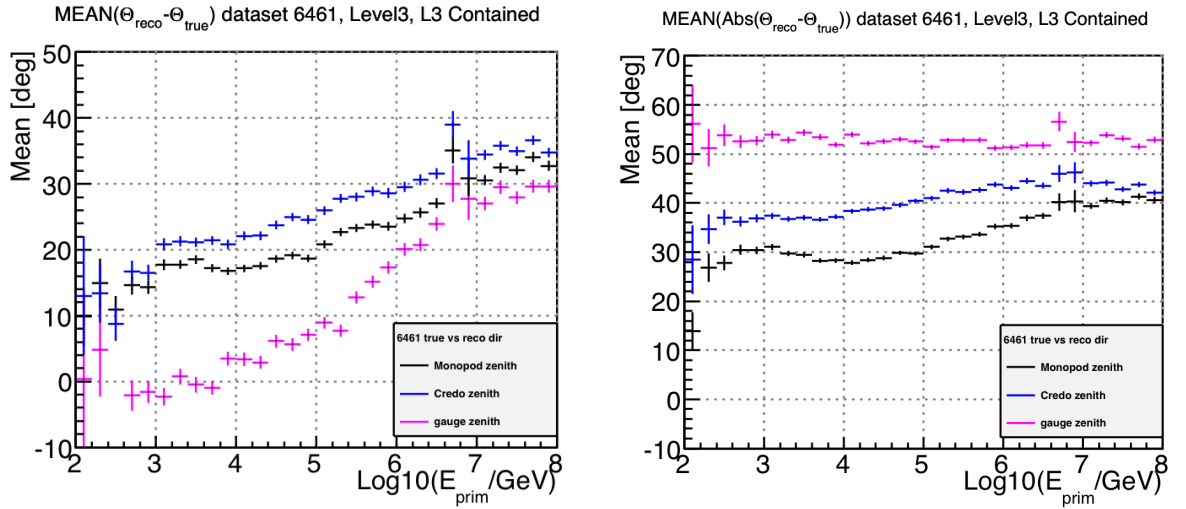and Monopod to be compared the case of the reconstructed zenith being sampled from a random number generator (gauge zenith); events satisfy weak containment

around the Glashow Resonance the resolution[3] in zenith is of the order of $\Delta_{\Delta\theta} \approx 40°$ for Monopod and $\Delta_{\Delta\theta} \approx 46°$ for Credo. The pink line shows the "resolution" in case of using a random number in the interval $\theta_{rnd} \in [0°, 180°[$ as reconstructed zenith. Hence only little information about the zenith can be extracted at Level3, since the resolution of both algorithms is only marginally better (by about $10°$) than the case of not having extracted any information (pink). Some caution is required when interpreting the bias shown in figure 6.8. Since with increasing energy the earth starts to absorb neutrinos until it becomes opaque at PeV energies, one expects a bias towards overestimating the zenith even in the case of random population of reconstructed zeniths. The pink curve visualizes that effect, rising from no bias at low energies to a bias of about $\sim 30°$ at highest energies.

The overall directional resolution in terms of the mean opening angle α between the true and reconstructed directions are summarized in figure 6.9. Over all the best directional resolution is achieved by Monopod with $\bar{\alpha} \approx 48°$ between $10\,\text{TeV}$ and $100\,\text{TeV}$. At energies around the Glashow Resonance resonance Monopod still gives the best result ($\bar{\alpha} \approx 60°$).

Summary

A summary is given by Table 6.1, showing the reconstruction performance at energies around the Glashow Resonance for three samples of dataset 6461, which differ only w.r.t. to the region within the detector of the events. Sample 1 shows the case of weak containment (Level3 Containment + additional cut on z_{true}, as discussed above), whereas

---

[3]resolution here: average absolute deviation of the reconstructed zenith from the true zenith
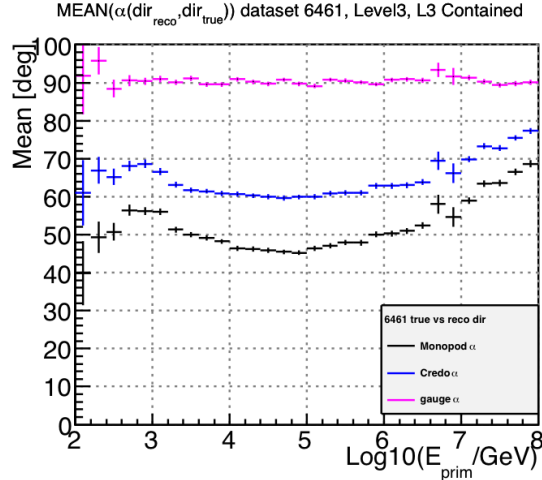
FIGURE 6.9: **Electron neutrino Monte Carlo (Level3):** The figures shows the mean opening angle $\bar{\alpha}$ between the true and reconstructed directions. "gauge zenith" refers to the case of the reconstructed direction being a random number; weak containment req.

Sample	$\mu_{\Delta x} \pm \sigma_{\Delta x}$ [m]	$\mu_{\Delta y} \pm \sigma_{\Delta y}$ [m]	$\mu_{\Delta z} \pm \sigma_{\Delta z}$ [m]	$\mu_{\Delta \log E} \pm \sigma_{\Delta \log E}$
Sample 1				
Monopod	1.7 ± 8.2	-0.8 ± 4.9[4]	-1.6 ± 4.2	0.03 ± 0.08
Credo	1.6 ± 8.6	0.7 ± 8.4	-1.8 ± 5.5	0.13 ± 0.09
Sample 2				
Monpod	-0.1 ± 7.3	-2.3 ± 8.7	-2.0 ± 3.9	-0.02 ± 0.07
Credo	-0.9 ± 8.8	-2.0 ± 7.0	-1.0 ± 4.5	0.13 ± 0.08
Sample 3				
Monopod	1.2 ± 6.9	-0.3 ± 7.8	-1.6 ± 3.1	0.00 ± 0.07
Credo	2.8 ± 11.3	-0.8 ± 8.1	-1.4 ± 7.8	0.15 ± 0.07

TABLE 6.1: **Electron neutrino Monte Carlo (Level3):** Bias and resolution of Credo and Monopod at the Glashow Resonance. The three samples: Sample 1: full detector with weak containment; Sample 2: above the dustlayer with strong containment; Sample 3: below the dust layer ($x_{true}^2 + y_{true}^2 < (350\,\mathrm{m})^2$ and $-400\,\mathrm{m} < z_{true} < -200\,\mathrm{m}$). Resolution and bias have been extracted from fits to gaussian distributions.

samples 2 and 3 are restricted to well contained events ($x_{true}^2 + y_{true}^2 < (350\,\mathrm{m})^2$) above ($50\,\mathrm{m} < z_{true} < 350\,\mathrm{m}$) and below ($-400\,\mathrm{m} < z_{true} < -200\,\mathrm{m}$) the dust layer. The results presented in this section are based on 1-iteration of both algorithms and supposedly improve with increasing number of iterations. However even in the case of having 32 iterations of Credo a median directional resolution of only $30°$ was found in previous studies [50]. Concerning the energy it is visible, that the energy estimates of Credo and Monopod differ at Level3. This disagreement will be addressed in the next section.

6.3 Credo and Monopod: A direct comparison at the Glashow resonance

In the last section it was found, that at Level3 of the cascade filter stream Monopod and Credo give largely different energy estimates, although relying on the same reconstruction method. By especially focusing on the Glashow resonance this shall be further investigated in this section. During those studies a problem with simulated Glashow resonance events was found in Monte Carlo dataset 6461, which will be discussed first.

6.3.1 Problem with Lepton Propagation in Dataset 6461 at Level2
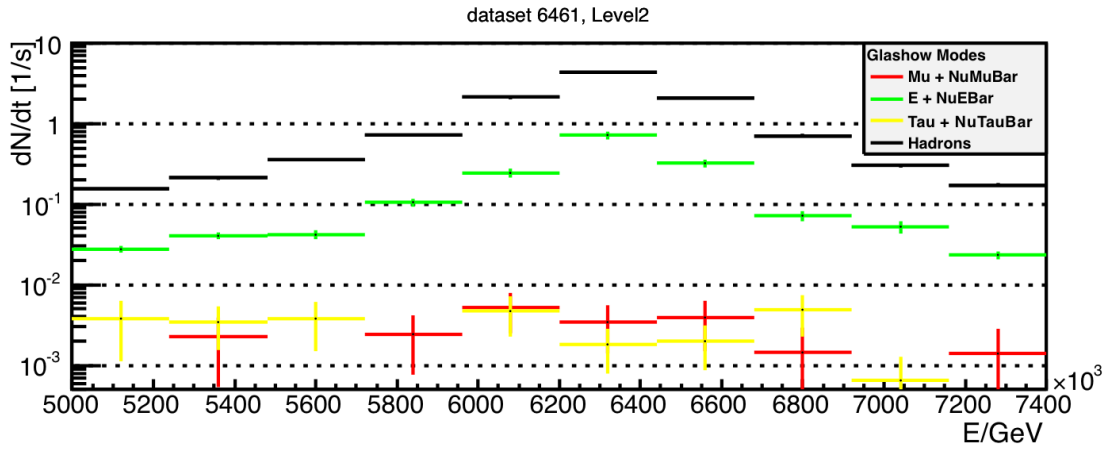
FIGURE 6.10: **Electron neutrino Monte Carlo (Level2):** Rates of the different Glashow Resonance modes in simulation for a neutrino flux expectation of $\frac{d\Phi}{dE} = 10^{-8} \left(\frac{E}{\text{GeV}}\right)^{-2} \text{GeV}^{-1}\text{cm}^{-2}\text{s}^{-1}\text{sr}^{-1}$ and $\Phi_{\nu_e}/\Phi_{\bar{\nu}_e} = 1$

In this work it was found, that the the muon and tau decay modes of the W^--boson are strongly suppressed compared to the electron mode, as can be seen in Figure 6.10. In order to investigate this problem, two additional datasets will be used throughout this discussion:

The "generated" Dataset

- dataset id: 7747 (unprocessed)

- geometry: IC79

- ice model: SPICEMie

- photon propagator: Photonics

---

[4]This value underestimates the respective resolution, due to a failed fit.

- generator: neutrino-generator (NuE)

- energy range: $10^{1.7}\,\mathrm{GeV} < E_\nu < 10^9\,\mathrm{GeV}$ with $E^{-\gamma}$ ($\gamma = 1$)

- angular range: $0° < \theta < 180°$

- software version: simulation.releases.V02-06-02

The "fixed" dataset 8788

- dataset id: 8788 (processed to Level2)

- geometry: IC86

- ice model: SPICEMie

- photon propagator: PPC

- generator: neutrino-generator (NuE)

- energy range: $10^{1.7}\,\mathrm{GeV} < E_\nu < 10^7\,\mathrm{GeV}$ with $E^{-\gamma}$ ($\gamma = 1$)

- angular range: $0° < \theta < 180°$

- software: simulation releases.V03-02-00 (contains lepton propagator bugfix)

According to the branching ratios (compare table 1.5) the rates in all leptonic modes should be the same, with small differences due to neutrino propagation through the earth. These differences would slightly enhance the contribution to the rate by the tau mode, compared to the other leptonic modes. At PeV energies the Earth is opaque for neutrinos, meaning that neutrinos traveling upwards ($\theta > 90°$, see Figure 3.2) would interact before reaching the detection volume, thus getting absorbed by the earth. The tau neutrino however is not absorbed, since a tau lepton produced in a CC interaction will decay to a tau neutrino (and others) before getting absorbed by the earth. As shown in Figure 6.10 there are up to two orders of magnitude difference between events associated with muon and tau production as compared to the electron mode. These missing contributions are also visible in the unweighted spectrum as a dip at the energy of interest in Figure 6.11. In order to understand the differences between the surviving contribution in the track like modes and the missing events, we plot the event distributions in the zenith-distance plane in Figure 6.12, with distance being the distance of the first resonant interaction vertex from the origin of the IceCube coordinate system. The upper plots in Figure 6.12 show the event distributions for all events, which are associated with the Glashow Resonance for the electron channel (left) and the muon channel (right). In the muon channel those events, which have had their first resonant
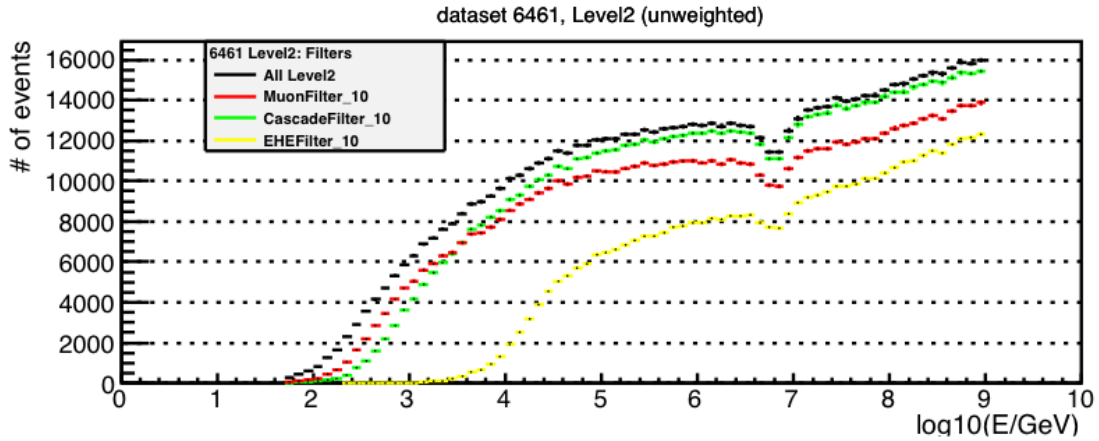
FIGURE 6.11: **Electron neutrino Monte Carlo (Level2):** E^{-1} primary neutrino energy spectrum at Level2 and the contributions from different IceCube filters. Missing events are shown as a suppression at the Glashow Resonance ($\log \frac{E_\nu}{\text{GeV}} \sim 6.8$).

FIGURE 6.12: **Electron neutrino Monte Carlo (Level2):** Zenith versus distance d for the electron channel (top left) and the muon channel (top right). In addition the influence of the requirement, that the last neutrino interaction was resonant, is shown (bottom).
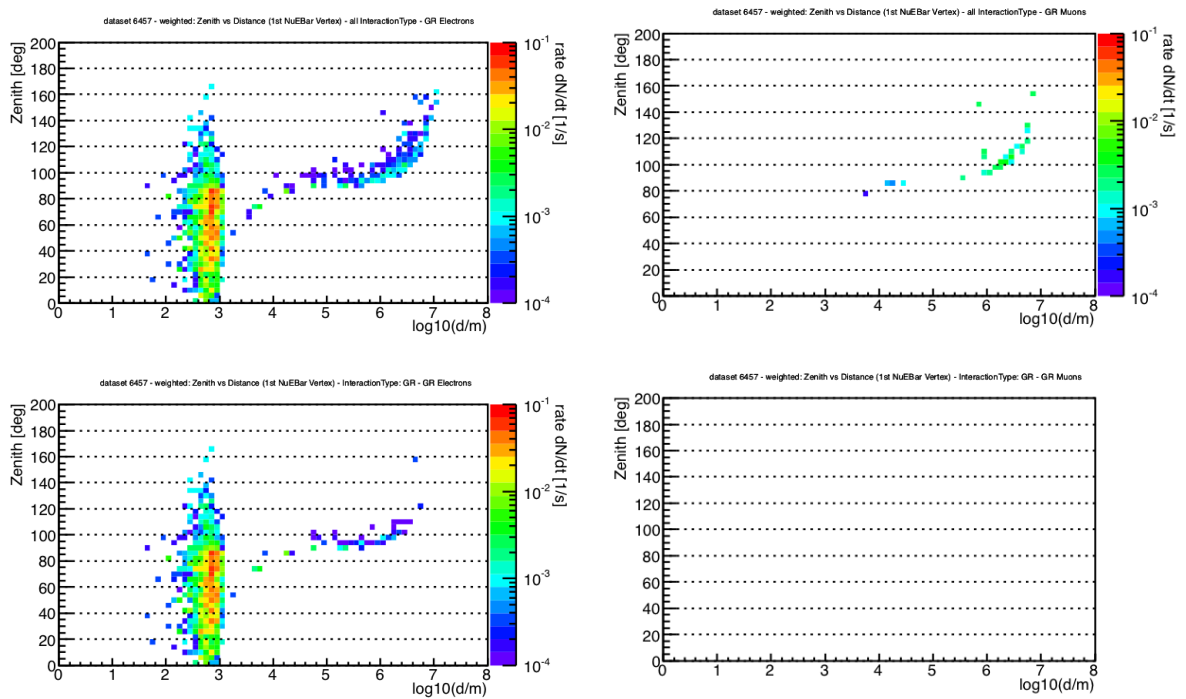
interaction vertex close to the detection Volume ($d < 1\,\mathrm{km}$) are missing. In the lower plots an additional cut regarding the interaction, which produced visible light in the detector, was applied. Only those events that produced visible light due to a resonant interaction are shown. In the muon channel 100% of the signal is missing after that selection. The same holds for the tau channel. Hence the only contribution to the track like modes in this dataset is due to those events, that produced muon and tau anti-neutrinos resonantly somewhere in the earth, which then produced a signal in the detector due to a subsequent CC or NC interaction.

In order to distinguish whether those events have been lost due to filtering and processing up to Level2 or if they have not been simulated within the simulation framework, a small unprocessed dataset (dataset 7747, based on same software and settings as used in Figure 6.12) of generated events was produced and subsequently processed using standard processing scripts (Version 11-02-00). The left plot in Figure 6.13 shows the zenith-distance plane for dataset 7747 (unprocessed) in the muon channel. By compar-
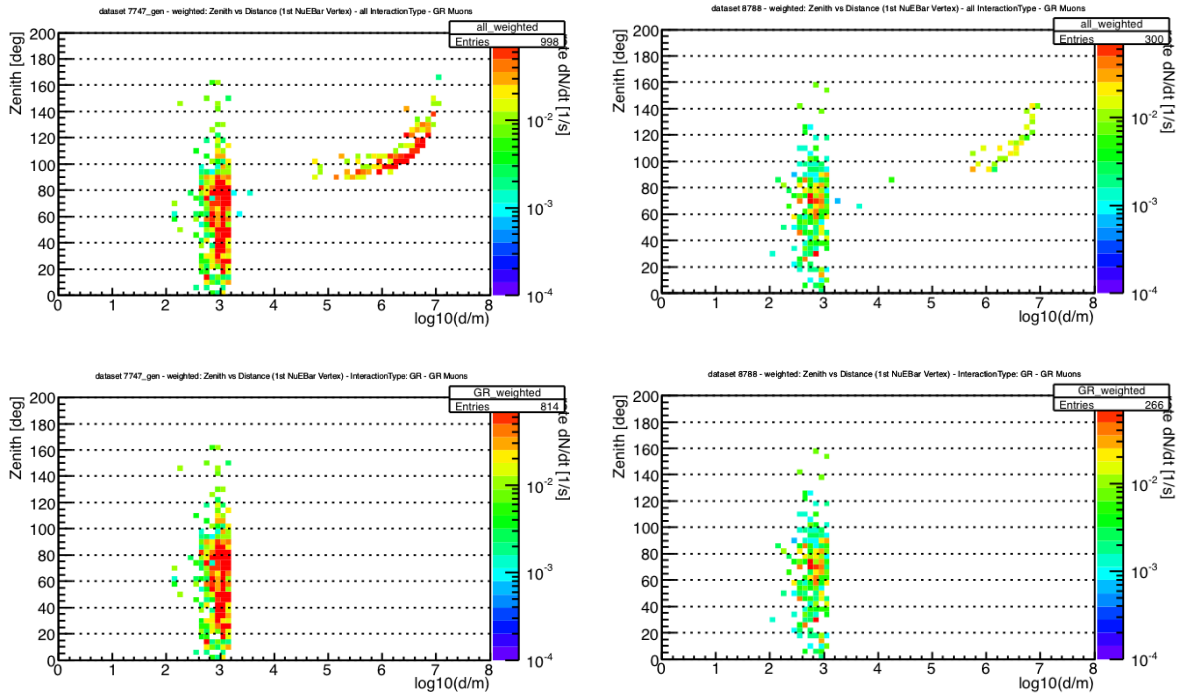
FIGURE 6.13: **Dataset 7747 unprocessed:** zenith versus distance d plane for the GR muon channel (left). **Dataset 8788 at Level2:** GR muon channel (right), simulated with IceSim 3.2. (w. lepton propagation bug fix).

ing to Figure 6.12 it becomes clear, that the neutrino generator used in the Monte Carlo simulation is not responsible for the loss. Instead it was found that the events are lost during the triggering, which means that these events miss their associated light output and hence are not kept. We passed this information to the simulation working group

in IceCube. It turned out that the secondary leptons (μ^- and τ^-) produced in the respective resonant interactions have not been propagated by the lepton simulation MMC (section 4). The small fraction of events associated with the Glashow resonance, which survived up to Level2 in dataset 6461, have been kept, because the hadronic cascade in the subsequent CC/NC interaction produced by itself sufficient light to trigger the detector.

In the release version 3.2. of the IceCube simulation software IceSim, this bug has partially been fixed. The right plot in figure 6.13 shows the distribution of muon events associated with the Glashow Resonance after Level2 processing of dataset 8788, which was produced after the release of IceSim 3.2. with the bug fix mentioned above. The Level 2 distribution of dataset 8788 (right) follows the unprocessed distribution of dataset 7477 for that mode (left), with differences in normalization being due to triggering. However the tau mode is still affected by this problem, as shown in Figure 6.14. Why the tau channel is still suppressed after the release of IceSim 3.2., is currently under investigation in the IceCube simulation working group.
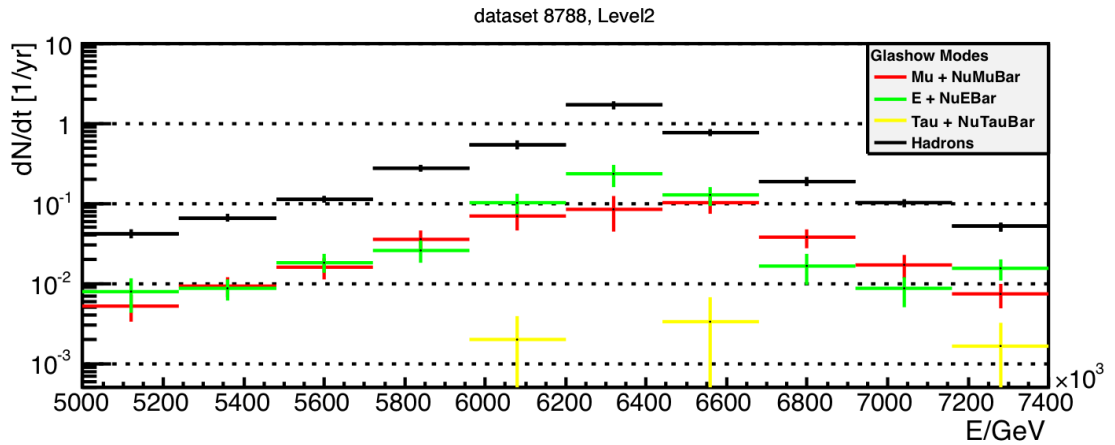
FIGURE 6.14: **Dataset 8788 at Level2:** Rates of the different Glashow Resonance modes in simulation after the release of IceSim 3.2. for a neutrino flux expectation of $\frac{d\Phi}{dE} = 10^{-8} \left(\frac{E}{\text{GeV}} \right)^{-2} \text{GeV}^{-1}\text{cm}^{-2}\text{s}^{-1}\text{sr}^{-1}$ and $\Phi_{\nu_e}/\Phi_{\bar{\nu}_e} = 1$

6.3.2 The Event Samples

The issue discussed above, does not influence the Glashow resonance modes with hadronic or electron (and electron anti neutrino) final states. In addition the hadronic Glashow resonance mode does not produce neutrinos, which would invisibly carry away energy, thus creating cascades with a well-defined light yield. Furthermore this channel dominates the Glashow Resonance at 6.3 PeV. Hence the following study, addressing the observed disagreement in energy as well as the general reconstruction performance at

the Glashow resonance, is based on those cascades only. In section 6.2 it was shown that partially contained cascades impose a challenge for reconstruction algorithms. By requiring a strong containment of the sample the corresponding non-gaussian tails vanished. To make sure, that no light leaves the detection volume those containment cuts have been tightened further. The samples, subsequently being used, possess the following properties:

- 1000 hadronic cascades via Glashow Resonance

- dataset 6461 at Level2[5]

- $1\,\mathrm{PeV} < E_{prim} < 10\,\mathrm{PeV}$ with E^{-1} spectrum

- $x_{true}^2 + y_{true}^2 < (250\,\mathrm{m})^2$

- **Sample A (above the dustlayer):** $100\,\mathrm{m} < z_{true} < 300\,\mathrm{m}$

- **Sample B (below the dustlayer):** $-400\,\mathrm{m} < z_{true} < -200\,\mathrm{m}$

The study will focus on the sample A, since the reconstruction performance above the dust layer typically is worse compared to the performance below the dust layer, where the clearest ice is present. Sample B will be used to validate the results, we obtained based on investigating Sample A.

6.3.3   Credo and Monopod: Corrections 1 (same pulses and ice model)

Interpreting the difference in the energy estimates provided by Credo and Monopod found in section 6.2 is problematic, since at Level3 those algorithms have been run using different input (i.e. different seed and differently processed light pulses). Hence for further investigation the effect of the algorithm has to be disentangled from the influence of having different input. Thus in this section, both algorithms will be used to reconstruct the event sample based on the same settings as were previously applied at Level 3 except that the same input will be used for both algorithms. This is summarized as follows:

- pulses: OfflinePulses

- ice model: SPICE1

- photonics interface: PhotoSplines

---

[5]Level2 was chosen to increase the statistics to 1000 cascades with the described properties.

- seed: Cscd-llh (vertex), ToI (direction), ACER (energy)

- 1-iteration

- Credo with "IC40-Corrections" (same as at Level3)

- Monopod with constant scaling of Photonics predictions ($\xi = 0.58$, same as at Level3)

- Software: IceRec.release.V04-01-02
  including Credo.release.V00-02-02 and Millipede.release.V01-01-00

It was decided to use calibrated pulses (OfflinePulses), that have not been cleaned from noise, since both algorithms consider noise contributions to the measured charge, when likelihood values are computed. PhotoSpline tables are used to avoid problems, which may arise from the coarse binning and the respective possible artifacts of the linear interpolation, used in PhotoRec tables (compare sec 4.4). These settings will subsequently be referred to as C1R for Credo and M1R for Monopod.

The distributions of $\frac{\Delta E}{E} = \frac{E_{reco} - E_{true}}{E_{true}}$ (energy), $\Delta \theta = \theta_{reco} - \theta_{true}$ (zenith), $\Delta x = x_{reco} - x_{true}$ and $\Delta z = z_{reco} - z_{true}$ (vertex) as obtained with C1R and M1R are shown in Figure 6.15 for sample A. The corresponding resolutions have been obtained from fits to Gaussian distributions, except for the zenith distribution, which due to geometry is not expected to follow a Gaussian distribution.

As shown in Figure 6.15, when relying on the same input, Credo and Monopod still give different estimates of the energy distribution $\frac{\Delta E}{E} = \frac{E_{reco} - E_{true}}{E_{true}}$. Whereas Credo on average overestimates the cascade energy by about 21 %, Monopod underestimates the cascade energy by about -8 %. In addition Monopod shows a non-Gaussian feature at lower reconstructed energies. Hence Monopod divides this sample, which should contain very similar cascades, into two regions, a main peak for which the under estimation of -8 % holds and a side peak towards even lower reconstructed energies. Credo determines the x coordinate to within $\sigma_{\Delta x} \approx 5.2$ m, while being unbiased. However a contribution of non-gaussian tails are present. The Monopod result is slightly worse, showing a resolution of $\sigma_{\Delta x} \approx 7.8$ m without bias. The performance in y is similar. Due to the denser instrumentation along z, a better resolution of 3.7 m (Credo) and 5.6 m (Monopod) is achieved. Both algorithms show the same zenith resolution of $\theta_{RMS} \approx 40°$. The results for all parameters are listed in Table 6.2. The side peak in the Monopod energy distribution was not observed in section 6.2, when Monopod was using a more accurate seed, provided by Credo. We checked, whether this feature depends on the seed by using

---

[6]These values only apply for the main peak of the corresponding distribution. A significant contribution is due to events, which form a second peak towards underestimated energies.
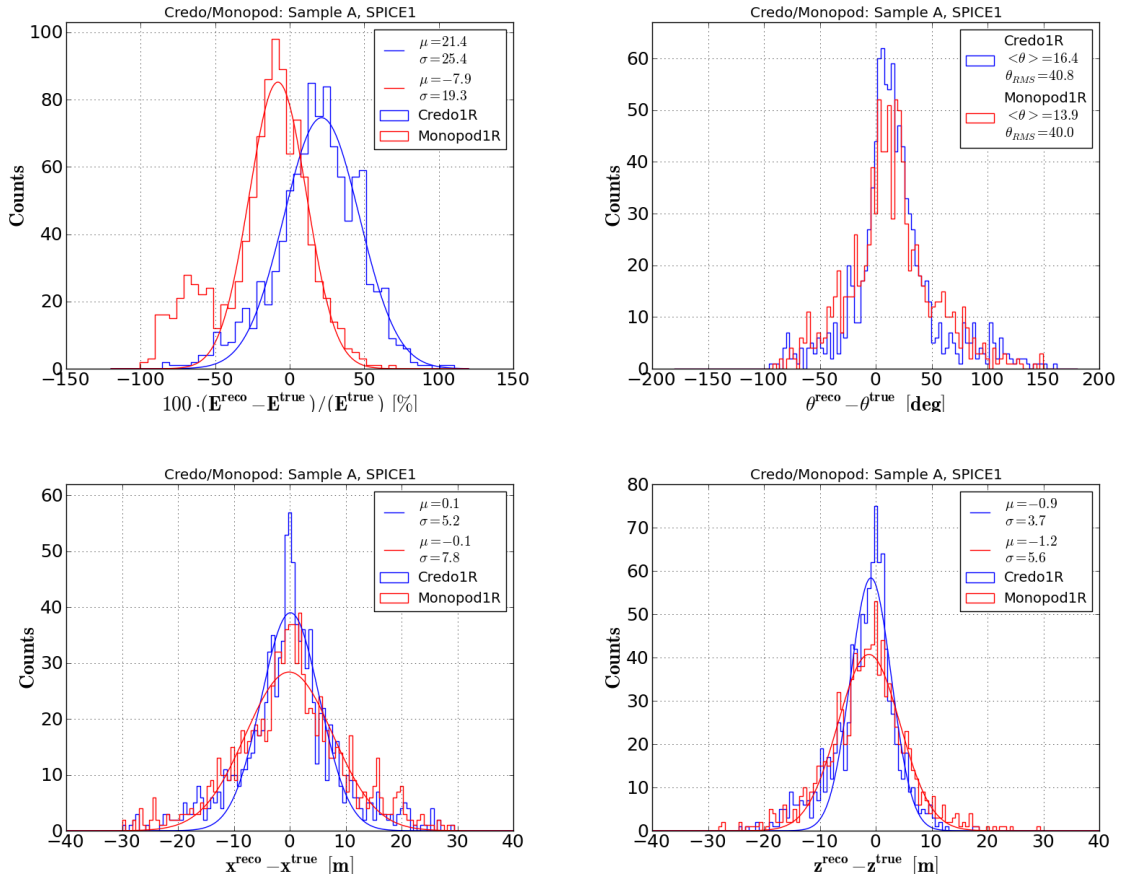
FIGURE 6.15: **Sample A:** Reconstruction results of M1R and C1R for energy $\frac{\Delta E}{E}$ (top left), zenith $\Delta\theta$ (top right), Δx (bottom left) and Δz (bottom right)

$\mu_{\Delta x} \pm \sigma_{\Delta x}$ [m]	$\mu_{\Delta y} \pm \sigma_{\Delta y}$ [m]	$\mu_{\Delta z} \pm \sigma_{\Delta z}$ [m]	$\mu_{\frac{\Delta E}{E}} \pm \sigma_{\frac{\Delta E}{E}}$	$\overline{\Delta\theta} \pm RMS_{\Delta\Theta}$
-0.1 ± 7.8	0.0 ± 7.3	-1.2 ± 5.6	$(-8 \pm 19)\,\%$[6]	$(13 \pm 40)^\circ$
0.1 ± 5.2	0.0 ± 4.6	-0.9 ± 3.7	$(21 \pm 25)\,\%$	$(16 \pm 41)^\circ$

TABLE 6.2: Sample A: Summary of the bias and resolution for M1R (1st row) and C1R (2nd row)

the result of C1R obtained in this section as seed for 1-iteration of Monopod (M1C1) and 1-iteration of Credo (C1C1), while keeping all other settings as before.

As shown in Figure 6.16 the Monopod side peak in the energy vanished, when being seeded with C1R, and the distribution becomes gaussian. Hence we interpret this as Monopod being more sensitive to its seed. In addition after using the more precise seed, both algorithms show similar distributions of the vertex coordinates. The corresponding resolutions slightly improved compared to the C1R result (shown in 6.15) by about $\sim 0.5\,\text{m}$ in all coordinates. Despite the vanishing side peak in case of M1C1 the

$\mu_{\Delta x} \pm \sigma_{\Delta x}$ [m]	$\mu_{\Delta y} \pm \sigma_{\Delta y}$ [m]	$\mu_{\Delta z} \pm \sigma_{\Delta z}$ [m]	$\mu_{\frac{\Delta E}{E}} \pm \sigma_{\frac{\Delta E}{E}}$	$\overline{\Delta\theta} \pm RMS_{\Delta\Theta}$
M1C1				
-0.1 ± 5.1	0.0 ± 4.2	-0.8 ± 3.5	$(-13 \pm 19)\,\%$	$(15 \pm 36)^{\circ}$
C1C1				
0.2 ± 4.6	0.1 ± 4.2	-0.7 ± 3.2	$(21 \pm 25)\,\%$	$(16 \pm 39)^{\circ}$

TABLE 6.3: Sample A: Summary of the bias and resolution for M1C1 and C1C1

energy results of M1C1 and C1C1 remain unchanged when compared to M1R and C1R. Due to the improved seed, Monopod now shows a slightly better zenith performance ($\theta_{RMS} = 36.2°$) than Credo ($\theta_{RMS} = 38.7°$). This is summarized in Table 6.3. Despite
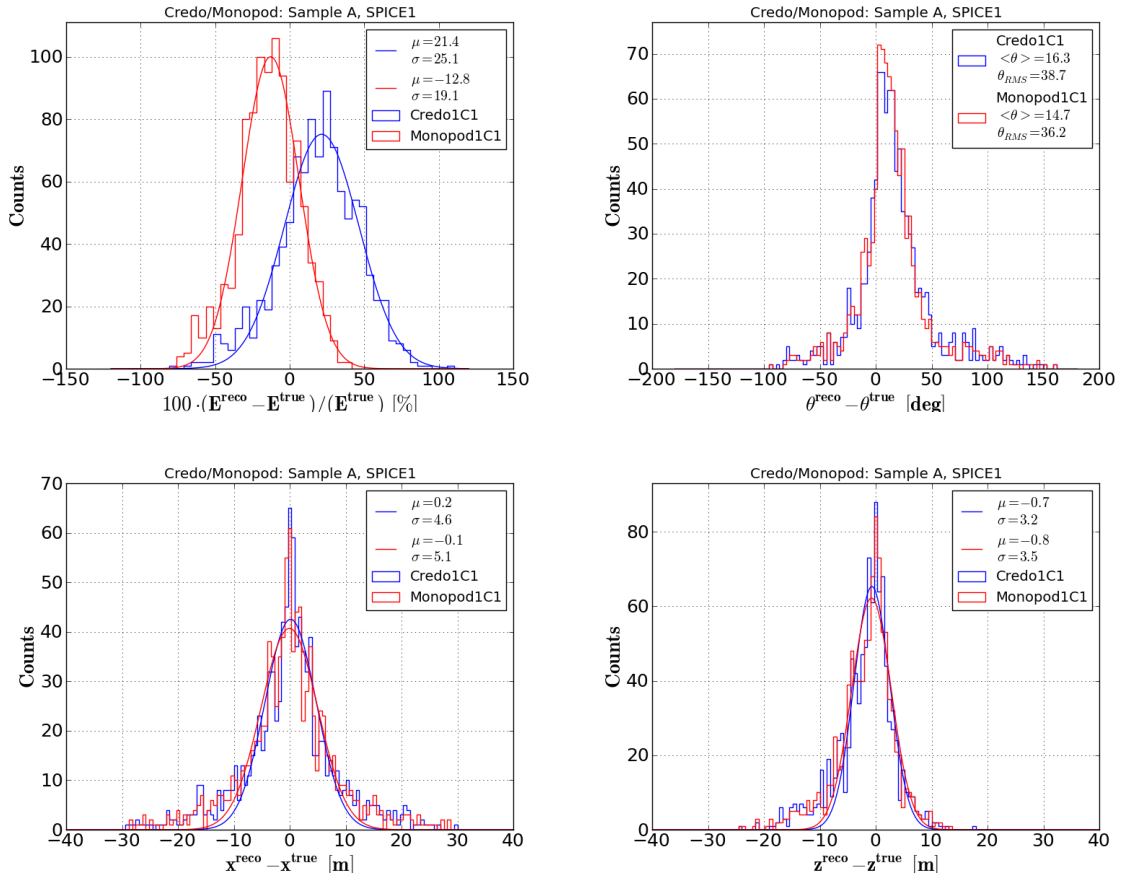
FIGURE 6.16: **Sample A:** Reconstruction results of M1C1 and C1C1 for energy $\frac{\Delta E}{E}$ (top left), zenith $\Delta\theta$ (top right), Δx (bottom left) and Δz (bottom right); Seed: C1R

improving the vertex resolution, having a better seed did not resolve the presence of non-Gaussian tails in the vertex distributions. Since both algorithms show Gaussian energy distributions, the used settings will be kept, while only the photonics corrections in both algorithms will be changed to study the influence of those corrections on the visible disagreement in the energy estimates.

6.3.4   Credo and Monopod: Corrections 2 (photonics scaling)

The number of photons created by a cascade scales linear with the cascade energy. Credo and Monopod apply corrections to the predicted Photonics amplitudes (sec. 5.2), which thus have a direct influence on the reconstructed energy. The corrections, used in Credo, have been introduced in 2008/2009 (40-string detector configuration) [50]. By comparing the expected and observed charge in each DOM, it was found in [50] that Photonics on average over-predicted the light yield in a given DOM for unknown reasons. This discrepancy has been parametrized and the parametrization was used to lower the photonics prediction before minimizing the Credo likelihood (for details see [50]). Due to advances in calibration since then, those corrections should be redundant. Thus from now on, they have been removed for the subsequent studies in this work. However as discussed below, other corrections are still necessary.

The detector response, except for the DOM acceptance and efficiency, is not reflected in the photonics predictions. First of all the charge response function of the IceCube PMT (sec. 3) yields a mean single photon charge of $< q_{spe} >= 0.85\,q_{spe}$. Hence on average the observed charge will be lower than the Photonics predicted light yield by 85%. In addition so-called cable shadowing may reduce the expected number of photons by another 10%. Thus the DOM efficiency ϵ_0 would have to be corrected by a factor of $\xi = 0.9 \cdot 0.85$ to yield an "effective" DOM efficiency $\epsilon_{eff} = \xi \cdot \epsilon_0$. Since the Photonics simulation uses the uncorrected DOM efficiency ϵ_0 to derive the predicted amplitude A_0, the predicted amplitude needs to be corrected accordingly: $A_{eff} = \xi \cdot A_0$. In the case of Monopod this was already done [77].

Instead of $\xi = 0.58$ (Monopod) and IC40-Corrections (Credo), which were used in the IceCube Cascade Level3 processing, yielding a large disagreement in the energy estimate, as seen in Figure 6.16), the constant correction $\xi = 0.9 \cdot 0.85 \approx 0.77$ will now be applied in both, M1C1 as well as C1C1. As shown in Figure 6.17 the large disagreement vanished. Furthermore all other reconstructed parameters (vertex and zenith) agree very well, as shown in table 6.4 based on the results of the respective gaussian fits (sample A). However two issues remain. First the above mentioned correction yields underestimated energies for both algorithms by about $-30\,\%$. Second the distributions of the vertex residuals show large non-gaussian tails towards miss reconstructed values, indicating unstable results.
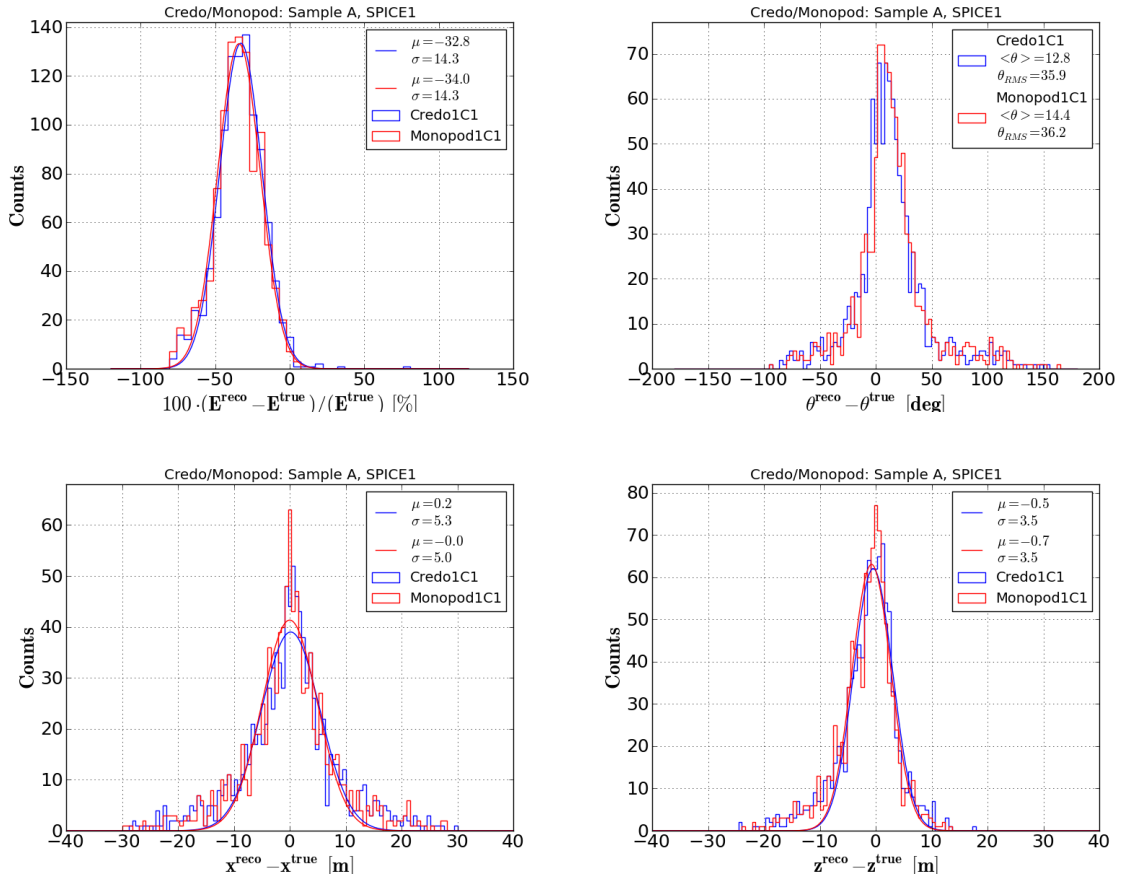
FIGURE 6.17: **Sample A:** Reconstruction results of M1C1 and C1C1 for energy $\frac{\Delta E}{E}$ (top left), zenith $\Delta\theta$ (top right), Δx (bottom left) and Δz (bottom right); Same settings as in Figure 6.16 but common photonics correction $\xi \approx 0.77$ applied in both algorithms.

$\mu_{\Delta x} \pm \sigma_{\Delta x}$ [m]	$\mu_{\Delta y} \pm \sigma_{\Delta y}$ [m]	$\mu_{\Delta z} \pm \sigma_{\Delta z}$ [m]	$\mu_{\frac{\Delta E}{E}} \pm \sigma_{\frac{\Delta E}{E}}$	$\overline{\Delta\theta} \pm RMS_{\Delta\Theta}$
M1C1				
0.0 ± 5.0	-0.1 ± 4.1	-0.7 ± 3.5	$(-34 \pm 14)\,\%$	$(14 \pm 36)^{\circ}$
C1C1				
0.2 ± 5.3	0.1 ± 4.8	-0.5 ± 3.5	$(-33 \pm 14)\,\%$	$(13 \pm 36)^{\circ}$

TABLE 6.4: **Sample A:** Resolution and Bias for M1C1 and C1C1; Same settings as in table 6.3, but common photonics correction $\xi = 0.77$ applied in both algorithms

We have shown that C1C1 and M1C1 show similar reconstruction performance on Sample A, when feeding the same input to Credo and Monopod, while applying the same corrections $\xi = 0.77$ to the photonics predicted amplitudes. This also holds for Sample B, see Table 6.5. Compared to Sample A (Table 6.4) the resolutions are up to a factor of two better, due to the clear ice below the dust layer. The energy however shows the same underestimation of $\mu_{\frac{\Delta E}{E}} \approx -30\%$. Since Monopod and Credo were found to show consistent results for the correction $\xi = 0.77$, this setting will subsequently be used

$\mu_{\Delta x} \pm \sigma_{\Delta x}$ [m]	$\mu_{\Delta y} \pm \sigma_{\Delta y}$ [m]	$\mu_{\Delta z} \pm \sigma_{\Delta z}$ [m]	$\mu_{\frac{\Delta E}{E}} \pm \sigma_{\frac{\Delta E}{E}}$	$\overline{\Delta\theta} \pm RMS_{\Delta\Theta}$
M1C1				
0.0 ± 2.6	0.0 ± 2.4	-0.3 ± 1.9	$(-32 \pm 14)\,\%$	$(4 \pm 23)°$
C1C1				
0.0 ± 2.5	0.0 ± 2.7	-0.2 ± 2.0	$(-31 \pm 14)\,\%$	$(4 \pm 21)°$

TABLE 6.5: **Sample B:** Resolution and Bias for M1C1 and C1C1; $\xi = 0.77$

(unless mentioned otherwise).

6.3.5 Credo and Monopod: Event-wise comparison

It is interesting to investigate how both algorithms compare on an event by event basis. The residuals $\frac{\Delta E}{E}$ and Δx_i will be redefined such that they measure the deviation between both algorithms: $\frac{\Delta E}{E} = 100 \cdot \frac{E_{M1C1} - E_{C1C1}}{E_{C1C1}}$, with E_{M1C1} and E_{C1C1} being the reconstructed Monopod and Credo energies respectively. The same will be used for the vertex $\Delta x_i = x_i^{M1C1} - x_i^{C1C1}$. Hence the comparison becomes independent of the absolute energy. These residuals are plotted in Figure 6.18 for sample A and sample B. Both
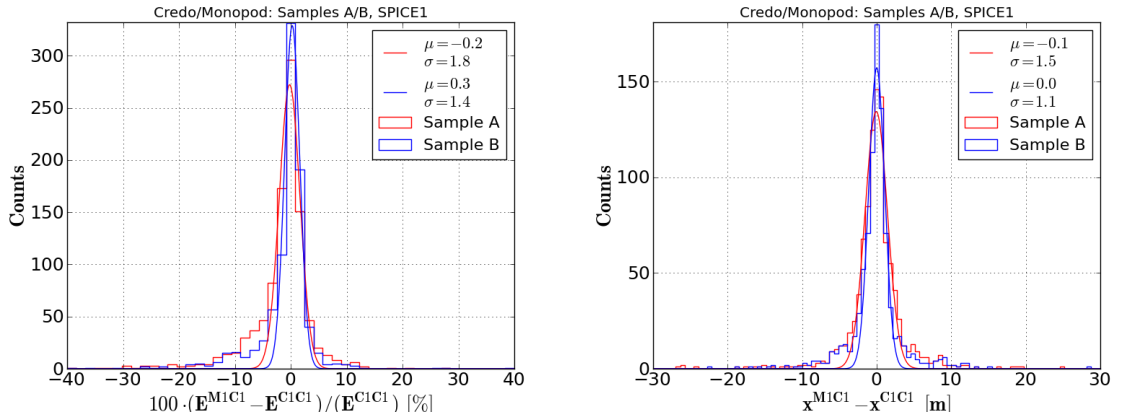

FIGURE 6.18: **Samples A and B:** Event per Event comparison of M1C1 and C1C1: $\frac{\Delta E}{E} = 100 \cdot \frac{E_{M1C1} - E_{C1C1}}{E_{C1C1}}$ (left) and $\Delta x_i = x_i^{M1C1} - x_i^{C1C1}$ (right); The respective resolutions can be found in 6.4 (Sample A) and 6.5 (Sample B)

algorithms agree within $\sigma_{\frac{\Delta E}{E}} \approx 2\%$ in terms of energy for most of the events. This is in agreement within the resolution w.r.t to the true energy of $\sigma_{\frac{\Delta E}{E}\,true} \approx 14\%$, as shown in tables 6.4 (Sample A) and 6.5 (Sample B). The same holds for the vertex position, with one exception. The deviation between both algorithms $\sigma_{\Delta x} \approx 1.5\,\mathrm{m}$ is not significantly smaller than the respective resolution w.r.t to x_{true} of $\sigma_{\Delta x}^{true} \approx 2.5\,\mathrm{m}$.

The presence of non gaussian tails in both histograms of figure 6.18 reveals a contribution of events for which the residuals $\sigma_{\frac{\Delta E}{E}}$ and $\sigma_{\Delta x}$ exceed the resolutions $\sigma_{\frac{\Delta E}{E}\,true}$

and $\sigma_{\Delta x}^{true}$. This discrepancy can be explained with the fit results being unstable for this class of events. This will be shown by applying the following seeding scheme (visualized in fig. 6.19): A first iteration will be performed using Credo (C1R) and Monopod
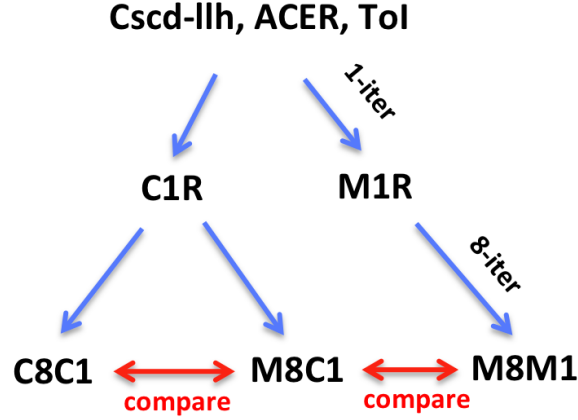

FIGURE 6.19: Seeding scheme used to investigate the tails in the distributions of figure 6.18.

(M1R) seeded with Cscd-llh, ACER and ToI, as in sec. 6.3.3. Next a more precise result will be obtained using 8-iterations of Credo (C8C1), seeded with the result of the C1R. In addition 8-iterations of Monopod, M8C1 and M8M1, will be seeded with C1R and M1R respectively. This allows to compare deviations between M8C1 and C8C1 to the deviations between two Monopod results (M8C1 and M8M1), which only differ w.r.t their seed. Thus this will qualitatively provide an estimate of the instabilities due to minimization and seeding (i.e. paths through the likelihood during minimization). The

FIGURE 6.20: **Sample A:** (Left) distance d between the reconstructed vertices of M8C1 and C8C1 versus the relative difference in the e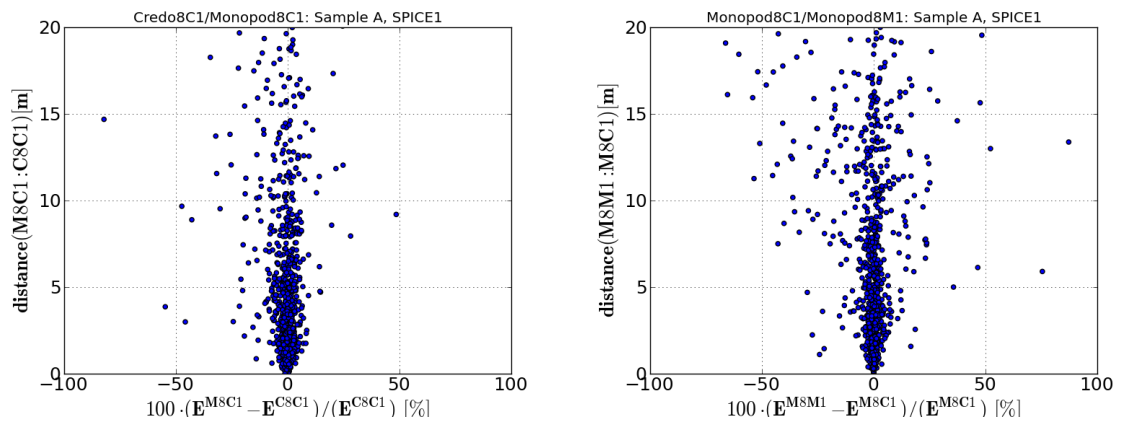nergy estimate $\frac{\Delta E}{E} = 100 \cdot \frac{E_{M8C1} - E_{C8C1}}{E_{C8C1}}$; (Right) distance d between the reconstructed vertices of M8C1 and M8M1 versus the relative difference in the energy estimate $\frac{\Delta E}{E} = 100 \cdot \frac{E_{M8M1} - E_{M8C1}}{E_{M8C1}}$

results are presented in Figure 6.20, showing the distance between both reconstructed

vertices versus the fractional difference between the energy estimators in case of Sample A. The main fraction of the events shown in both 2D plots in Figure 6.20 agree within $\frac{\Delta E}{E} \approx 2\%$ and $\sigma_{\Delta x_i} \approx 2\,\text{m}$. The tails, discussed above, show up as a contribution of events which wildly scatters in this plane. However as one can see, the scattering in case of a comparison between the results of M8C1 and C8C1 (left) is comparable (or slightly less) than the scattering in case of a comparison between M8M1 to M8C1 (right). The conclusion is that the observed tails of events, for which Monopod and Credo disagree, can be explained with the algorithms being sensitive to the seeds for those events. Thus for those events the reconstruction result is not stable against changes of the initial conditions. Hence we have shown that Credo and Monopod give consistent reconstruction results, when using the same set of settings, as expected from the fact, that both are using the same likelihood description.

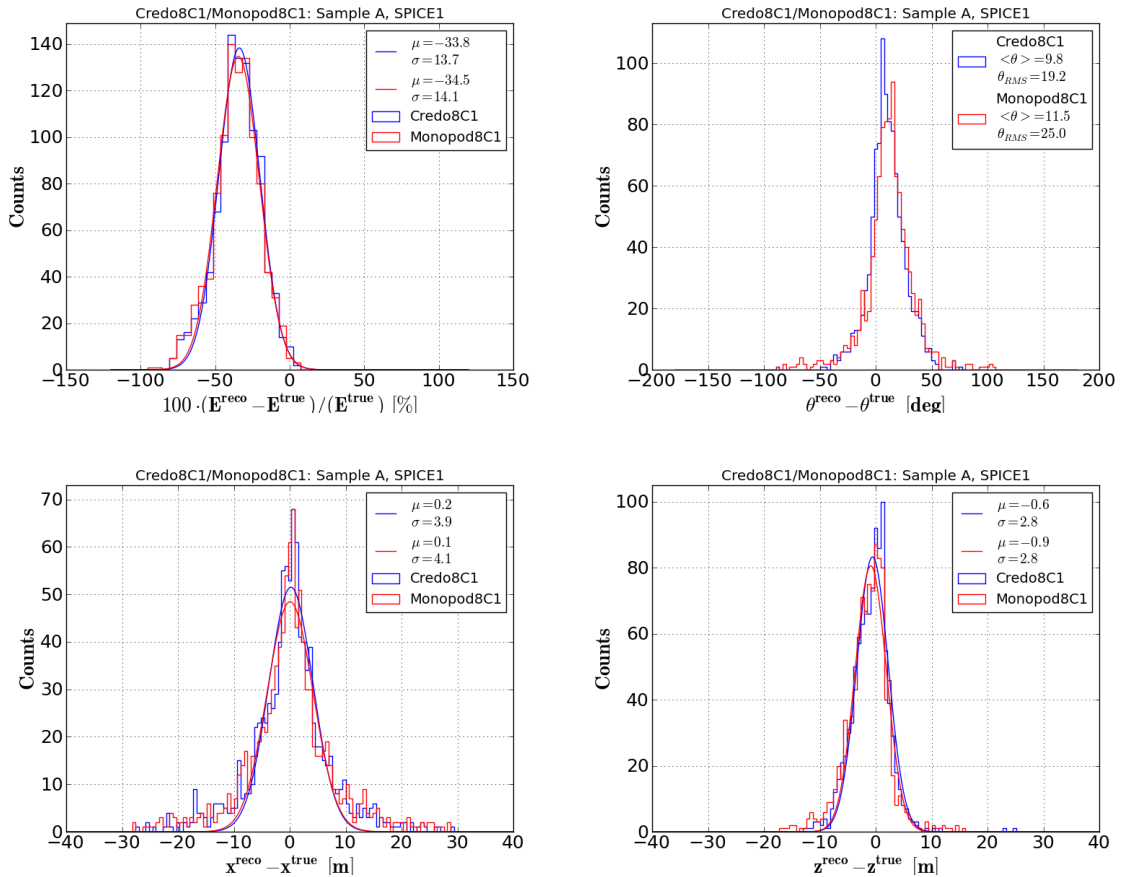### 6.3.6 Credo and Monopod: Increasing the number of iterations

FIGURE 6.21: **Sample A:** Reconstruction results of M8C1 and C8C1 for energy $\frac{\Delta E}{E}$ (top left), zenith $\Delta\theta$ (top right), Δx (bottom left) and Δz (bottom right); common photonics correction $\xi = 0.77$ applied in both

By comparing the reconstruction results obtained by M8C1 and C8C1 (sec. 6.3.5 to the results of C1C1 and M1C1 (sec. 6.3.4) it is possible to investigate by how much the results improve when more iterations are used. Hence from now on the following definitions apply:

$$\frac{\Delta E}{E} = 100 \cdot \frac{E_{reco} - E_{true}}{E_{true}} \tag{6.1}$$

$$\Delta\theta = \theta_{reco} - \theta_{true} \tag{6.2}$$

$$\Delta x_i = x_i^{reco} - x_i^{true} \tag{6.3}$$

The corresponding distributions for M8C1 and C8C1 based on Sample A are shown in Figure 6.21. Increasing the number of iterations from one to eight iterations did not change the energy distribution. Hence the energy resolution remains at $\frac{\Delta E}{E} = 14\%$. The vertex resolution improved by about $1\,\text{m}$ in all components. The strongest effect is seen in the reconstructed zenith with a change from $\theta_{RMS} = 35.9°$ (C1C1) to $\theta_{RMS} = 19.2°$ (C8C1) and from $\theta_{RMS} = 36.2°$ (M1C1) to $\theta_{RMS} = 25.0°$ (M8C1). However additional iterations did not resolve the issue of having non-gaussian contributions in the vertex distributions. The results for sample A are summarized in Table 6.6.

That the observations made for Sample A also hold for Sample B, is shown in Table

$\mu_{\Delta x} \pm \sigma_{\Delta x}$ [m]	$\mu_{\Delta y} \pm \sigma_{\Delta y}$ [m]	$\mu_{\Delta z} \pm \sigma_{\Delta z}$ [m]	$\mu_{\frac{\Delta E}{E}} \pm \sigma_{\frac{\Delta E}{E}}$	$\overline{\Delta\theta} \pm RMS_{\Delta\Theta}$
M8C1				
0.1 ± 4.1	0.1 ± 4.1	-0.9 ± 2.8	$(-35 \pm 14)\,\%$	$(12 \pm 25)°$
C8C1				
0.2 ± 3.9	0.2 ± 3.9	-0.6 ± 2.8	$(-34 \pm 14)\,\%$	$(10 \pm 19)°$

TABLE 6.6: **Sample A**: Resolution and bias for M8C1 and C8C1; $\xi = 0.77$

6.7 for C1R and C4C1 (4-iterations). The energy is again stable against increasing the number of iterations, while mainly the reconstructed zenith improves. In contrast

$\mu_{\Delta x} \pm \sigma_{\Delta x}$ [m]	$\mu_{\Delta y} \pm \sigma_{\Delta y}$ [m]	$\mu_{\Delta z} \pm \sigma_{\Delta z}$ [m]	$\mu_{\frac{\Delta E}{E}} \pm \sigma_{\frac{\Delta E}{E}}$	$\overline{\Delta\theta} \pm RMS_{\Delta\Theta}$
C1R				
0.0 ± 2.7	0.2 ± 2.7	-0.5 ± 2.4	$(-31 \pm 14)\,\%$	$(6 \pm 27)°$
C4C1				
0.0 ± 2.3	0.0 ± 2.4	-0.3 ± 1.8	$(-32 \pm 14)\,\%$	$(3 \pm 15)°$

TABLE 6.7: **Sample B**: Resolution and bias for C4C1 and C1R; $\xi = 0.77$

to the zenith the energy resolution does not improve further with increasing number of iterations. This will have implications on the strategy to select candidate events

in a search for the Glashow Resonance, with the cascade energy being the main cut variable. Since the best performance is already achieved after one iteration, a stable energy estimate can be achieved, without spending additional CPU resources on more iterations. In that context a comparison on an event-per-event basis between C8C1 and C1C1 is of interest. Again the sensitivity to the absolute energy scale will be removed by using the following residuals: $\frac{\Delta E}{E} = 100 \cdot \frac{E_{C1C1} - E_{C8C1}}{E_{C8C1}}$ and $\Delta x_i = x_i^{C1C1} - x_i^{C8C1}$. The distribution of the distance between both reconstructed vertices versus the distribution of the relative energy difference is shown in Figure 6.22 for Sample A. Most events line
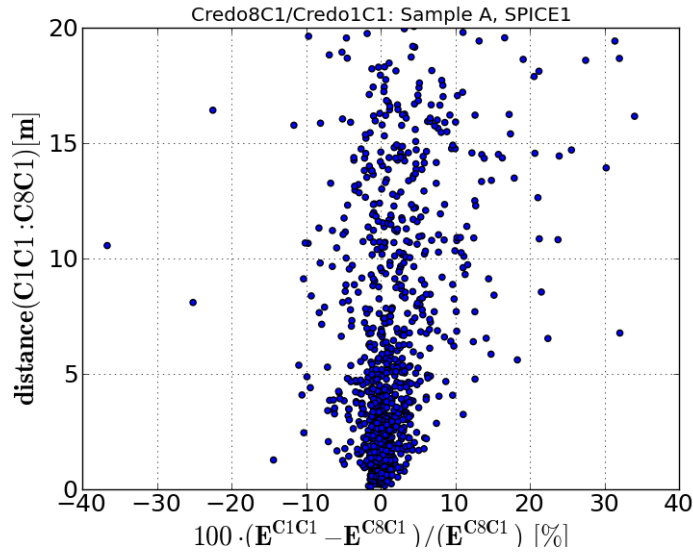
FIGURE 6.22: **Sample A**: Distance d between the reconstructed vertices of C8C1 and C1C1 versus the relative difference in the energy estimate $\frac{\Delta E}{E} = 100 \cdot \frac{E_{C1C1} - E_{C8C1}}{E_{C8C1}}$

up at a straight line, where the reconstructed energies of C1C1 and C8C1 agree within $\sigma_{\Delta \frac{\Delta E}{E}} \approx 2\%$, but for a class of events both estimates disagree, producing the scattered results in Figure 6.22. Hence for those events, the reconstructed energy seems to be unstable, which will further be investigated in the next section.

6.4 Credo and Monopod: Saturation Effects

This section addresses the large non-gaussian tails observed in the distributions of the reconstructed x and y positions of C8C1 and M8C1 (Figure 6.21, bottom left) as well as the remaining per-event disagreement between the energy estimates of C8C1 and C1C1 (Figure 6.22). In Figure 6.23 (left) we plot the distance between the reconstructed vertex as obtained by C1R and the true vertex (position of shower maximum) versus the distance of that shower maximum to the closest (brightest) DOM. The average distance between the true position of the shower maximum and the solution found by Credo

(C1R) increases with decreasing distance of that true vertex to the closest optical module. By looking at the waveforms it can be understood, why events close to a DOM typically are misreconstructed. An example of such waveforms (ATWD and fADC) is shown in Figure 6.23 for a DOM which measured the light yield near the shower maximum ($d \approx 20\,\mathrm{m}$). The upper plot shows the two ATWD waveforms, as measured by the two digitizers, each covering a time window of $450\,ns$. The lower plot shows the corresponding fADC waveforms with a coverage of $6400\,\mathrm{ns}$. The first fADC waveform (blue) is clipped during the first $\sim 1500\,\mathrm{ns}$ of the event, due to its limited dynamic range. Since for the ATWD it is possible to record the waveform via the low gain[7] input, the ATWD waveform does not get clipped. However it should be noted, that the ATWD waveform (blue) exceeds a current of $50\,\mathrm{mA}$ by more than a factor of two. Thus during the full ATWD time window the PMT measured in the deeply non-linear regime (see sec: 3). This means, that the linear relation between the observed amount of photoelectrons and the amount of incident photon used in pulse extraction and calibration does not hold anymore, making this waveform mostly unusable during reconstruction. The second DOM launch (red) is caused by PMT afterglow (see [58] for details) and hence does not provide useful information during reconstruction.

Since Photonics does not include saturation effects in its charge prediction, these pre-
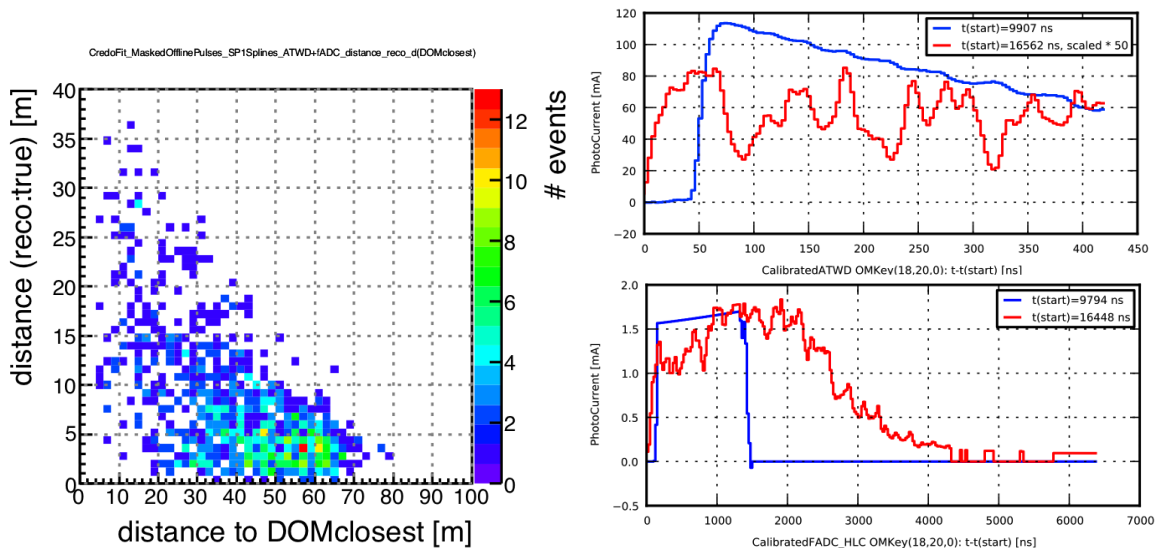
FIGURE 6.23: A correlation between the distance to the reconstructed vertex (C1R) to the true vertex and the distance of that shower maximum to the closest DOM (left); ATWD (top right) and fADC (bottom right) waveforms measured by a DOM close to the shower maximum $d \approx 20\,\mathrm{m}$

dictions can not be compared to the calibrated pulses in that regime.

---

[7]The difference in amplification between the low-gain ATWD the fADC signals is about a factor of 90

Consider a Photonics predicted charge μ_{oi} for pulse i in dom o being in the saturated regime. The corresponding measured charge q_{oi} will be much smaller then the prediction. Since cascade reconstruction algorithms assume the measured charge q_{oi} to follow a Poisson distribution with mean μ_{oi}: $P\left(q_{oi}, \mu_{oi}\right) = \frac{\mu_{oi}^{q_{oi}} e^{-\mu_{oi}}}{q_{oi}!}$, the real hypothesis $\underline{C}_0$ will become highly unlikely. Hence the mismatch between prediction and observation penalizes the true hypothesis w.r.t to other hypotheses, which thus might have a better likelihood and will be found as solution. Until a proper parametrization of that effect is found, those DOMs which took data in the non-linear regime will be removed from the fits to prevent introducing such misleading penalty terms in the likelihood. Hence DOMs, which satisfy the following criteria, will be excluded from C8C1 and M8C1, as suggested in [77]:

- $I_{phot}^{o}\left(t\right) > 50\,\mathrm{mA},\ t \in T$

- $Q_{tot}^{o} > 10 \cdot \left\langle Q_{tot}^{HLC} \right\rangle$

with T being the duration of the event and $\left\langle Q_{tot}^{HLC} \right\rangle$ denotes the average total charge of all HLC pulses of the corresponding event. The second condition removes DOMs, which during the event measured at least a factor of 10 more charge, than the average of all optical modules. This prevents the algorithm to be sensitive to DOMs with large amounts of charge, for which indications of non-poissonean behavior exists [50]. The effect of removing bright DOMs on the C8C1 and M8C1 results is shown in Figure 6.24.

For both algorithms the reconstructed energy shifts towards higher energies. In case of C8C1 the bias decreased from $\mu_{\frac{\Delta E}{E}} \approx -34\%$ to $\mu_{\frac{\Delta E}{E}} \approx -12\%$ while the resolution improved from $\sigma_{\frac{\Delta E}{E}} \approx 14\%$ to $\sigma_{\frac{\Delta E}{E}} \approx 10\%$. The energy distribution of M8C1 shows strong deviation from the expected gaussian distribution due to the presence of a significant side peak. It was verified that this structure remains stable against changing the seed to M1R or increasing the number of iterations to 16, with bright DOMs still being removed. Hence for Monopod, removing bright DOMs leads to a worse energy reconstruction performance than before[8]. By comparing the distributions of all parameters provided M8C1 and C8C1, shown in Figure 6.24, one can see that the vertex resolution of M8C1 is worse by up to $2\,\mathrm{m}$ compared to C8C1, while also showing a worse resolution in the reconstructed zenith of $\theta_{RMS}^{M8C1} = 48°$ compared to $\theta_{RMS}^{C8C1} = 27°$. Before removing bright DOMs both algorithms showed the same performance (compare Figure 6.21). The results for all parameters, as obtained from the fits to gaussian distributions are given in Table 6.8.

We will now compare the distributions of Δx for C8C1 before removing bright DOMs

---

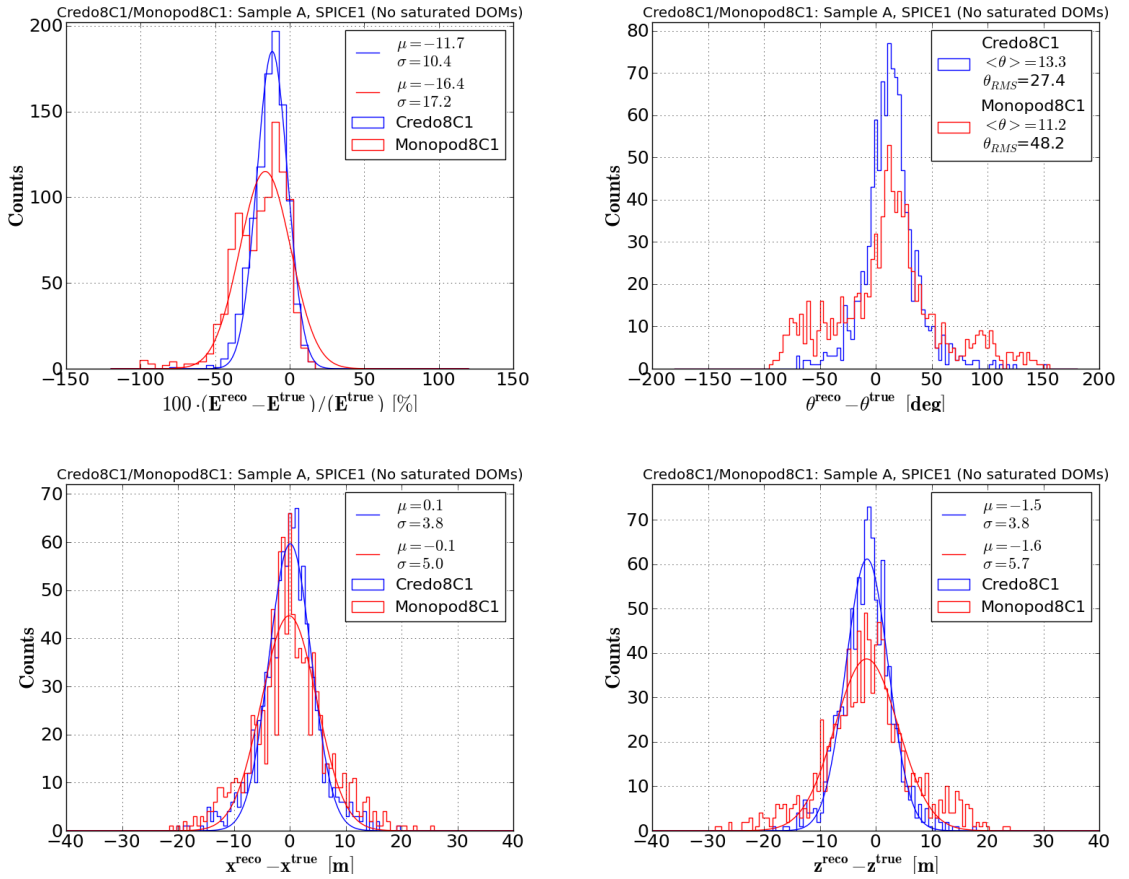[8]This statement holds for Monopod as part of Millipede.release.V01-01-00, used in this study.

FIGURE 6.24: **Sample A:** Reconstruction results of M8C1 and C8C1 for energy $\frac{\Delta E}{E}$ (top left), zenith $\Delta\theta$ (top right), Δx (bottom left) and Δz (bottom right); Bright DOMs removed

$\mu_{\Delta x} \pm \sigma_{\Delta x}$ [m]	$\mu_{\Delta y} \pm \sigma_{\Delta y}$ [m]	$\mu_{\Delta z} \pm \sigma_{\Delta z}$ [m]	$\mu_{\frac{\Delta E}{E}} \pm \sigma_{\frac{\Delta E}{E}}$	$\overline{\Delta\theta} \pm RMS_{\Delta\Theta}$
M8C1				
-0.1 ± 5.0	0.0 ± 5.6	-1.6 ± 5.7	$(-16.4 \pm 17.2)\,\%$[9]	$(11.2 \pm 48.2)°$
C8C1				
0.1 ± 3.8	-0.1 ± 4.2	-1.5 ± 3.8	$(-11.7 \pm 10.4)\,\%$	$(13.3 \pm 27.4)°$

TABLE 6.8: **Sample A:** Resolution and Bias for M8C1 and C8C1; Bright DOMs removed; Based on Figure 6.24

(Figure 6.21, bottom left) and after removing bright DOMs (Figure 6.24, bottom left). It can be seen, that while preserving a resolution of about $\sigma_{\Delta x} \approx 4\,\mathrm{m}$, the large tails towards miss reconstructed vertices, which are present in Figure 6.21, vanished in Figure 6.24 after removing bright DOMs. The same is true for the y-component. Hence in addition to improving the estimated energy of C8C1, removing bright DOMs also improves

---

[9]The distribution is not gaussian, hence the given values have no probabilistic meaning. However it shows that M8C1 after removing bright DOMs reconstructs to higher energies compared to before (see 6.6)

the reconstructed position in the xy-plane. On the other hand by comparing the Δz distribution of C8C1 in Figure 6.21 (bottom right) to the Δz distribution of C8C1 in Figure 6.24 one can see that the resolution $\sigma_{\Delta Z}$ worsened by $\sim 1\,\mathrm{m}$ after removing bright DOMs, while preserving the gaussian shape. This can be explained due to the cuts used to remove bright DOMs. Since the optical modules are much denser populated along z, those criteria will mainly remove DOMs in the z direction, which otherwise would constrain the position of the shower maximum in the z direction. In addition the zenith worsened from before $\theta_{RMS}^{C8C1} = 19°$ to $\theta_{RMS}^{C8C1} = 27°$ after those cuts, which remove the DOMs which detect the largest fraction of unscattered photons (closest to the shower maximum).

In addition to studying the influence on the reconstruction resolution, it is interesting to investigate the influence of removing bright DOMs on the per-event agreement of the energy estimates of C81C1 and C1C1. For a class of events both energy estimates differed before removing bright DOMs, leading to presence of results, which scatter widely in Figure 6.22. The corresponding distribution in the 2D plane, showing the fractional difference in the energy estimate of C8C1 and C1C1 vs the distance between both reconstructed vertices after removing bright DOMs in sample A, is shown in Figure 6.25. Compared to Figure 6.22 the scattered results vanished and nearly all events line
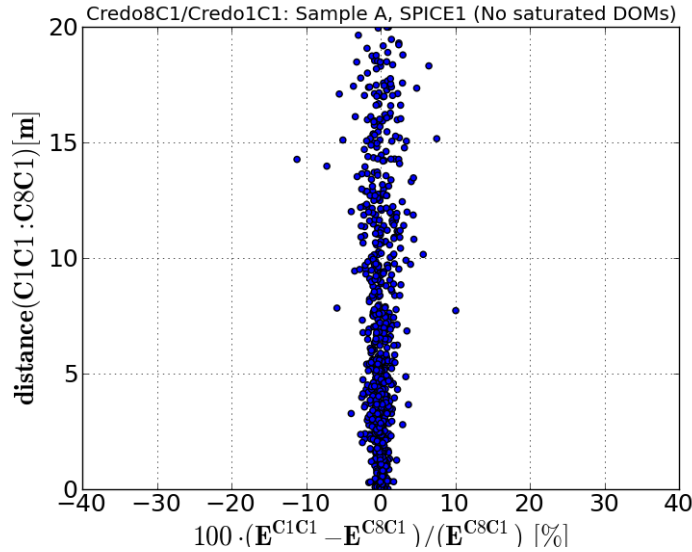
FIGURE 6.25: **Sample A**: Distance d between the reconstructed vertices of C8C1 and C1C1 versus the relative difference in the energy estimate $\frac{\Delta E}{E} = 100 \cdot \frac{E_{C1C1} - E_{C8C1}}{E_{C8C1}}$; Bright DOMs removed

up within $\sigma_{\frac{\Delta E}{E}} \approx 1\%$. Hence removing bright DOMs not only improved resolution and bias of the reconstructed energy, it also removed the dependency of the reconstructed energy on the amount of iterations, thus providing a stable energy estimate.

The discussion of the reconstruction resolution and bias after removing bright DOMs based on Sample A also holds for Sample B, as shown in table 6.9, with the results of C1R and C4C1 being obtained after removing bright DOMs. This can be compared to table 6.7 showing the results before removing bright DOMs. The difference compared to sample A is that the resolution in zenith remains unchanged with $\theta_{RMS}^{C4C1} = 15°$ (before) and $\theta_{RMS}^{C4C1} = 14°$ (after). We conclude that removing bright DOMs will be helpful in

$\mu_{\Delta x} \pm \sigma_{\Delta x}$ [m]	$\mu_{\Delta y} \pm \sigma_{\Delta y}$ [m]	$\mu_{\Delta z} \pm \sigma_{\Delta z}$ [m]	$\mu_{\frac{\Delta E}{E}} \pm \sigma_{\frac{\Delta E}{E}}$	$\overline{\Delta\theta} \pm RMS_{\Delta\Theta}$
C1R				
0.1 ± 3.7	0.0 ± 3.6	-1.0 ± 2.8	$(-11.6 \pm 13.3)\,\%$	$(9.6 \pm 28.6)°$
C4C1				
-0.1 ± 3.3	0.0 ± 3.0	-1.0 ± 2.2	$(-11.9 \pm 13.4)\,\%$	$(5.8 \pm 14.1)°$

TABLE 6.9: **Sample B**: Resolution and bias for C4C1 and C1R; $\xi = 0.77$; Bright DOMs removed;

searches for high energetic cascades at the Glashow resonance, for which an accurate energy estimate is a fundamental necessity. Since this was not achieved by using Monopod (V01-01-00), only Credo will be considered in the subsequent studies .

6.5 Credo: Influence of the ice model

In section 4.3 it was discussed, that the optical properties of the glacial ice, which are used during reconstruction, have been obtained by fitting the scattering and absorption coefficients (among others) to the measured light yield of the flasher LEDs on string 63. Those parameters are subject to statistical and systematic errors. Hence during the reconstruction of experimental data, the optical properties are likely to show small deviations from the best fit values especially at large distances from string 63. The results presented so far, can be interpreted as conservative in a sense that the simulated events have been reconstructed using an ice model (SPICE1), which shows deviations from the one (SpiceMie) used during the production of the simulated data (sec. 4.3). This section aims at estimating the sensitivity of the Credo result on the optical properties of the ice, by using the same ice model (SpiceMie) for reconstruction, which was used to simulate the samples A and B.

According to the findings of section 6.4, bright DOMs are excluded and a constant Photonics correction of $\xi = 0.77$ is used. Based on the combined results of Cscd-llh, ACER and ToI 4-iterations (C4R) and 8-iterations (C8R) of Credo are used. The results are shown in Figure 6.26 for Sample A.
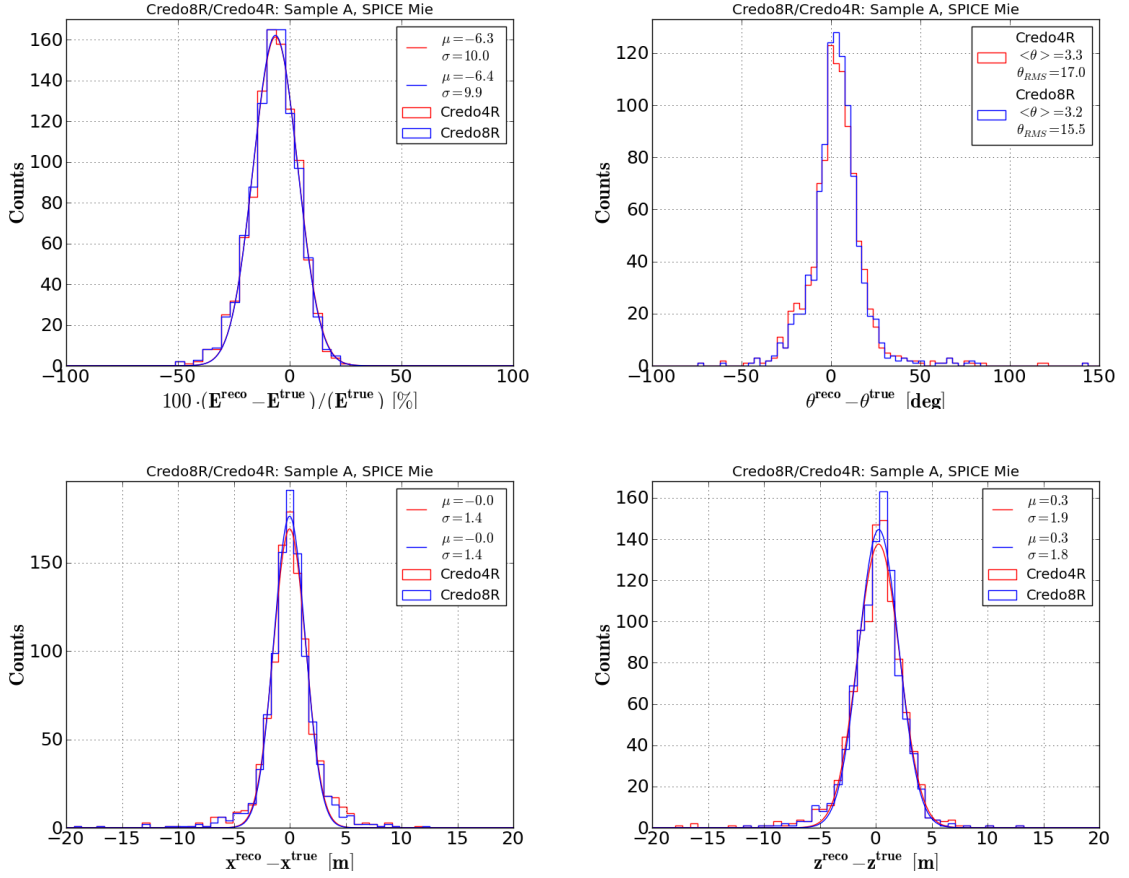
FIGURE 6.26: **Sample A:** Reconstruction results of C4R and C8R for energy $\frac{\Delta E}{E}$ (top left), zenith $\Delta\theta$ (top right), Δx (bottom left) and Δz (bottom right); Bright DOMs removed; SpiceMie ice model

First of all, the results of all parameters (vertex, energy, zenith) are almost independent of the number of iterations, indicating a very stable fit result. Compared to the best result achieved when using SPICE1, C8C1 in Figure 6.24, using SpiceMie decreased the C8R bias in Figure 6.26 of the energy from $\mu_{\frac{\Delta E}{E}} = -11.7\%$ to $\mu_{\frac{\Delta E}{E}} = -6.3\%$, while the resolution shows only a tiny improvement from $\sigma_{\frac{\Delta E}{E}} = 10.4\%$ to $\sigma_{\frac{\Delta E}{E}} = 9.9\%$. The effect of using the correct optical properties mainly influences the reconstructed vertex and zenith. While the resolution $\sigma_{\Delta x_i}$ in all three vertex parameters improved by at least a factor of 2, the bias in the z-coordinate decreased from $\mu_{\Delta z} = -1.5\,\mathrm{m}$ for C8C1 using SpiceMie to $\mu_{\Delta z} = 0.3\,\mathrm{m}$ for C8R using SpiceMie. The results, shown in Figure 6.26, are summarized in Table 6.10 for sample A. In addition the results of using the true parameters $\underline{C}_0 = \{\vec{x}_0, \theta_0, \phi_0, E_0, t_0\}$ as seed, are shown for 8 iterations of Credo (C8T). No improvement compared to C8R is achieved. Since having the true parameters as seed represents the most optimal initial conditions for a fit, we can conclude, that, given a precise knowledge of the ice properties, already few iterations of Credo (C4R) provide the best possible estimate of the Cascade parameters. Thus the results given in Table

$\mu_{\Delta x} \pm \sigma_{\Delta x}$ [m]	$\mu_{\Delta y} \pm \sigma_{\Delta y}$ [m]	$\mu_{\Delta z} \pm \sigma_{\Delta z}$ [m]	$\mu_{\frac{\Delta E}{E}} \pm \sigma_{\frac{\Delta E}{E}}$	$\overline{\Delta\theta} \pm RMS_{\Delta\Theta}$
C4R				
0.0 ± 1.4	0.1 ± 1.4	0.3 ± 1.9	-6.3 ± 10.0	$(3.3 \pm 17.0)^\circ$
C8R				
0.0 ± 1.4	0.1 ± 1.4	0.3 ± 1.8	-6.4 ± 9.9	$(3.2 \pm 15.5)^\circ$
C8T				
0.1 ± 1.3	0.1 ± 1.3	0.4 ± 1.7	-6.3 ± 9.9	$(2.9 \pm 15.5)^\circ$

TABLE 6.10: **Sample A**: Resolution and bias for C8T, C8R and C4R $\xi = 0.77$; Bright DOMs removed

6.10 show the intrinsic resolution, i.e. the limiting resolutions, that can be achieved by having the optimal input. The remaining resolution therefore is mostly related to the approximations underlying the method: assuming point like cherenkov emission, the non-inclusion of the detector response in the Photonics simulation, deviations from poisson statistics for bright pulses etc.

Those observations also hold for sample B, as shown in Table 6.11 using SpiceMie for C8T, C8R and C4R. The latter can be compared to the result, given in Table 6.9, based on SPICE1. While the accuracy of the energy estimate remains unchanged, the other parameters show strong improvements.

Figure 6.27 compares the reconstruction results obtained by C8T for both samples.

$\mu_{\Delta x} \pm \sigma_{\Delta x}$ [m]	$\mu_{\Delta y} \pm \sigma_{\Delta y}$ [m]	$\mu_{\Delta z} \pm \sigma_{\Delta z}$ [m]	$\mu_{\frac{\Delta E}{E}} \pm \sigma_{\frac{\Delta E}{E}}$	$\overline{\Delta\theta} \pm RMS_{\Delta\Theta}$
C4R				
0.1 ± 1.1	0.0 ± 1.2	-0.4 ± 1.3	-11.5 ± 12.1	$(4.1 \pm 8.8)^\circ$
C8R				
0.0 ± 1.1	0.0 ± 1.1	-0.4 ± 1.3	-11.5 ± 12.1	$(4.0 \pm 7.5)^\circ$
C8T				
0.1 ± 1.1	-0.1 ± 1.1	-0.3 ± 1.3	-11.4 ± 11.9	$(4.0 \pm 7.4)^\circ$

TABLE 6.11: **Sample B**: Resolution and bias for C8T, C8R and C4R; $\xi = 0.77$; Bright DOMs removed

Due to the clearer ice below the dust layer the reconstructed parameters which have a strong dependence on timing information (influenced by scattering) show an improved resolution for Sample B.

So far the discussion of the dependence of the results on the ice model only considered the bias and resolution. In Sample B below the dust layer another parameter is of
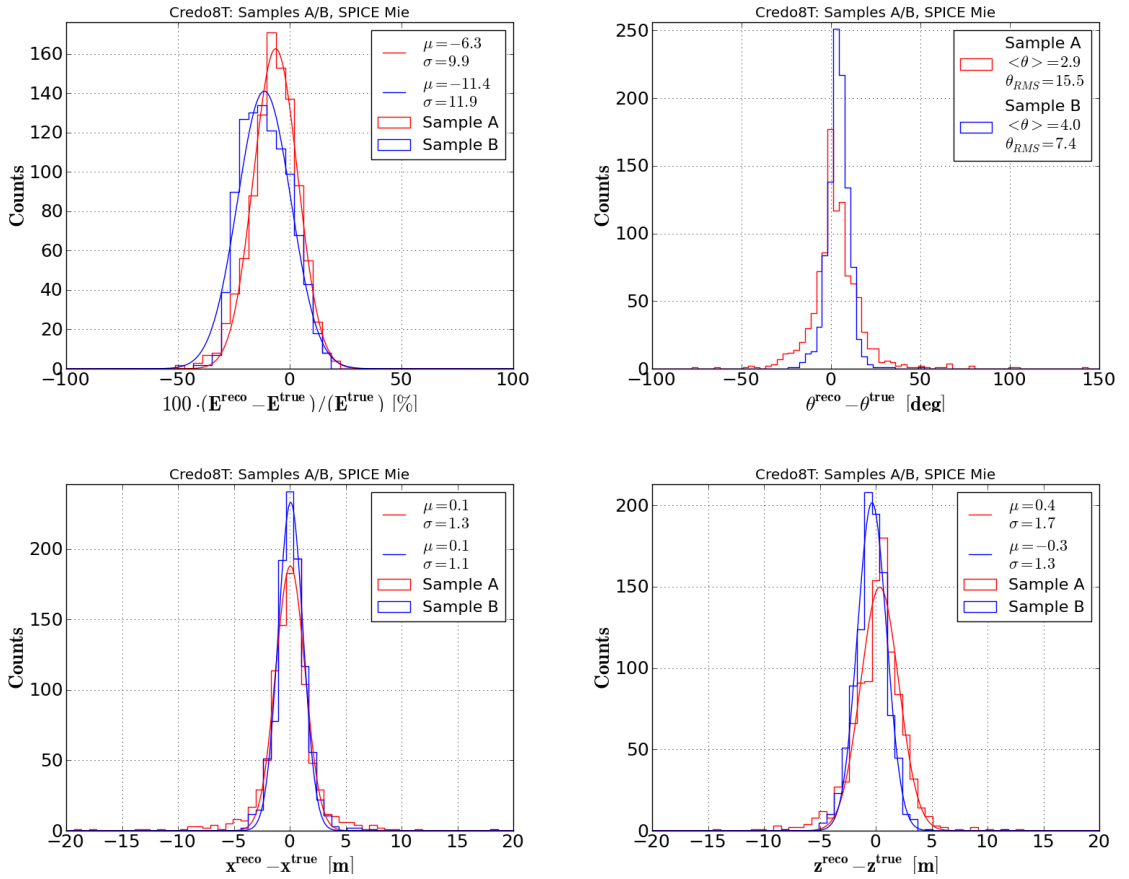
FIGURE 6.27: **Samples A and B:** Reconstruction results of C8T for $\frac{\Delta E}{E}$ (top left), zenith $\Delta\theta$ (top right), Δx (bottom left) and Δz (bottom right); Bright DOMs removed; SpiceMie ice model

importance, which is the number events for which Credo did not converge. When using SpiceMie for both samples the algorithm always converges. In the case of SPICE1, i.e. when the ice model used deviates from the optical properties underlying the data, such a contributions exists. Independent of the settings used to run Credo, this contribution was 0.1% in case of sample A and between 8% and 10% for sample B. This supports the interpretation that the reconstruction becomes more sensitive to its seed, when the ice model deviates from the "true" properties, as was argued above, when discussing, that the results become independent of the number of iterations in case of matching optical properties. Above the dust layer the reconstructed vertex provided by Cscd-llh is known to be more accurate than below the dust layer. Hence below the dust layer the contribution of failed fits is larger than above the dust layer. Thus while in principle increasing the number of iterations can make up for some of the differences between the ice model of use and the true optical properties, as was shown in sec. 6.3.6, the amount of failed fits can only be improved by either improving the seed or the ice model of use.

Chapter 7

Cascade Reconstruction Performance for Standard Candle Experimental Data

In this section we will broaden the cascade reconstruction performance studies presented so far, by using in-situ light pulses independent of simulations. The Standard Candle Laser was designed to act as a calibrated light source to gauge cascade reconstruction algorithms at high energies in a real environment, especially focusing on the calibration of the absolute energy scale. After the deployment of the Standard Candle's at the south pole, the in-situ light yield was found to significantly deviate from the lab calibrated values. However given its pulse-per-pulse stability of 3% [62], we can use the Standard Candle to test cascade reconstruction algorithms on experimental data. Only the absolute energy scale will not be accessible. Since the Standard Candle is deployed at a fixed position with a well defined direction and a stable light output, the question to be answered in this section is, how well this is reflected in the Credo reconstruction results.

7.1   Standard Candle II Data

In the last chapter the best Credo performance was achieved below the dust layer, thus the Standard Candle II was chosen for this study to minimize the impact of scattering and absorption on the result. The latest Standard Candle II data have been taken on the 13th of January 2011 for the different filter wheel settings. Given the dynamic brightness of the Standard Candle (sec. 3.4) the energy of interest w.r.t the Glashow Resonance should be reflected at a brightness between 1% and 10%. In order to minimize the effect of saturation, the 1% brightness dataset (Run 117411) was chosen. This dataset has

already been filtered from background (i.e. cosmic ray muons) and provides a purity of $> 99\%$. The Standard Candle is located on String 55 between DOMs 42 and 43 ($x_{SCII} = 11.87\,\mathrm{m}$, $y_{SCII} = 179.19\,\mathrm{m}$, $z_{SCII} = -205.64\,\mathrm{m}$). The vertex resolution will subsequently be defined as the deviation of the reconstructed vertex from the position of the SCII, given above:

$$\Delta x^i = x^i_{credo} - x^i_{SCII} \tag{7.1}$$

Since the SCII was deployed facing downwards, the deviation $\Delta\theta$ of the reconstructed zenith θ_{credo} from the true zenith $\theta_{SCII} = 0°$ equals the reconstructed zenith θ_{credo}. Hence we define the zenith resolution as follows:

$$\Delta\theta = \theta_{credo} \tag{7.2}$$

The total light yield of the Standard Candle II, and hence the cascade energy equivalent, is subject to large systematic uncertainties. It can not be used to measure the energy resolution. Therefore we will subsequently define the energy resolution $\frac{\Delta E}{E}$ with respect to the average energy estimate $\langle E_{credo}\rangle$:

$$\frac{\Delta E}{E} = 100 \cdot \frac{E_{credo} - \langle E_{credo}\rangle}{\langle E_{credo}\rangle} \tag{7.3}$$

7.2 Credo: Performance

The processing of SC II Run 117411 was done in early 2011 when WaveCalibrator and WaveDeform had yet to be released. In order to benefit from the advances in calibration since then (i.e. beacon baseline subtraction), the experimental data needed to be reprocessed. In accordance with the strategy used throughout this thesis 1000 events have been selected. For this sample the raw waveforms have been calibrated, using WaveCalibrator (Release V11-08-00), before extracting and calibrating light pulses, using WaveDeform (Release V01-00-03). The Standard Candle events were then reconstructed using Credo (Release V00-02-03) within IceRec (Release V04-02-00). The reconstruction used spline fitted photonics tables based on SPICE1 as ice model and OfflinePulses without noise cleaning, as before. The seeding strategy is based on the results of last section.

At first, we used one iteration of Credo (C1R) based on the results of Cscd-llh, ACER and ToI as a seed. Four iterations of Credo (C4C1), seeded with the C1R result, are then used to study the reconstruction performance. In this study all DOMs are included and the constant Photonics correction $\xi = 0.77$ is applied.
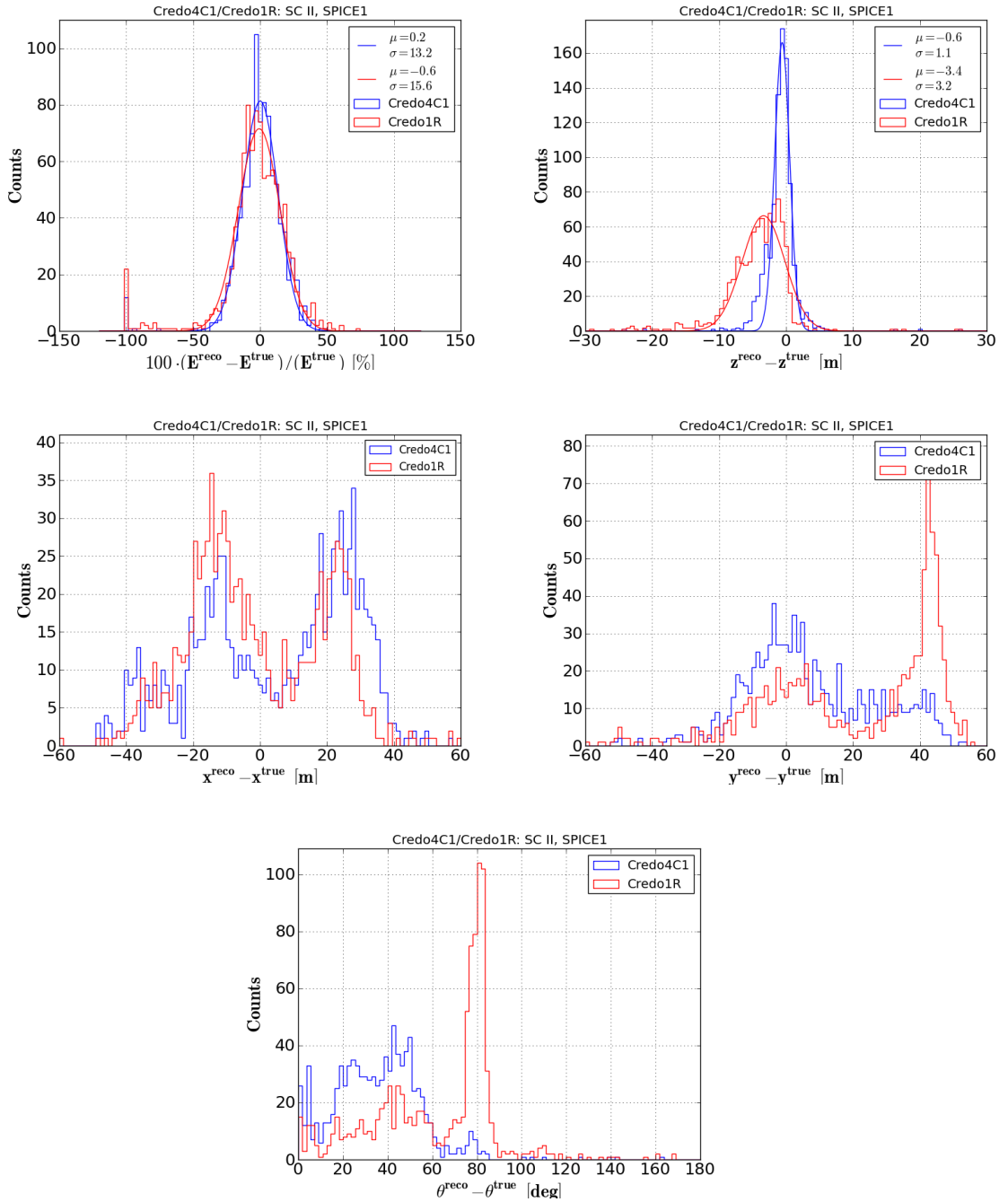
FIGURE 7.1: **SCII:** Resolution and bias as obtained by C4R and C4C1; $\frac{\Delta E}{\langle E_{C4C1} \rangle}$ (top left), Δz (top right), Δx (center left), Δy (center right), $\Delta \theta$ (bottom)

The average value of the C4C1 energy estimate was found to be $\langle E_{C4C1} \rangle = 543 \, \text{TeV}$. Given the lab calibrated light yield of the laser, one would have expected an energy around $1 \, \text{PeV}$. However indications exist, that the actual in-situ light output is dimmed by a factor of 2 for unknown reasons, which means that given this large uncertainty, the result is not in tension with the expectation.

Figure 7.1 shows the distributions of $\frac{\Delta E}{\langle E \rangle}$, Δx_i and $\Delta\theta$ for C1R and C4C1 reconstructions. Given that those 1000 cascades should all be described with almost the same parameters, the result is disillusioning. The distributions in the polar plane (Figure 7.1, center left and center right) do not show gaussian behavior, but develop a spiky structure, no matter whether one or four iterations were used. The same is true for the zenith distribution (Figure 7.1, bottom). In addition the distributions are highly sensitive to changing the number of iterations, while improving only marginally. The only distributions that show expected shapes are $\frac{\Delta E}{\langle E_{C4C1} \rangle}$ (Figure 7.1, top left) and Δz (Figure 7.1, top right), while both imply poor resolutions of $\sigma_{\Delta z} \approx 1.1\,m$ and $\sigma_{\frac{\Delta E}{\langle E_{C4C1} \rangle}} \approx 13\%$ respectively , given that all those cascades should be identical.

We investigate the correlation between the reconstructed x and y positions in figure 7.2. The results of C1R (left) and C4C1 (right) are distributed in a ring like structure
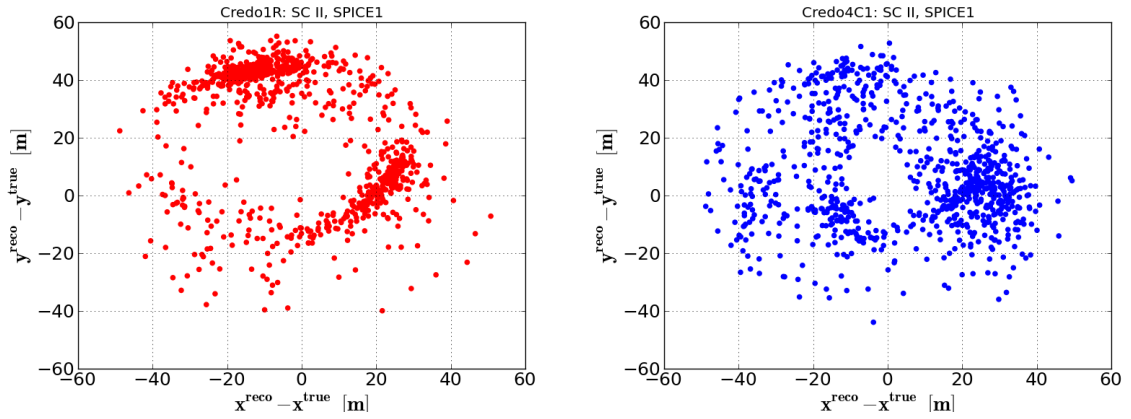

FIGURE 7.2: **SCII:** Reconstructed cascade positions in the X,Y-plane for C1R (left) C4C1 (right); Standard Candle position $(\Delta X, \Delta Y) = (0\,m, 0\,m)$

around the position of the standard candle, i.e. the position of string 55 ($\Delta x = 0$, $\Delta y = 0$), where the laser is situated. Increasing the number of iterations only smeared this structure. Although these rings are not spherically symmetric around the position of string 55, this strongly points towards saturation effects.

As discussed in sec. 6.4, when a DOM becomes saturated, the measured charge will be much smaller then the Photonics prediction, based on the true hypothesis. Hence the true solution gets penalized and the likelihood prefers the vertex to be shifted from string 55.

An example of the waveforms of the DOMs on string 55 neighboring the Standard Candle is shown in figure 7.3 for DOM 42 (left) and DOM 43 (right). Photocurrents about $100\,mA$ and larger indicate, that those DOMs operated in the deeply non-linear
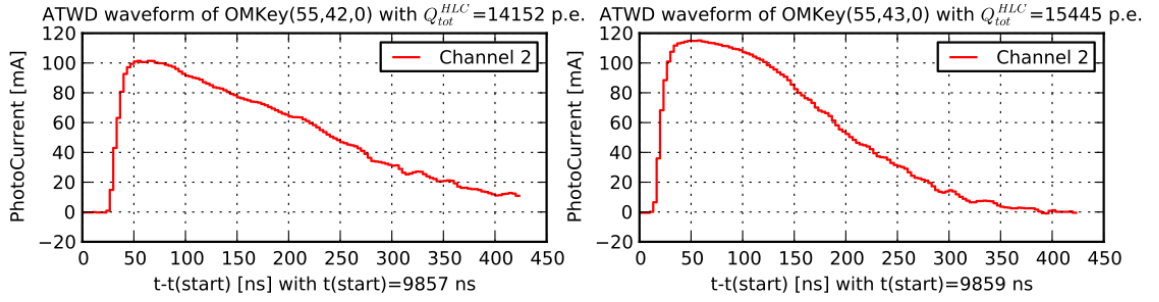
FIGURE 7.3: **SCII:** Example ATWD waveforms of the DOMs neighboring the SCII below (left) and above (right)

regime of the PMT. Hence it seems worthwhile to exclude saturated DOMs from the cascade reconstruction algorithm to study, whether the results (Figure 7.1) improve.

7.3   Credo: Saturation Effects

The selection criteria, which were used in section 6.4 to minimize saturation effects in the reconstruction, were applied to this set of Standard Candle Cascades.

- $I_{phot}^o \left(t \right) > 50 \, \text{mA}, \ t \in T$

- $Q_{tot}^o > 10 \cdot \left\langle Q_{tot}^{HLC} \right\rangle$

with T being the duration of the event and $\left\langle Q_{tot}^{HLC} \right\rangle$ denotes the average total charge of all HLC pulses of the corresponding event. In 99.6% of all events the same 8 DOMs out of on average (average of all events) ~ 619 DOMs, which recorded light, got excluded. The eight DOMs, which were removed, are distributed symmetrical around the Standard Candle position on String 55, ranging from DOM 39 to DOM 46. Such a symmetry is expected from the spherical light pattern of the Standard Candle Events. Given the stable light yield of the laser, one would expect those criteria to select the same DOMs in 100% of all events. The presence of four events for which fewer DOMs were removed, could be traced to be due to a problem with the mainboard firmware, used during Run 117411 (see Appendix A). The issue was found not to influence the reconstruction result.

Figure 7.4 shows the distributions for $\frac{\Delta E}{\langle E_{C4C1} \rangle}$ (top left), Δz (top right), Δx (center left), Δy (center right), $\Delta \theta$ (bottom left) after excluding bright DOMs in C1R and C4C1 reconstructions. A contribution of failed reconstructions (about 8% of all events) is not shown in Figure 7.4. For those events C1R preferred a vertex solution outside the detection volume. Since the C1R result was subsequently used to seed additional iterations, C4C1 did not converge for those events. This reflects that no solution exists outside the detection volume.
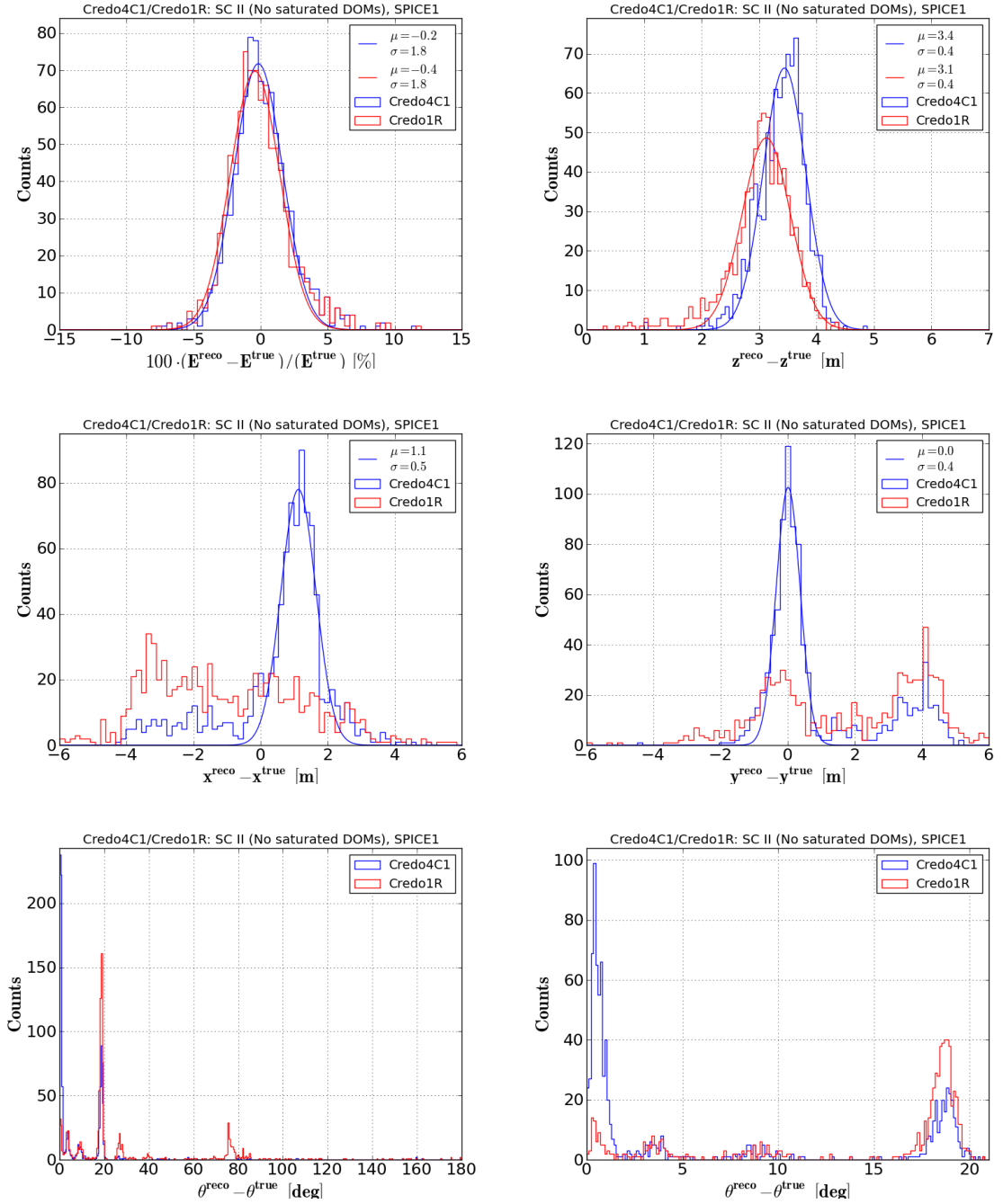
FIGURE 7.4: **SCII:** Saturated DOMs removed; Resolution and bias as obtained by C4R and C4C1; $\frac{\Delta E}{\langle E_{C4C1} \rangle}$ (top left), Δz (top right), Δx (center left), Δy (center right), $\Delta \theta$ (bottom left), $\Delta \theta$ zoomed (bottom right)

Excluding those eight saturated DOMs yielded strong improvements of the fit results, which will be discussed below.

Energy

The energy resolution improved by almost an order of magnitude from $\sigma_{\frac{\Delta E}{E}} \approx 13\%$ before removing bright DOMs (top left plot of Figure 7.1) to $\sigma_{\frac{\Delta E}{E}} \approx 1.8\%$ (top left plot of Figure 7.4) afterwards. The achieved resolution lies now well within the lab calibrated pulse-per-pulse stability of the laser of 3% [62]. The influence of excluding saturated DOMs on the on average reconstructed energy is small. It slightly decreased from $\langle E_{C4C1} \rangle = 543\,\text{TeV}$ to $\langle E_{C4C1} \rangle = 527\,\text{TeV}$. By comparing the distribution of C1R to C4C1 in the top left plot of Figure 7.4, one can see, that the reconstructed energy remains stable against increasing the amount of iterations. This confirms the same observation made in sec. 6.4 based on electron neutrino simulations.

Z-Coordinate

The effect of removing saturated DOMs on the z-coordinate is two fold. The resolution $\sigma_{\Delta z}$ achieved by C4C1 improved by more than a factor of 2 from $\sigma_{\Delta z} = 1.1\,\text{m}$ (top right plot of Figure 7.1) to $\sigma_{\Delta z} = 0.4\,\text{m}$ (top right plot of Figure 7.4). The bias $\mu_{\Delta z}$ of the C4C1 result however became worse. Before this step, the standard candle was reconstructed to be on average $0.6\,\text{m}$ below its actual position, which afterwards on average yields a position $3.4\,\text{m}$ above the true value. The strongest constraints on the reconstructed position typically come from the DOMs closest to the light source, because the first photons, measured close to the source, are less affected by scattering than others. All saturated DOMs, removed in the Standard Candle events, lie on the same string. Hence the distance along the string (along z) between the contributing DOMs and the source increased. In result, scattering becomes more important and makes the reconstruction result more sensitive to differences between the ice model and the actual optical properties of the glacial ice. However given the strong improvements of resolutions in energy and z-position, this is acceptable.

The top right plot of Figure 7.4 shows the Δz distributions for the C4C1 and C1R reconstructions. The reconstruction result remains sensitive to the number of iterations. Although the two distributions share the same resolution, they differ in bias and normalization. The C1R result $\mu_{\Delta z} = 3.1\,\text{m}$ is slightly less biased than the C4C1 result $\mu_{\Delta z} = 3.4\,\text{m}$. The large discrepancy in normalization is due to the presence of a second peak in the Δz distribution of C1R in the region $\Delta z < 0\,\text{m}$, which is shown in Figure 7.5. This structure makes up most of the contribution of $\sim 17\%$ of all events, which, after additional iterations, get fully recovered and add to the single peak in the Δz distribution of C4C1, thus explaining the difference in normalization in the top right
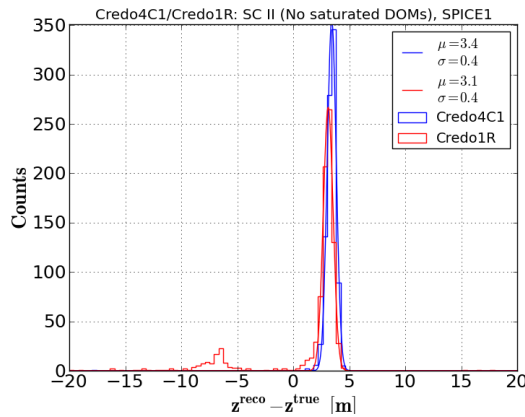
FIGURE 7.5: **SCII:** Saturated DOMs removed; Resolution and bias of Δz as obtained by C4R and C4C1; same as Figure 7.4 (top left)

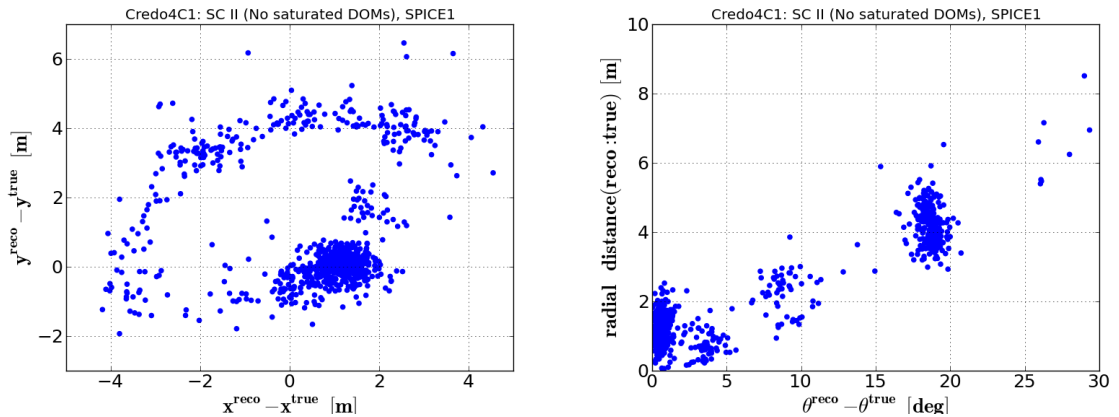plot of Figure 7.4.

The XY-Plane

FIGURE 7.6: **SCII:** Reconstructed cascade positions in the X,Y-plane for C4C1 (left); Radial distance of the reconstructed vertex to string 55 vs reconstructed zenith for C4C1 (right)

Before removing saturated DOMs, the solutions covered an area of about $\sim 10.000\,\mathrm{m}^2$ in the xy-plane, distributed in a ring like structure around string 55, as shown in Figure 7.2 (right). The left plot in Figure 7.6 shows, that for C4C1 this area shrunk to $\sim 50\,\mathrm{m}^2$ after removing bright DOMs, while in figure 7.4 the corresponding distributions of Δx (center left) and Δy (center right) develop gaussian peaks near the true position of the Standard Candle in the xy-plane $(\Delta x, \Delta y) = (0\,\mathrm{m}, 0\,\mathrm{m})$. However in addition to the main peaks some side structure is still present, forming a partial ring of miss-reconstructed events. The sensitivity of the result to the number of iterations, as discussed above in the context of Δz, is even stronger in the case of Δx and Δy, as shown in centered plots of figure 7.4, comparing C4C1 to C1R. The latter does not show dominant peaks close to the true

position of SCII. The gaussian peaks in case of the C4C1 result indicate resolutions of $\sigma_{\Delta x} = 0.5\,\mathrm{m}$ and $\sigma_{\Delta y} = 0.4\,\mathrm{m}$ while only the Δx distribution is biased with $\mu_{\Delta x} = 1.1\,\mathrm{m}$.

The Zenith

Before removing bright DOMs the reconstructed zenith is distributed widely over most of the down going region ($\theta_{reco} < 85°$), without showing any preference for $\theta_{SCII} = 0°$, as shown at the bottom of Figure 7.1. This drastically changed after removing bright DOMs. The results of C4C1 are now mostly contained in two peaks with small structure in between, as shown at the bottom of Figure 7.4 (bottom left and bottom right). The main peak contains events with reconstructed zenith $\theta_{C4C1} < 2°$ (54%), which means the Credo reconstruction algorithm determines the direction of the cascade to be straight down going for these events. However a contribution of mis-reconstructed events forms a pronounced second peak (24%) in the region of $17° < \theta_{C4C1} < 21°$, as well as smaller contributions between both peaks. The right plot in Figure 7.6 shows that the events with a reconstructed zenith within the main peak $\theta_{C4C1} < 2°$ of the zenith distribution in 7.4 (bottom) have a distance of $\rho = \sqrt{\Delta x^2 + \Delta y^2} < 2\,\mathrm{m}$ to the position of the Standard Candle in the xy-plane, whereas the events in the second peak around $\theta_{C4C1} \approx 18°$ are distributed at $\rho \approx 4\,\mathrm{m}$. Hence the events with a misreconstructed zenith angle form the partial ring, observed in the left plot of Figure 7.6. The correlation between the reconstruction results concerning zenith and vertex position can be used to define the number of well reconstructed events N_{good} with $\theta_{Credo} < 2°$ and N_{bad} with $17° < \theta_{Credo} < 21°$ We stress again the strong dependence of the fit result on the number of iterations, as visible in 7.4 (bottom). In case of C1R the second peak of misreconstructed events N_{bad} is dominant over a small contribution of well reconstructed events N_{good}. In addition a significant number of events is reconstructed with $\theta_{C1R} > 21°$. All of the latter are recovered by additional iterations thus contributing to N_{good} for C4C1.

The aim throughout the last part of this thesis will be to increase the fraction N_{good}/N_{bad} of those events, thought to be well reconstructed.

7.4   Credo: Sensitivity to the Number of Iterations and final Result

In sec. 4.3 it was shown, that increasing the number of iterations improves the reconstruction result in case of insufficiencies in ice modeling. We will now study the influence of increasing the number of iteration on the Credo reconstruction performance, as follows: Based on the C4C1 result (Figure 7.4) another 8 iterations of Credo (C8C4) will be added. The result will be compared to 16 iterations of Credo based on Cscd-llh,ACER

and ToI (C16R) before a final estimate will be given by additional 16-iterations of Credo (C16C16). This is summarized in Figure 7.7. Using this scheme, we study whether the fraction N_{good}/N_{bad} improves. In addition one might ask which ratio would be achievable in case of having an infinite amount of iterations, i.e. whether this procedure will converge. This will be estimated using the "best" seed, which will be defined below.

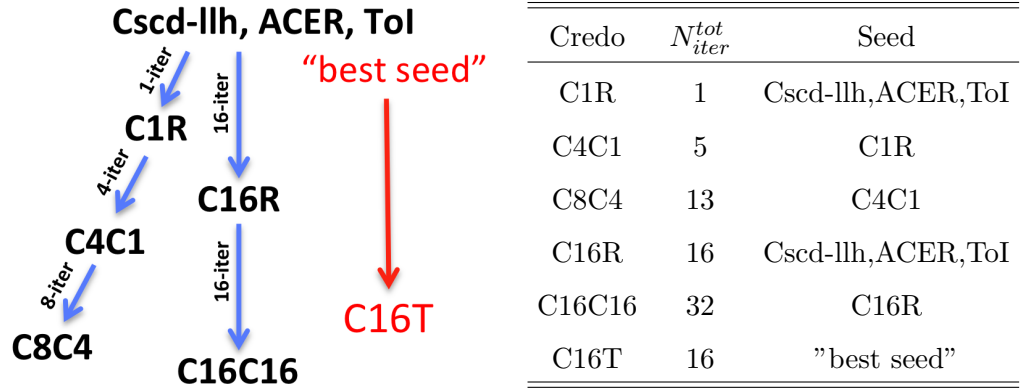Consider the case of an unbiased reconstruction result. To estimate the best possible

Credo	N_{iter}^{tot}	Seed
C1R	1	Cscd-llh,ACER,ToI
C4C1	5	C1R
C8C4	13	C4C1
C16R	16	Cscd-llh,ACER,ToI
C16C16	32	C16R
C16T	16	"best seed"

FIGURE 7.7: **SCII:** seeding scheme to study sensitivity of reconstruction results on iterations

performance, one can use the true parameters $\underline{C}_0$ of the Cascade, we want to reconstruct, as seed. This will improve the previous result, in case of insufficient accuracy of the ice model. To make sure that the Gaussian distributions, which will be centered around $\underline{C}_0$, represent global minima, several iterations are needed. When using the true parameters as seed the resolutions will therefore either remain stable or decrease with increasing number of iterations,

As we have seen in Figure 7.4, the result of C4C1 is biased in x ($\mu_{\Delta x} = 1.1\,m$) and z ($\mu_{\Delta z} = 3.4\,m$). We interpreted the values of each Cascade parameter, at which the corresponding distributions in Figure 7.4 are centered, as the preferred solution (the position of a global minimum in the likelihood space) of Credo. This solution should then especially be preferred over the position of the problematic side peaks, we observed. Hence the "best" seed will be the true parameters, corrected for the bias in the distribution of the corresponding variable. We use the bias, observed in the C16R (same as C8C4) results (Fig. 7.8), to calculate the following best seed values for C16T:

- $X_{best}^i = X_{SC}^i + \mu_{\Delta x^i} = (13.1\,\mathrm{m}, 179.3\,\mathrm{m}, -202.1\,\mathrm{m})$

- $E_{best} = \langle E_{Credo} \rangle = 527\,\mathrm{TeV}$

- $\theta_{best} = 0.0°$

Figure 7.8 shows a comparison between the results for C8C4 and C16R. The distribu-

FIGURE 7.8: **SCII:** Resolution and bias as obtained by C16R and C8C4; $\frac{\Delta E}{\langle E_{C4C1}\rangle}$ (top left), Δz (top right), Δx (center left), Δy (center right), $\Delta \theta$ (bottom left), $\Delta \theta$ zoomed (bottom right); bright DOMs removed

tions of $\frac{\Delta E}{\langle E_{C4C1}\rangle}$ are shown in the top left plot. No difference between C8C4 (13-iterations in total) and C16R (16-iterations in total) is observed. This confirms the observation previously made, that after removing bright DOMs the reconstructed energy is stable against the number of iterations and the best resolution is already achieved after 1-iteration (Figure 7.4, top left plot).

The top right plot of Figure 7.8 shows the reconstruction results of C8C4 and C16R for the z-component. The distributions are similar. The difference between the corresponding values for the resolution $\sigma_{\Delta z} = 0.3\,\mathrm{m}$ and bias $\mu_{\Delta z} = 3.5\,\mathrm{m}$ (C16R,C8C4) and the ones obtained by C4C1 as shown in Figure 7.4 (top right, $\sigma_{\Delta z} = 0.4\,\mathrm{m}$, $\mu_{\Delta z} = 3.4\,\mathrm{m}$) are neglegibile. However a small difference is observed in the normalization. That means, that increasing the number of iterations helps to recover a handful of events, for which the minimizer was stuck in a local minimum for C4C1.

The distributions of Δx (center left) and Δy (center right) are given in Figure 7.8. In both cases even the small increase in iterations from 13 (C8C4) to 16 (C16R) reduces the amount of miss reconstructed events (visible as tails in the distributions). Hence they add to the main peak of C16R without changing the resolution ($\sigma_{\Delta x} = 0.4\,\mathrm{m}$, $\sigma_{\Delta y} = 0.3\,\mathrm{m}$) and bias ($\mu_{\Delta x} = 1.2\,\mathrm{m}$, $\mu_{\Delta y} = 0.1\,\mathrm{m}$). As was the case for the z-component, the differences between those parameters and the ones obtained for C4C1 (Figure 7.4) are neglegibile. The main improvement compared to C4C1 is given by the strong reduction of the contribution of the side peak structure, formed by misreconstructed events. The zenith distribution of C16R and C8C4 is shown at the bottom of Figure 7.8. The only difference between both is given by the relative contribution of events in the main peak $\theta_{Credo} < 2°$ (N_{good}) and the second peak at $17° < \theta_{Credo} < 21°$ (N_{bad}). For C16R we find a ratio of $N_{bad}/N_{good} = 11\%$, while for C8C4 $N_{bad}/N_{good} = 22\%$ holds. This is a strong improvement compared to the case of C4C1 (Figure 7.4) with $N_{bad}/N_{good} = 45\%$.

To determine the best possible result, we compare C16C16 to C16T in Figure 7.9. As one can see, after 32 iterations (C16C16) for all parameters (energy, vertex, zenith) Credo converges at its best possible result (C16T). The tails visible in the distributions of Δx (center left), Δy (center right) as well as the second peak in zenith θ become almost neglegibile in both cases. The achieved resolutions and biases for all parameters remain stable at the ones obtained before (Figure 7.8). This results in a fraction $N_{bad}/N_{good} = 7\%$ for C16C16 and $N_{bad}/N_{good} = 5\%$ in the limiting case C16T.

A quantitative summary of the results of this section can be found in table 7.1, showing the improvements in the ratio N_{bad}/N_{good}. Table 7.2 shows the stability of the resolution and bias as obtained from fitting the main peaks of the respective distributions to gaussian distributions. An event-by-event comparison showed remarkable agreement between the results obtained by C16C16 and C16T for the well reconstructed events N_{good}. The reconstructed energies are in agreement within $\sigma_{\frac{\Delta E}{E}} \sim 0.2\%$, while the reconstructed vertex components agree within $\sigma_{\Delta x_i} \sim 0.1\,\mathrm{m}$.

The sensitivity of the Credo reconstruction results for Standard Candle events on the number of iterations, observed in this section, by far exceeded the sensitivity found in
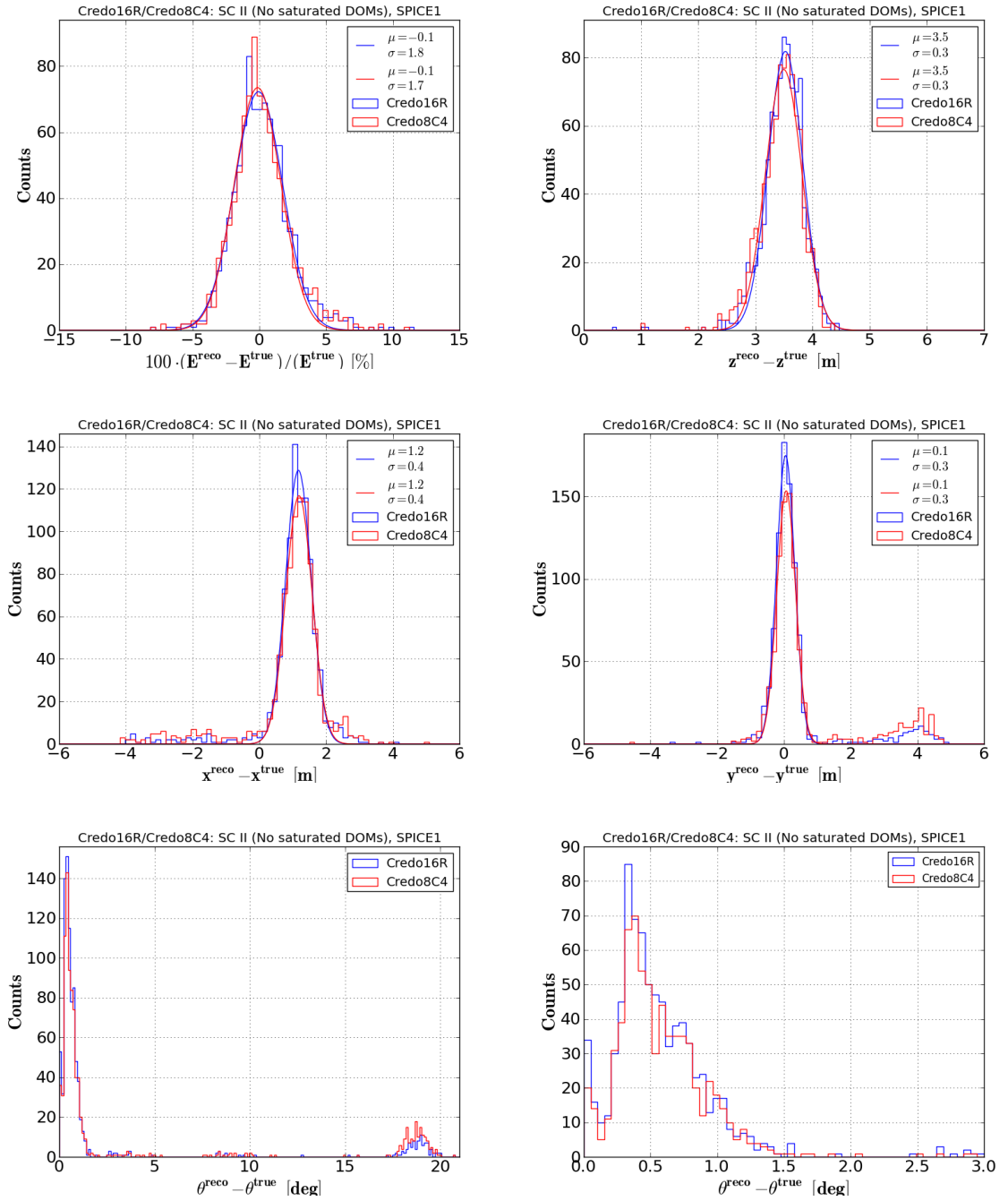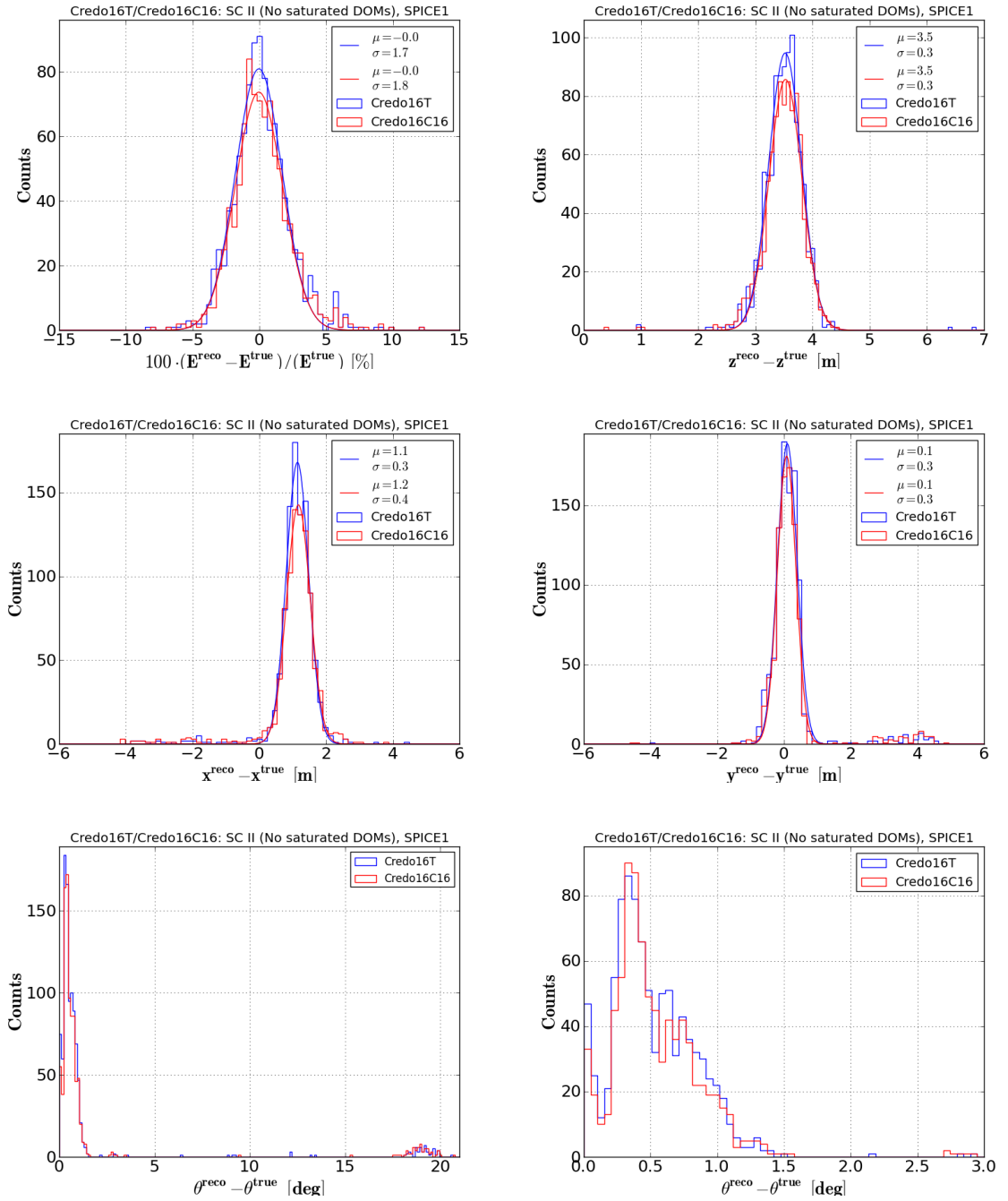
FIGURE 7.9: **SCII:** Resolution and Bias as obtained by C16T and C16C16; $\frac{\Delta E}{\langle E_{C4C1} \rangle}$ (top left), Δz (top right), Δx (center left), Δy (center right), $\Delta \theta$ (bottom left), $\Delta \theta$ zoomed (bottom right); bright DOMs removed

section 6.4, where we studied simulated neutrino events. For Monte Carlo data, this sensitivity mainly concerned the achieved resolutions. No strong impact on the shapes of the corresponding distributions was observed, i.e. the distributions after removing bright DOMs were found to be gaussian. In sec. 6.4 we attributed the remaining sensitivity on the number of iterations to be caused by differences between the ice models

used during simulation and reconstruction. This interpretation was based on the fact, that in section 6.5 the reconstruction was shown to be stable against those changes, when the reconstruction was based on the true ice model. In addition the contribution of failed reconstructions, previously observed, vanished.

We think that this difference between our Standard Candle and Monte Carlo results is to be expected, mainly for several reasons. First the Standard Candle emits photons at a wavelength of 337 nm only. At this wavelength the description of scattering and absorption in the SPICE1 ice model, which was used throughout this section, is based on an extrapolation from the values obtained by fitting in-situ LED data at 400 nm. This extrapolation in turn relies on AMANDA[1] measurements, which did not reach the depth at which SCII operates. Second and more importantly the simulated photons, used to determine the arrival time distributions and their normalization for a cascade with parameters $\underline{C}_0$ in Photonics, follow the Cherenkov spectrum, which differs from the monochromatic emission of the Standard Candle. Although the amount of radiated cherenkov photons increases with frequency, when convoluted with the spectral acceptance of the DOM, the Photonics results will be dominated by photons around ~ 390 nm. Given that those deficiencies are expected to be larger than any difference between SPICE1 and SpiceMie, it is not a surprise, that the reconstruction performance for Standard Candle events, as found in sec. 7.3, is more sensitive to the amount of iterations, than the results obtained based on simulated neutrino events in sec. 6.4.

As discussed in sec. 6.5 in the context of sample B (Monte Carlo Events, below the dust layer), when the ice model, used during reconstruction, differs from the true ice properties, a contribution of failed fits is expected, especially below the dust layer ($\sim$ 8%). This was attributed to be due to the insufficient accuracy in the vertex seed, provided by Cscd-llh below the dust layer. As shown in table 7.1 (NFailed and $N_{d>500\,\mathrm{m}}$) such a contribution ($\sim 10\%$) also exists for various reconstruction results obtained for SCII, which are directly or indirectly related to a Cscd-llh seed. Based on the Cscd-llh seed C1R and C16R reconstruct a number $N_{d>500\,m}$ of events to lie outside the detection volume of IceCube. For those events subsequent reconstructions (C4C1, C8C4 C16C16) are very likely to fail, because of the extremely bad seed. This problem can either be resolved by improving the ice model of use (see sec. 6.5) or by improving the seed. The influence of the latter is visible for C16T. The contribution of such events decreased from $\sim 10\%$ (C16R) to 1.5% (C16T). Hence most of the difference between C16C16 and C16T can be attributed to be due to his problem. If we remove the affected events from the respective samples, the fraction of N_{good}/N_{tot} improves from 83% to 90% for C16C16, which is to be compared to a change from 92% to 94% for of C16T. Hence further

---

[1]AMANDA is the small predecessor of IceCube, deployed at depths between 1500 m and 1900 m

improvements due to increasing the number of iterations beyond 32 will be negligibile.

Settings	N_{good}	N_{bad}	NConverged	NFailed	$N_{d>500\,m}$
Credo1R	70	458	991	9	93
Credo4C1	522	235	920	71	24
Credo8C4	700	153	910	10	14
Credo16R	786	90	1000	0	95
Credo16C16	832	62	927	73	22
Credo16T	923	50	1000	0	14

TABLE 7.1: **SCII:** N_{good} and N_{bad} for various Credo settings; In addition Number of Converged Reconstructions *NConverged*, Number of events with failed fits *NFailed* and Number of extremely miss reconstructed vertices $N_{d>500\,m}$ are given

Settings	$\mu_{\Delta x} \pm \sigma_{\Delta x}$ [m]	$\mu_{\Delta y} \pm \sigma_{\Delta y}$ [m]	$\mu_{\Delta z} \pm \sigma_{\Delta z}$ [m]	$\sigma_{\frac{\Delta E}{E}}$
Credo1R	*	*	3.1 ± 0.4	1.8%
Credo4C1	1.1 ± 0.5	0.0 ± 0.4	3.4 ± 0.4	1.8%
Credo8C4	1.2 ± 0.4	0.1 ± 0.3	3.5 ± 0.3	1.7%
Credo16R	1.2 ± 0.4	0.1 ± 0.3	3.5 ± 0.3	1.8%
CredoC16C16	1.2 ± 0.4	0.1 ± 0.3	3.5 ± 0.3	1.8%
Credo16T	1.1 ± 0.3	0.1 ± 0.3	3.5 ± 0.3	1.7%

TABLE 7.2: **SCII**: Resolution and Bias for various Credo settings; Values obtained from fitting the main peaks of the respective distributions to gaussian distributions; * The distribution does not show gaussian peaks

Chapter 8

Summary and Outlook

One of the primary goals of IceCube, a telescope detecting Cherenkov light in an instrumented ice volume of $1\,\mathrm{km}^3$ at the South Pole, is to observe the flux of high-energy cosmic neutrinos and anti-neutrinos from astrophysical sources. The (anti-)neutrino spectrum near the characteristic energy $E_\nu \approx 6.3\,\mathrm{PeV}$ of the Glashow resonance, the interaction of anti-neutrinos with atomic electrons via $\bar\nu_e e^- \to W^-$, is of particular interest, since it offers the unique possibility to determine the contribution from electron anti-neutrinos. Such a flux, if observed, provides new constraints on the possible production mechanisms for high-energy (anti-)neutrinos in astrophysical sources. The observation of extra-terrestrial (anti-)neutrinos at even higher energies may furthermore make it possible to probe the electroweak structure of nucleons at energies beyond the reach of current collider experiments.

The dominant signatures of neutrino interactions at the Glashow Resonance in IceCube are particle showers, originating from hadronic W^- decay with a combined branching ratio of $\sim 70\%$. The remaining $\sim 30\%$ originate in equal amounts from leptonic decays, with $W^- \to e^- + \bar\nu_e$ channel producing an electromagnetic shower, $W^- \to \mu^- + \bar\nu_\mu$ a track, and $W^- \to \tau^- + \bar\nu_\tau$ various signatures related to the subsequent τ decay. In this work, we described first IceCube performance studies with advanced reconstruction algorithms for (anti-)neutrino induced particle showers (cascades) in the energy range of the Glashow Resonance using simulations as well as data obtained by pulsing an in-situ laser.

The simulations consisted of the generation of events, simulated detector response, and reconstruction with the existing two most-advanced IceCube algorithms named Credo and Monopod. Only hadronic signatures were considered in the simulations, since it was found in the starting phase of this work, that the simulation of leptonic channels

yielded unphysical results[1]. The initially discrepant energies for $\bar{\nu}_e$-induced cascades reconstructed by Credo and Monopod were reconciled by using consistent descriptions for the light yield and propagation in the Antarctic ice. We furthermore studied the influence of repeated reconstruction passes (iterations), of the modeling of the ice properties and illumination of different detector regions, and of readings from the digital optical modules (DOMs), that operated at high input currents, thus leading to a non-linear response (saturation). The latter was found to have the strongest impact on the cascade reconstruction. The removal of saturated DOM readings prior to the reconstruction was found to result in a cascade energy estimate that is robust against the number of iterations of the reconstruction. The loss of timing information from these DOMs was shown to have only a modest impact on the accuracy of the reconstructed cascade position and zenith angle. For cascades at the Glashow resonance that are well contained in the IceCube instrumented volume, we achieved a Credo energy resolution of $10\% < \sigma\left(\Delta E/E\right) < 14\%$ depending on the ice model and the cascade position within the detector. A correctable bias was found in the mean reconstructed energy of $-12\% < \mu\left(\Delta E/E\right) < -6\%$, depending on the ice model and the cascade position within the detector. Stronger biases were found for the reconstructed shower position and the zenith angle, θ, of the incident flux as reconstructed from the cascade signature. The position resolution was found to be $1.1\,\mathrm{m} < \sigma\left(\Delta \mathrm{x, y, z}\right) < 4.2\,\mathrm{m}$ and the angular resolution $8° < \theta_{RMS} < 27°$. We thus conclude from our Monte Carlo simulations that resonant interactions of electron anti-neutrinos with atomic electrons in the IceCube detector can be reconstructed with a relative energy resolution better than 15% and directional sensitivity better than 30°. Future simulations studies would include an extension to partially contained signal events and background rejection.

To verify the above conclusions without reliance on Monte Carlo simulations, we studied the performance of the Credo cascade reconstruction algorithm from data obtained by pulsing an in-situ laser, named Standard-Candle-II (SCII), that is deployed on one of the IceCube detector strings and faces downwards. We analyzed data recorded with a constant 1% of the maximum brightness, corresponding to an average reconstructed energy of $527\,\mathrm{TeV}$. This brightness level was chosen in order to keep the number of saturated DOM readings at a manageable level. After excluding saturated DOM readings from the reconstruction, we found an energy resolution of $\Delta E/E = 1.8\%$ for laser events, independent of the number of iterations. The reconstruction of positions and directions were found to rely crucially on iterations, possibly because of differences in the propagation of photons with wavelengths of $\lambda = 400\,\mathrm{nm}$, as entered the method, and with the laser frequency of $\lambda = 337\,\mathrm{nm}$ in ice. A new determination of photon

---

[1]This has since been resolved for the μ decay channel, and the τ branch is being resolved as this thesis was written in the Fall of 2012.

response at the laser frequency and subsequent reconstruction are needed to confirm or disprove this statement. After 32 iterations, the reconstructed zenith angle was found to have adequately converged and a resolution of $\theta < 2°$ was obtained for 83% of all SCII events. This fraction was 92%, when the reconstructed best fit values are used as initial condition in Credo. We obtained vertex resolutions of $0.3\,\mathrm{m} < \sigma\,(\Delta\mathrm{x,y,z}) < 0.4\,\mathrm{m}$ for these events and observed a systematic difference of $3.7\,\mathrm{m}$ between the reconstructed and known SCII position. Our analysis of the data obtained with SCII thus qualitatively confirms the conclusions from our Monte Carlo simulations. Quantitatively, the SCII data present a best-case scenario. This analysis constitutes a first proof-of-principle based on data, that IceCube has angular sensitivity for high energy cascades.

Based on our present understanding of cascade reconstruction in IceCube, we anticipate to be able to observe $1 - 2$ contained cascade events per year at the Glashow resonance energy for an electron anti-neutrino flux $E^2\Phi = 1.0 \times 10^{-8}\,\mathrm{GeV} \cdot \mathrm{cm}^{-2} \cdot \mathrm{s}^{-1} \cdot \mathrm{sr}^{-1}$ consistent with current flux limits [78]. Analysis of partially contained cascade signals could double this rate, provided that adequate reconstruction and background rejection can be achieved, without a significant loss of detection efficiency. IceCube intends to operate its recently completed instrument well into the next decade and we thus look forward to the actual observation of the Glashow resonance, or alternatively to significantly sharpened limits on the flux of high-energy extra-terrestrial neutrinos.

Appendix A

Firmware Problems in Run 117411

For Run 117411, version 442 of the mainboard firmware controlling the FPGA logic was used, which later was shown to be problematic. If a local coincidence criterion is satisfied, ATWD recording of 450 ns is initiated, which causes a 29 μs deadtime for this ATWD chip during digitization (sec. 3.3). However during Run 117411 ATWD digitization was triggered, whenever the discriminator threshold value, was exceeded without checking for LC. This lead to cases, in which a random noise hit, produced in the time gap between two Standard Candle flashes, by accident triggers fADC+ATWD recording (instead of fADC only). Since for a signal event the ATWD typically records the main fraction of the measured charge, the respective DOM would miss a significant fraction of the Standard Candle light in such a case. An example of this effect is shown in figure A.1.

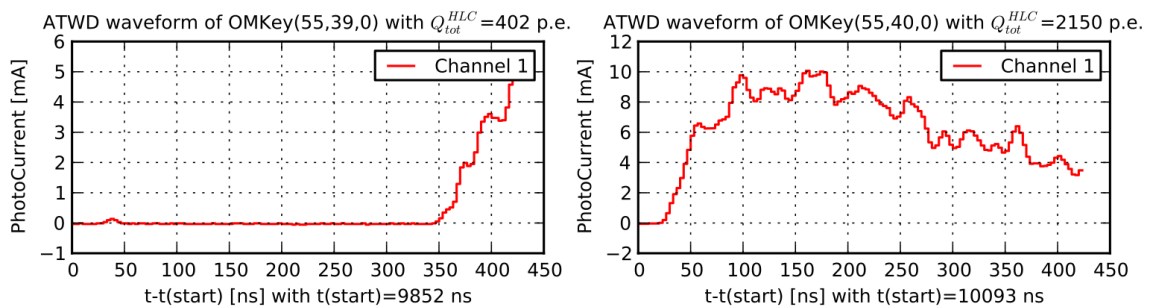In this Figure the waveforms for DOMs 39 (left) and 40 (right) on string 55 are shown

FIGURE A.1: **SCII:** Example ATWD waveform affected by a ATWD deadtime issue (left), to be compared to the waveform of the neighboring DOM (right), which is not affected

for one SCII event. Since DOM 40 is closer to the Standard Candle one would expect it to be launched before DOM 39. In contrast the ATWD waveform of DOM 40 starts

at $t = 10093\,\text{ns}$ whereas DOM 39 already detected a signal at $t = 9852\,\text{ns}$. In addition DOM 39 only measures a total charge of $402\,\text{p.e.}$, while DOM 40 detected $2150\,\text{p.e.}$. Such a large difference can not be explained by the distance of $17\,\text{m}$ between both DOMs. Since the total charge observed by DOM 39 is less then 10 times the average total charge of all DOMs for that event $(10 \cdot \langle q_{tot} \rangle_{DOMs} = 1050\,\text{p.e.})$, this DOM has not been removed from the reconstruction for that event (see sec. 7.3). However on average over all events DOM 39 recorded a total charge of $\langle q_{tot} \rangle^{DOM39}_{Events} = 1382\,\text{p.e.}$ and hence would have been removed. Due to the missing charge, it did not happen. The same is true for the other three events, for which less than eight DOMs have been removed. We will now investigate the influence of that problem on the reconstruction results, presented in section 7.3.

The total charge q^o_{tot} observed in DOM o should sample from a poisson distribu-
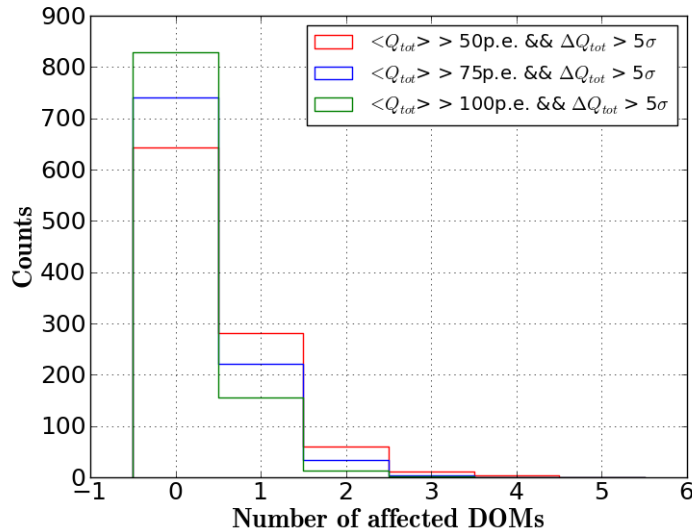

FIGURE A.2: **SCII:** Distribution of the amount of DOMs, marked as affected by deadtime problems for different criteria

tion $p\left(q^o_{tot}\right) = \frac{\mu_o^{q^o_{tot}} e^{-\mu_o}}{q^o_{tot}!}$ with μ_o being the mean of the total expected charge. Due to the pulse-per-pulse stability of the Standard Candle one can in a good approximation calculate μ_o from the SCII data as the mean total charge $\langle q^o_{tot} \rangle$ of all 1000 cascades. Since with increasing μ^p_o the poisson distribution is increasingly well described by a gaussian distribution with $\mu^g_o = \mu^p_o$ and standard deviation $\sigma^g_o = \sqrt{\mu^p_o}$ we identify affected DOMs by the requirement $\Delta q^o_{tot} = |q^o_{tot} - \langle q^o_{tot} \rangle| > 5 \cdot \sigma_g$ with $\sigma_g = \sqrt{\langle q^o_{tot} \rangle}$. Since this argument only holds for $\mu_o \gg 10\,\text{p.e.}$, only DOMs with $\langle q^o_{tot} \rangle > \{50, 75, 100\}$ [p.e.] will be considered. For example 79 DOMs satisfy $\langle q^o_{tot} \rangle > 75 p.e.$. The distribution of the number of DOMs, which have been marked by those criteria in a single event, is shown in Figure A.2. More than 30% of all events contain at least one DOM with an expected total charge$\langle q_o \rangle > 50\,p.e.$, which is marked as problematic. The effect on the
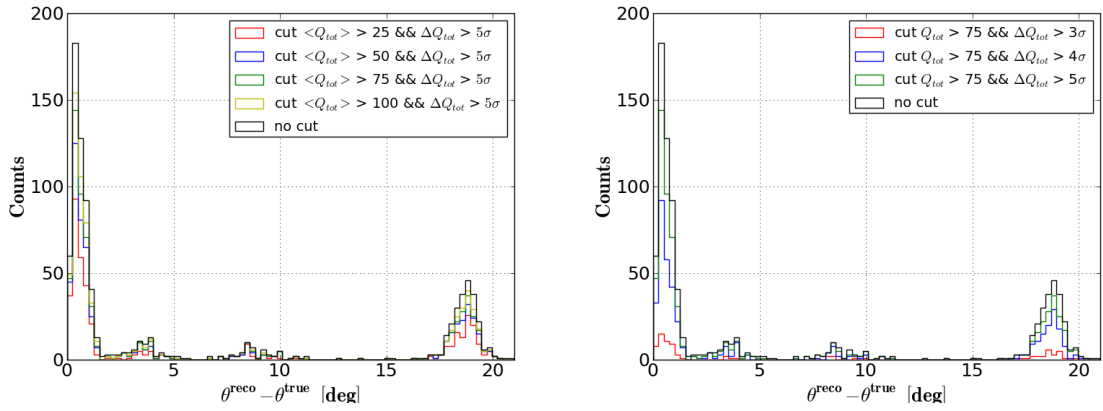
FIGURE A.3: **SCII:** reconstructed zenith distributions of Credo (C4C1); Potentially deadtime bug affected events are removed for different criteria, see text; (Left:) Removed events with $\Delta q^o_{tot} > 5\sigma$ and required total charge $\langle q^o_{tot} \rangle > \{50, 75, 100\}$ [p.e.]; (Right:) Removed events with $q^o_{tot} > 75$ p.e. and $\Delta q^o_{tot} > \{3, 4, 5\}\sigma$

reconstruction result is negligible, as shown in Figure A.3. In the left plot of Figure A.3 the Credo (C4C1) reconstructed zenith distributions are shown, with events, containing at least one DOM with a deviation of $\Delta q^o_{tot} > 5\sigma_g$ while the total charge of that DOM on average was $\langle q^o_{tot} \rangle > q$ (with $q \in \{25, 50, 75, 100, 10^5\}$ [p.e.]), being removed. Since no DOM observed more charge than $10^5 \, p.e.$ the corresponding curve shows the case of no cut being applied.

On the right side of Figure A.3 the Credo (C4C1) zenith distribution is shown, when events, with an average observed total charge of $\langle q^o_{tot} \rangle > 75$ p.e., which in addition have shown larger deviations from $\langle q^o_{tot} \rangle$ than $N \cdot \sigma_g$ (with $N \in \{2, 3, 4, 5, 10^4\}$), are removed. The last value was chosen artificially large to show the case without any cut.

None of those combinations significantly improved the ratio N_{bad}/N_{good}.

Affected DOMs will introduce penalty terms into the likelihood, as discussed in the case of saturation effects (sec. 7.3). However not observing an influence of the deadtime problem on the reconstruction result, while observing strong effects due to saturation is not in tension. The absolute value of the likelihood does not impact the best fitting hypothesis, but the likelihood ratio between competing hypotheses does. In case of of saturation, several DOMs clustering around the true hypothesis contribute to penalty terms, thus making hypotheses different from the true hypothesis to be preferred. In case of the deadtime problem less DOMs are affected, which due to noise being random in nature, are not correlated with each other in space. The correlation between the penalty terms and the position of the corresponding DOM relative to the position of the true vertex is significantly weaker than in case of saturation.

Bibliography

[1] F. Halzen and S. R. Klein. "Invited Review Article: IceCube: An instrument for neutrino astronomy". *Review of Scientific Instruments*, 81(8):081101, 2010.

[2] J. Beringer et al. "The Review of Particle Physics: Cosmic Rays". *Phys. Rev. D86, 010001*, 2012.

[3] J. Blümer et al. "Cosmic rays from the knee to the highest energies". *Progress in Particle and Nuclear Physics*, 63:293–338, 2009.

[4] K. Kotera and A. V. Olinto. "The Astrophysics of Ultrahigh-Energy Cosmic Rays". *Annual Review of Astronomy and Astrophysics*, 49:119–153, 2011.

[5] R. U. Abbasi et al. "First Observation of the Greisen-Zatsepin-Kuzmin Suppression". *Physical Review Letters*, 100(10):101101, 2008.

[6] J. Abraham et al. "Observation of the Suppression of the Flux of Cosmic Rays above 4×10^{19}eV". *Physical Review Letters*, 101(6):061101, 2008.

[7] T. Abu-Zayyad et al. "The Cosmic Ray Energy Spectrum Observed with the Surface Detector of the Telescope Array Experiment". *ArXiv e-prints*, 2012.

[8] M. Takeda et al. "Energy determination in the Akeno Giant Air Shower Array experiment". *Astroparticle Physics*, 19:447–462, 2003.

[9] K. Greisen. "End to the Cosmic-Ray Spectrum?". *Phys. Rev. Lett.*, 16:748–750, 1966.

[10] G. T. Zatsepin and V. A. Kuz'min. "Upper Limit of the Spectrum of Cosmic Rays". *Soviet Journal of Experimental and Theoretical Physics Letters*, 4:78, 1966.

[11] M. Lemoine. "Acceleration and propagation of ultrahigh energy cosmic rays". *ArXiv e-prints*, 2012.

[12] S. Hümmer et al. "Energy dependent neutrino flavor ratios from cosmic accelerators on the Hillas plot". *Astroparticle Physics*, 34:205–224, 2010.

[13] A. M. Hillas. "The Origin of Ultra-High-Energy Cosmic Rays". *Annual Review of Astronomy and Astrophysics, Vol. 22: 425-444*, 22:425–444, 1984.

[14] J. Abraham et al. "Correlation of the Highest-Energy Cosmic Rays with Nearby Extragalactic Objects". *Science*, 318:938–, 2007.

[15] P. Abreu et al. "Update on the correlation of the highest energy cosmic rays with nearby extragalactic matter". *Astroparticle Physics*, 34:314–326, 2010.

[16] R. Abbasi et al. "An absence of neutrinos associated with cosmic-ray acceleration in γ-ray bursts". *Nature 484, 351–354*, 484:351–354, 2012.

[17] E. Fermi. "On the Origin of the Cosmic Radiation". *Physical Review*, 75:1169–1174, 1949.

[18] M. Longair. *"High Energy Astrophysics"*. Cambridge University Press, 3rd edition, 2011.

[19] W. I. Axford et al. "The acceleration of cosmic rays by shock waves". In *International Cosmic Ray Conference*, volume 11 of *International Cosmic Ray Conference*, pages 132–137, 1977.

[20] G. F. Krymskii. "A regular mechanism for the acceleration of charged particles on the front of a shock wave". *Akademiia Nauk SSSR Doklady*, 234:1306–1308, 1977.

[21] R. D. Blandford and J. P. Ostriker. "Particle acceleration by astrophysical shocks". *ApJ Letters*, 221:L29–L32, 1978.

[22] W. Pauli. "Offener Brief an die Gruppe der Radioaktiven bei der Gauvereins-Tagung zu Tuebingen.", 1930.

[23] E. Fermi. "Versuch einer Theorie der β-Strahlen. I". *Zeitschrift fur Physik*, 88: 161–177, 1934.

[24] C. L. Cowan et al. "Detection of the Free Neutrino: a Confirmation". *Science*, Vol. 124(3212):103–104, 1956.

[25] S. Weinberg. "A Model of Leptons". *Physical Review Letters*, 19:1264–1266, 1967.

[26] S. Glashow. "Partial-symmetries of weak interactions". *Nuclear Physics*, 22:579–588, 1961.

[27] A. D. Martin et al. "Parton distributions for the LHC". *European Physical Journal C*, 63:189–285, 2009.

[28] R. Gandhi et al. "Neutrino interactions at ultrahigh energies". *Phys. Rev. D*, 58 (9):093009, 1998.

[29] A. Bhattacharya et al. "The Glashow resonance at IceCube: signatures, event rates and pp vs. pγ interactions". *jcap*, 10:017, 2011.

[30] M. H. Reno. "Neutrino cross sections at HERA and beyond". *Nuclear Physics B Proceedings Supplements*, 151:255–259, 2006.

[31] R. Gandhi et al. "Ultrahigh-energy neutrino interactions". *Astroparticle Physics*, 5:81–110, 1996.

[32] J. Pumplin et al. "New Generation of Parton Distributions with Uncertainties from Global QCD Analysis". *Journal of High Energy Physics*, 7:012, 2002.

[33] B. Voigt. *"Sensitivity of the IceCube Detector for Ultra-High Energy Electron-Neutrino Events"*. PhD thesis, Humboldt-Universitaet Berlin, 2008.

[34] D. Hooper. "Measuring high energy neutrino-nucleon cross sections with future neutrino telescopes". *Phys. Rev. D*, 65(9):097303, 2002.

[35] S. L. Glashow. "Resonant Scattering of Antineutrinos". *Physical Review*, 118: 316–317, 1960.

[36] The Tevatron Electroweak Working Group. Combination of CDF and D0 Results on the Width of the W boson. *ArXiv e-prints*, March 2010.

[37] J. Bahcall and E. Waxman. "High energy neutrinos from astrophysical sources: An upper bound". *Phys. Rev. D*, 59(2):023002, 1999.

[38] J. Bahcall and E. Waxman. "High energy astrophysical neutrinos: The upper bound is robust". *Phys. Rev. D*, 64(2):023002, 2001.

[39] R. Abbasi et al. "First search for atmospheric and extraterrestrial neutrino-induced cascades with the IceCube detector". *Phys. Rev. D*, 84(7):072001, 2011.

[40] A. Schukraft. "A view on prompt atmospheric neutrinos with IceCube". Nuclear Physics B Proceedings Supplement (00), 2012.

[41] A. Ishihara. "Ultra-high energy neutrinos with IceCube". *Nuclear Physics B Proceedings Supplements*, 2012.

[42] N. J. Carron. *"An Introduction to the Passage of Energetic Particles through Matter"*. Taylor and Francis, 2007.

[43] L. Rädel and C. Wiebusch. "Calculation of the Cherenkov light yield from low energetic secondary particles accompanying high-energy muons in ice and water with Geant 4 simulations". *ArXiv e-prints*, June 2012.

[44] J. Beringer et al. "The Review of Particle Physics: Passage of Particles through Matter". *Phys. Rev. D86, 010001*, 2012.

[45] H. J. Bhabha and W. Heitler. "The Passage of Fast Electrons and the Theory of Cosmic Showers". *Royal Society of London Proceedings Series A*, 159:432–458, 1937.

[46] J. Matthews. "A Heitler model of extensive air showers". *Astroparticle Physics*, 22: 387–397, 2005.

[47] A. Stoessl. "Estimating the Performance of Cascade Reconstruction algorithms with artificial light sources in IceCube". Diplomarbeit, Eberhard-Karls Universitaet Tuebingen, 2010.

[48] C. Wiebusch. *"The Detection of Faint Light in Deep Underwater Neutrino Telescopes"*. PhD thesis, RWTH Aachen, 1995.

[49] M. P. Kowalski. *"Search for Neutrino-Induced Cascades with the AMANDA-II Detector"*. PhD thesis, Humboldt-Universitaet zu Berlin, 2003.

[50] E. Middell. "Reconstruction of Cascade-Like Events in IceCube". Diplomarbeit, Humboldt-Universitaet Berlin, 2008.

[51] P. A. Čerenkov. "Visible Radiation Produced by Electrons Moving in a Medium with Velocities Exceeding that of Light". *Physical Review*, 52:378–379, 1937.

[52] J. D. Jackson. *"Classical Electrodynamics"*. John Wiley and Sons, 1962.

[53] G. N. Afanasiev. *"Vavilov-Cherenkov and Synchrotron Radiation: Foundations and Applications"*. Springer; 1 edition (November 3, 2004), 2004.

[54] R. Abbasi et al. "IceTop: The surface component of IceCube". *ArXiv e-prints*, 2012.

[55] J. van Santen. "Markov-Chain Monte-Carlo Reconstruction for cascade-like events in IceCube". Diplomarbeit, Humboldt-Universitaet Berlin, 2010.

[56] R. Abbasi et al. "The IceCube data acquisition system: Signal capture, digitization, and timestamping". *Nuclear Instruments and Methods in Physics Research A*, 601: 294–316, 2009.

[57] K. Hanson and O. Tarasova. "Design and production of the IceCube digital optical module". *Nuclear Instruments and Methods in Physics Research A*, 567:214–217, 2006.

[58] R. Abbasi et al. "Calibration and characterization of the IceCube photomultiplier tube". *Nuclear Instruments and Methods in Physics Research A*, 618:139–152, 2010.

[59] Hamamatsu Corp., editor. *"Photomultiplier Tubes - Basics and Applications"*. Hamamatsu Corp., 3rd edition, 2006.

[60] D. Chirkin. "Study of ice transparency with IceCube Flashers". *IceCube Internal Reports*, 2009.

[61] M. Inaba. "General performance of the IceCube detector and the calibration results". *International workshop on new photon-detectors PD07*, 2007.

[62] K. Filimonov et al. "Internal Calibration of IceCube Standard Candle I". *IceCube Internal Reports*, 2007.

[63] J. Kelley. "DOMs and DAQ Demystified, Part II: DAQ, Triggers, Filters and more (Talk at IceCube Bootcamp 2012)". unpublished, 2012.

[64] S. Yoshida and A. Ishihara. "Note on neutrino-generator and JULIeT: Effective area and event rate using the event weighting technique". *IceCube Internal Reports*, 2006.

[65] D. Chirkin and W. Rhode. "Propagating leptons through matter with Muon Monte Carlo (MMC)". *ArXiv High Energy Physics - Phenomenology e-prints*, 2004.

[66] D. Heck and J. Knapp. "CORSIKA an Air Shower Simulation Program". *Webpage*, 2010. URL http://www-ik.fzk.de/corsika/.

[67] M. Ackermann et al. "Optical properties of deep glacial ice at the South Pole". *Journal of Geophysical Research (Atmospheres)*, 111(10):D13203, 2006.

[68] D. Chirkin. "Study of South Pole ice transparency with IceCube Flashers". *32nd International Cosmic Ray Conference, Beijing, Proceedings*, 2011.

[69] D. Chirkin. "Photon Propagation Code". *Webpage*, 2010. URL http://icecube.wisc.edu/~dima/work/WISC/ppc/.

[70] R. C. Bay et al. "South Pole paleowind from automated synthesis of ice core records". *JOURNAL OF GEOPHYSICAL RESEARCH*, Vol. 115(D14126):10pp., 2010.

[71] J. Lundberg et al. "Light tracking through ice and water - Scattering and absorption in heterogeneous media with PHOTONICS". *Nuclear Instruments and Methods in Physics Research A*, 581:619–631, 2007.

[72] A. W. F. Edwards. *"Likelihood"*. Johns Hopkins, expanded paperback edition edition, 1992.

[73] M. J. D. Powell. "An efficient method for finding the minimum of a function of several variables without calculating derivatives". *The Computer Journal*, 7(2): 155–162, 1964.

[74] D. Pandel. "Bestimmung von Wasser- und Detektorparametern und Rekonstruktion von Myonen bis 100 TeV mit dem Baikal-Neutrinoteleskop NT-72", Humboldt-Universitaet Berlin, February 1996.

[75] J.C. Nash. "The (Dantzig) simplex method for linear programming". *Computing in Science Engineering*, 2(1):29 –31, 2000.

[76] J. van Santen. "Monopod: Millipede for Cascades". Talk at IceCube Fall Collaboration meeting (Uppsala, Sweden), September 2011.

[77] J. van Santen. "Private Communication with Monopod author Jakob van Santen". unpublished, 2012.

[78] S. Hickford. "Search for astrophysical neutrino-induced cascades using IceCube-40". *32nd International Cosmic Ray Conference, Beijing, Proceedings*, 2011.